Dispersion effects in buoyancy-driven flow in porous media: local vs. distributed drainage

by

Saeed Sheikhi Mohammadabadi

A thesis submitted in partial fulfillment of the requirements for the degree of

Doctor of Philosophy

Department of Mechanical Engineering

University of Alberta

Abstract

Understanding the dynamics of injecting fluids into porous media is essential for enhancing the reliability of subsurface storage/sequestration of fuels such as hydrogen or combustion byproducts such as carbon dioxide. In either case, significant progress has been made overcoming a variety of technical challenges, such as understanding capillary trapping in the context of carbon sequestration. Conversely, the dynamics of mixing, whether for miscible or immiscible systems, remain poorly understood. This work specifically focuses on the case of miscible systems and so is especially relevant when considering the flow of hydrogen into cushion gas, i.e. the gas that remains in formation in a depleted natural gas reservoir. The overarching goal of this thesis is to clarify the dispersive mixing dynamics of a source fluid injected into a saturated porous medium characterized by cap rock that is leaky and possibly inclined. Our study employs both theoretical analysis and numerical simulations and assumes small density differences between the source and ambient fluids, consistent with the Boussinesq approximation.

To address the above objective, three interrelated problems are considered. First, we consider the mixing dynamics of a gravity current fluid that propagates along cap rock layer characterized by an isolated fissure. The gravity current thereby experiences dispersion and local drainage. We present a reduced-order theoretical model that includes coupled, non-linear partial differential equations, the solution of which yields estimates for the gravity current shape and density. We validate this theoretical model using COMSOL numerical simulations that mimic laboratory experiments. Our findings demonstrate that the fissure permeability and dimension impact the degree of dispersive mixing, as do the dip angle and flow conditions upstream of the fissure.

The second research component replaces the localized drainage of the above paragraph with distributed drainage, which is experienced along the length of a (thin) interbed layer. Our theoretical model and accompanying COMSOL simulations suggest that the relative intensity of dispersion is influenced by the amount of mixing experienced by the fluid that drains through the interbed layer. To this end, we consider two extreme scenarios for the mixing of this drained fluid: no mixing and perfect mixing. Comparing the theoretical model predictions with COMSOL output, it is observed that the no mixing model performs better at early times, while the perfect mixing model is more reliable at late times. In this context, the degree of dispersive mixing experienced by the gravity current depends on the effective permeability of the interbed layer and the dip angle.

The third research component is to validate our reduced-order theoretical model for underground hydrogen storage in depleted gas reservoirs. Thus do we compare predictions from the theoretical model described in the previous paragraph against the output of reservoir-level simulation software such as CMG and OpenGoSim. Relative to the reduced-order models, these reservoir simulator packages take into account more complex factors e.g. thermodynamic effects including non-linear equations of state and concentration-dependent viscosities. By performing this comparison study, we find that the theoretical model is often successful in predicting both the amount of hydrogen that dispersively mixes with the surrounding ambient gas and the shape of the gravity current.

The overarching contribution of this thesis is to present a straightforward hydrodynamic model that describes the evolution and dispersive mixing of miscible, leaky porous media flows reasonably well, all the while neglecting the kinds of thermodynamical details that would otherwise render the model very computationally expensive to solve.

Preface

This thesis is an original work by Saeed Sheikhi. The mathematical formulations of Chapters 2 and 3 and numerical simulations in Chapters 2, 3 and 4 are conducted by myself, with the assistance of Dr. M. R. Flynn.

Chapter 2 of this thesis has been published as S. Sheikhi, C. K. Sahu and M. R. Flynn, "Dispersion effects in porous medium gravity currents experiencing local drainage", Journal of Fluid Mechanics, vol. 975, 2023, A18. Chapter 3 of this thesis has been published as S. Sheikhi and M. R. Flynn, "Porous media gravity current flow over an interbed layer: the impact of dispersion and distributed drainage", Journal of Fluid Mechanics, vol. 984, 2024, A33. Chapter 4 of this thesis also has been published as S. Sheikhi and M. R. Flynn, "Can a hydrodynamic model predict the flow evolution of a hydrogen plume in a depleted natural gas reservoir?", International Journal of Hydrogen Energy, vol. 81, 2024, 795-804. I was responsible for theoretical developments, numerical simulations and analysis as well as the manuscript writing. Dr. M. R. Flynn was the supervisory author and was involved with concept formations and manuscript revisions.

Acknowledgements

My sincere gratitude is extended to my family, friends, and mentors, who have all contributed to this project. With particular gratitude to:

- my supervisor, Dr. Morris Flynn, for his invaluable assistance, support and guidance without which this work would not have been possible. Throughout this study, he provided helpful advice, encouragement, and cooperation that improved the results and directed the research in a fruitful direction. His broad knowledge and experience have been essential to this project's success.
- my supervisory committee members, Dr. Carlos Lange and Dr. Arman Hemmati for their thoughtful comments that have helped me improve my research and outline a suitable timeline for my PhD program during our committee meetings.
- my spouse for her constant understanding and support during this journey. Her tolerance and support have always been a source of courage and inspiration for me.
- my dad, mom, and brother for their endless support.
- the members of Morris research group, my friends and fellow at the University of Alberta who have accompanied me on this important journey.

Contents

Abstract ii

Preface iv

Acknowledgements v

List of Tables x

List of Figures xi

List of Symbols xviii

1 Introduction and overview 1

1.1 Geological carbon dioxide sequestration 1

1.2 Hydrogen as a substitute for fossil fuel 4

1.2.1 Surface hydrogen storage 4

1.2.2 Underground hydrogen storage 5

1.3 Buoyancy-driven flow in porous media 8

1.3.1 Literature review 10

1.4 Knowledge gap 16

1.5 Thesis outline 18

2 Dispersion effects in porous media gravity currents experiencing local drainage 21

2.1 Abstract 21

2.2 Introduction . . . 22
2.3 Theoretical model . . . 26
2.3.1 Governing equations . . . 26
2.3.2 Boundary conditions . . . 32
2.3.3 Non-dimensional governing equations . . . 33
2.4 Numerical investigation . . . 36
2.4.1 Numerical set-up . . . 37
2.4.2 Initial conditions . . . 41
2.4.3 Meshing and solver . . . 41
2.4.4 Qualitative observations (horizontal bottom boundary) . . . 42
2.4.5 Determining the entertainment coefficient . . . 43
2.5 Results and discussion . . . 45
2.6 Application to UHS . . . 51
2.7 Summary and conclusions . . . 54

3 Porous media gravity current flow over an interbed layer: the impact of dispersion and distributed drainage 56

3.1 Abstract . . . 56
3.2 Introduction . . . 57
3.3 Theoretical model . . . 62
3.3.1 Governing equations . . . 62
3.3.2 Boundary conditions . . . 68
3.3.3 Non-dimensional governing equations . . . 69
3.4 Numerical simulations . . . 72
3.4.1 COMSOL set-up . . . 73
3.4.2 Initial conditions and solver . . . 74
3.4.3 Preliminary validation . . . 75
3.4.4 Determination of the entertainment coefficient . . . 76
3.5 Results and discussion . . . 78

3.5.1 Comparison of theoretical and numerical results . . . 78
3.5.2 Effects of K_{eff} and θ on dispersion . . . 82
3.5.3 Flow characterization past the point of theoretical model breakdown . . . 85
3.6 Summary and conclusions . . . 88

4 Can a hydrodynamic model predict the flow evolution of a hydrogen plume in a depleted natural gas reservoir? 92
4.1 Abstract . . . 92
4.2 Introduction . . . 93
4.3 Numerical simulations . . . 97
4.3.1 Formulation . . . 97
4.3.2 OpenGoSim . . . 101
4.3.3 CMG . . . 101
4.4 Theoretical model development . . . 102
4.5 Results . . . 107
4.5.1 Comparison of the theoretical and numerical results . . . 107
4.5.2 Results beyond the theoretical model . . . 113
4.6 Conclusions . . . 115

5 Conclusions and future work 117
5.1 Primary contributions from the present work . . . 120
5.2 Limitations of the present study to be addressed by future work . . . 122

References 125

Appendix A Theory details of gravity currents experiencing local drainage 134
A.1 Derivation of the bulk and dispersed velocity in the theoretical model . . . 134
A.2 Derivation of the drainage velocity in the theoretical model . . . 135
A.3 Method of solution for the theoretical model . . . 136

Appendix B Theory details of gravity currents over an interbed layer 139

B.1 Derivation of the drainage velocity in the perfect mixing model 139
B.2 Derivation of the drainage velocity in the no mixing model 140

Appendix C Details of numerical simulations **143**

C.1 Verification and validation of numerical simulations 143
C.1.1 COMSOL 143
C.1.2 CMG and OpenGoSim 145
C.2 Workflow of numerical simulations 146

List of Tables

1.1 Scientific contributions of this thesis. 20

1.2 List of scientific meetings at which the author has presented portions of this thesis. Abbreviations are as follows: APS - DFD: American Physical Society - Division of Fluid Dynamics, IGR: Institute of Geophysical Research, FEGRS: The Faculty of Engineering Graduate Research Symposium. Furthermore, Interpore is an annual conference organized by the International Society of Porous Media. 20

3.1 Lower layer dispersed buoyancy fraction at $t = 150$ for various K_{eff} and $\theta = 0°$ and $\theta = 5°$. 87

List of Figures

1.1 [Colour] Options for geological CO_2 storage. Adapted from Ali *et al.* (2022) under the terms of the Creative Commons CC-BY license. 2

1.2 [Colour] Schematic of the hydrodynamic effects and gas mixing in an underground hydrogen storage facility. Adapted from Michelsen *et al.* (2023) and used with permission. 6

1.3 [Colour] (a) Dense plume and (b) dense gravity current with density ρ within a uniform porous medium. This figure is generated by running COMSOL simulations of the type described in Chapter 2 and Chapter 3. 9

1.4 Physical mechanisms cause dispersion in porous media. 10

1.5 Gravity current over a narrow permeable layer. 14

2.1 [Colour] Schematic of a leaky gravity current propagating along an inclined boundary with local drainage through an isolated fissure. The gravity current consists of bulk and dispersed phases. Variables h_1 (bulk phase height), h_2 (overall height), u_1 (bulk phase velocity), u_2 (dispersed phase velocity), w_{e1} (entrainment velocity from bulk phase), w_{e2} (entrainment velocity from ambient), and $\bar{c}_2$ (average concentration in dispersed phase) are function of x and t. Meanwhile, variables x_{N_b} (bulk phase nose position) and x_{N_d} (dispersed phase nose position) are function of t only. 28

2.2 Theoretical predictions showing, for different times, gravity current profiles for (a) $\theta = 0°$ and (b) $\theta = 5°$. The thick line represents the bulk interface and the thin line represents the dispersed interface. The location of the fissure is as indicated. Here, $\Gamma = 35$, $K = 0.5$, $l^* = 0.79$ and $\xi^* = 0.04$. As we will justify in section 2.4.5, we consider $\varepsilon = 0.0125$ when $\theta = 0°$ and $\varepsilon = 0.0086$ when $\theta = 5°$. 37

2.3 Percentage of the gravity current (a) volume and (b) buoyancy that remains in the dispersed phase for $\theta = 0°$ with $\varepsilon = 0.0125$ and $\theta = 5°$ with $\varepsilon = 0.0086$. Here, consistent with figure 2.2, $\Gamma = 35$, $K = 0.5$, $l^* = 0.79$ and $\xi^* = 0.04$. 38

2.4 Schematic of the numerical set-up. 39

2.5 Numerically-determined estimates for the dispersed phase area fraction for different grid sizes. Here, consistent with figure 2.2, $\theta = 0°$, $\Gamma = 35$, $K = 0.5$, $l^* = 0.79$ and $\xi^* = 0.04$. 42

2.6 [Colour] Bulk phase concentration reduction beyond the fissure for $\theta = 0°$ and $l^* = 0.79$. The red area shows $c^* > 0.9$, the green area shows $0.8 < c^* < 0.9$ and the blue area shows $c^* < 0.8$. Boundaries are drawn based on an interpolation performed over a total of 14 simulations for each of the lower and upper surfaces. The inset images show a comparison between theory and numerical simulations for different combinations of Γ and K. The thick (thin) white line is the bulk (dispersed) interface as predicted by the theoretical model of section 2. Meanwhile colored contours show the output of the COMSOL numerical model. Red dashed lines indicate the location $x^* = 2$, where concentrations are evaluated in constructing the regime diagram. . . . 44

2.7 [Colour] Error-minimizing value of ε vs. θ. Here we consider $\Gamma = 45$, $K = 0.3$, $l^* = 0.79$ and $\xi^* = 0.04$. Blue circles consider $\Gamma = 45$, $K = 0.2$ and red crosses consider $\Gamma = 30$, $K = 0.3$ Also, and with reference to (2.47), $t_1^* = 20$ and $t_2^* = 70$. . . 45

2.8 [Colour] Gravity current profiles as predicted theoretically and numerically. Line types are as follows: thick solid line – bulk interface; thin solid line – dispersed interface; dashed line – sharp interface solution obtained by setting $\varepsilon = 0$ in (2.16) and (2.17). Numerical output is indicated by the colour contours. (a-d) $\theta = 0°$, $\Gamma = 35$, $K = 0.5$, $\xi^* = 0.04$, and $l^* = 0.79$. (e-h) $\theta = 5°$, $\Gamma = 70$, $K = 0.3$, $\xi^* = 0.04$, and $l^* = 1.11$. The variation of parameter values between the left- and right-hand side panels is deliberate and illustrates model predictions over a broad range of the parameter space. Note that the scale of the horizontal axis in the left- and right-hand side images is different. 46

2.9 (a) Area fraction (equation 2.36) and (b) buoyancy fraction (equation 2.38) as a function of the upstream flow parameter (equation 2.26 a) for three different values of the fissure parameter (equation 2.26 b). Here, we consider a horizontal bottom boundary such that $\theta = 0°$ and $t^* = 40$. Crosses indicate the solutions for $\Gamma = 45$, for which corresponding time series data are given in panels (c), (d) and (e) for $K = 0.2$, 0.3 and 0.4, respectively. These same three K values are considered in the time series of panels (f), (g) and (h), which consider, again for $\Gamma = 45$ and $\theta = 0°$, the difference of nose position between the bulk and the dispersed gravity currents. This nose position difference is shown as a function of Γ in panel (i) where we again consider $t^* = 40$. 48

2.10 As in figure 2.9 but with an inclined boundary ($\theta = 5°$). 50

2.11 Difference of (a) nose positions and of (b) dispersed phase area and buoyancy fractions vs. θ. Here, $t^* = 45$, $\Gamma = 35$, $K = 0.5$, $l^* = 0.79$ and $\xi^* = 0.04$. 51

2.12 Difference of (a) nose position and (b) area fraction in the dispersed phase for $\theta = 0°$ with $\varepsilon = 0.0125$ and $\theta = 5°$ with $\varepsilon = 0.0086$ for various ξ^*. Here, $t^* = 45$, $\Gamma = 35$, $K = 0.5$, and $l^* = 0.79$. 51

2.13 As in figure 2.12 but considering the influence of l^* for $\xi^* = 0.04$. 52

2.14 Fraction of H_2 lost to dispersion vs. source volume flow rate for the example of section 2.6. The horizontal dashed line assumes a maximum loss fraction of 5%. 53

3.1 [colour] Schematic of a leaky gravity current propagating along, and draining through, the permeability jump associated with an interbed layer of thickness ξ. We assume equal permeability k in the upper and lower layers, and a reduced permeability k_b in the interbed layer. The gravity current and the fluid that drains from the gravity current consist of bulk and dispersed phases. These are respectively confined by the red and black curves. Meanwhile, the dashed curve that is drawn through the lower two layers signifies the equivalent depth of draining fluid, assuming that this draining fluid consists solely of bulk fluid, i.e. has a density that matches the source density. The variables h_1, h_2, u_1, u_2, w_{e1}, w_{e2} and $\bar{c}_2$ depend on x and $\tilde{t}$. Conversely the variables x_{N_b} and x_{N_d} depend only on $\tilde{t}$. The vertical scale is exaggerated in this schematic. 63

3.2 [colour] Schematic of a leaky gravity current experiencing perfect mixing in (and therefore immediate removal from) the lower layer. The red line indicates the bulk interface and the black line indicates the dispersed interface. 66

3.3 Theoretical predictions showing gravity current profiles assuming (a) perfect mixing, and, (b) no mixing in the lower layer. Thick lines represent the bulk interface and thin lines represent the dispersed interface. Here, $K = 0.0025$, $\xi = 0.333$ (equivalent to $K_{\text{eff}} \equiv K(1 + \frac{1}{\xi}) = 0.01$, see equation 3.40 below) and $\theta = 0°$. We further assume that $\varepsilon = 0.0344$. The justification for this choice will be presented in subsection 3.4.4. 71

3.4 Schematic of the numerical set-up that similitude (a) perfect mixing (b) laboratory experiments. 73

3.5 Error-minimizing value of ε versus θ and $K_{\text{eff}} = K\left(1 + \frac{1}{\xi}\right)$. 78

3.6 [colour] Numerical prediction of the gravity current profile versus the analogue theoretical predictions corresponding to perfect mixing (red curves) and no mixing (black curves). Thick lines indicate the bulk interface and thin lines indicate the dispersed interface. The color contours show the numerical output. (a-d) $\theta = 0°$ and (e-h) $\theta = 5°$. Here, $K = 0.0025$ and $\xi = 0.333$ which is equivalent to $K_{\text{eff}} = 0.01$. 79

3.7 [colour] Time series of the bulk and dispersed nose positions for $\theta = 0°$ and (a) $K_{\text{eff}} = 0.01$ and (b) $K_{\text{eff}} = 0.02$. Numerical data are indicated by the square symbols; theoretical predictions are indicated by the red (perfect mixing) and black (no mixing) curves. The dashed black curves indicate the domain where the hydrostatic assumption becomes invalid in the no mixing model. The inset images show the bulk and dispersed interfaces before and after the sharp reduction in the position x_{N_d} of the dispersed nose for the no mixing case. 80

3.8 [colour] Theoretical model regime diagram illustrating the regimes where (i) both of the no mixing and perfect mixing models return accurate predictions [red], (ii) the no mixing model remains hydrostatic but is inaccurate owing to its over-prediction of gravity current retraction [green], (iii) the no mixing model is invalid [blue], and, (iv) both models become invalid [white]. Formally, data are shown for $\theta = 0°$; however, we find very similar results at different inclination angles. 82

3.9 [colour] (a) Difference of nose separation and (b) buoyancy fraction in the dispersed phase for $\theta = 0°$ but various K_{eff} at $t = 150$. 84

3.10 [colour] As in figure 3.9 but considering the influence of θ for $K_{\text{eff}} = 0.01$. 84

3.11 [colour] Numerical prediction of the flow in the green and blue regions of figure 3.8. Inset images show the gravity current profile in more detail. Here, $K_{\text{eff}} = 0.03$, $\theta = 0°$ and non-dimensional times are as indicated. 86

3.12 [colour] Numerical prediction of the gravity current and associated draining flow for different K_{eff} at $t = 150$ and with $\theta = 0°$. The inset images show the vertical variation of the vertical velocity, w. Curves are drawn for $t = 100$ (black lines) and $t = 150$ (red lines). The red dashed line from the left-most image displays the location $x = 3$ where vertical velocities are evaluated. 87

4.1 Schematic of the numerical domains. (a) Planar geometry, (b) curved (i.e. one-half of an anticline-like) geometry. Note that the scale of the domain is not identical in all directions. The dark stripe indicates the interbed layer. The interbed thickness varies between 1 m and 1.5 m in different simulations. The domain height H and lower layer height H_l are, respectively, 150 m and 38 m for unconfined domains and 50 m and 23 m for confined domains. 97

4.2 [Colour] Relative permeability of the aqueous and gas phase based on saturation. Note that for irreducible water (i.e. $S_g \leq 0.2$), the relative permeability of the gas phase remains unchanged. This is because the irreducible water resides small pore spaces that do not contribute to the overall flow (Ahmed, 2010). 98

4.3 [colour] Schematic of a leaky gravity current elongating over an inclined interbed layer. The upper and lower layers have identical permeability, k, and the interbed layer has a smaller permeability, k_b. The red and black lines respectively define the boundaries of the bulk and dispersed phases of the gravity current. We assume a "perfect mixing model" whereby source fluid that drains into the upper layer is quickly and thoroughly mixed into the surrounding ambient. Adapted from figure 2 of Sheikhi & Flynn (2024). 103

4.4 [colour] Theoretical predictions for the profile of the bulk phase gravity current (thick solid curves) and the dispersed phase gravity current (thin solid curves) vs. the analogue numerical simulation output (color contours) computed using (a) OpenGoSim, and, (b) CMG. Here we consider a dip angle of $\theta = 0°$, a total time of 6 months and two different values for K_{eff}, defined by (4.22). 108

4.5 Time series data of the buoyancy fraction in the dispersed phase for $\theta = 0°$ and different K_{eff}. (a) OpenGoSim results, and, (b) CMG results. Lines connecting adjacent data points are included to highlight the overall trend of the numerical data. Shaded domains indicate times when the gravity current bulk phase either stops elongating or experiences retraction. The time $t = 0$ corresponds to the initiation of hydrogen flow. 108

4.6 Time variation of the bulk nose positions predicted by CMG for various K_{eff} and $\theta = 0°$. Theoretical predictions for each K_{eff} value are indicated with the solid lines. 109

4.7 [colour] Dispersed phase buoyancy fraction vs. K_{eff} for formation pressures of $P_{\text{form}} =$ 100 bar, 125 bar and 150 bar. Results are shown assuming $\theta = 0°$, $t = 180$ days for black circles, $t = 92$ days for red circles and $t = 53$ days for blue circles. In all cases, $t^* = 90$, where (4.13) is used in defining the non-dimensional time. For each pressure, the marker size indicates the volume of fluid in the bulk phase. For ease of presentation, data are normalized so that the symbols corresponding to $K_{\text{eff}} = 0.06$ are all the same size. 110

4.8 Variation of the bulk phase non-dimensional nose position as a function of non-dimensional time t^*, compared for different formation pressures, namely 100 bar (circles), 125 bar (squares) and 150 bar (stars). (a) $K_{\text{eff}} = 0.015$, and, (b) $K_{\text{eff}} = 0.06$. In both panels, we assume a horizontal interbed layer such that $\theta = 0°$. 111

4.9 [colour] As in figure 4.4 but with an inclination angle $\theta = 10°$. (a) $K_{\text{eff}} = 0.015$ (b) $K_{\text{eff}} = 0.06$. Note that only CMG-based numerical results are shown. 112

4.10 [colour] Gravity current evolution in a vertically-confined porous medium where $\theta = 0°$. As in figures 4.4 and 4.9, the thick and thin red curves indicate the theoretically-predicted boundaries for the bulk and dispersed gravity currents. Color contours show the output of the CMG numerical simulations. (a) $K_{\text{eff}} = 0.015$, and, (b) $K_{\text{eff}} = 0.06$. Results are shown after 6 months of hydrogen injection. 112

4.11 Time series data of the dispersed phase buoyancy fraction for a horizontal (circles), 10° inclined (squares) and anticline (stars) domain. (a) $K_{\text{eff}} = 0.015$, and, (b) $K_{\text{eff}} = 0.06$. Note that the y-axis limits are different for panels (a) and (b). Note that the closed and open circles are drawn directly from figure 4.5 (b). Note also that the average inclination angle experienced by a gravity current in an anticline domain progressively increases as time evolves and the gravity current elongates. The average inclination angle is specified here at $t = 90$ days, 120 days, 150 days and 180 days. 114

C.1 COMSOL estimates for the dispersed phase bouncy fraction for different grid sizes in the distributed drainage case. Here, $K_{\text{eff}} = 0.015$, $\theta = 0°$ and $t^* = 150$. 144

C.2 [Colour] Comparison between COMSOL and the Huppert & Woods (1995) solution for a porous media gravity current propagating along an impermeable boundary without drainage. Here, $k = 2.18 \times 10^{-4}\,\text{cm}^2$, $q_s = 0.14\,\text{cm}^2/\text{s}$ and (a) $g'_s = 15\,\text{cm/s}^2$,(b) $g'_s = 30\,\text{cm/s}^2$. 144

C.3 [Colour] Comparison between COMSOL and Bear's (1972) theoretical solution for a concentration front progressing through a porous medium. Here, $k = 2.18 \times 10^{-4}\,\text{cm}^2$, $\phi = 0.38$, $t = 200$ sec and (a) $q = 0.001\,\text{cm/s}$, (b) $q = 0.01\,\text{cm/s}$. The horizontal axis variable, $x' = \frac{x - \frac{qt}{\phi}}{\sqrt{\frac{4Dt}{\phi}}}$, represents a Galilean-shifted horizontal coordinate in which D is the dispersion coefficient. The vertical axis variable, c/c_s, represents the non-dimensional scalar concentration in which c_s is the concentration ahead of the advancing front. 145

C.4 Dispersed phase buoyancy fraction vs. (a) the medium permeability, k, and (b) the source volume flow rate, Q_{in}. Results are shown assuming a formation pressure of $P_{\text{form}} = 100\,\text{bar}$. We further assume that $\theta = 0°$, $t = 180\,\text{day}$ and $K_{\text{eff}} = 0.015$. Note that $Q_{\text{in}} = 2 \times 10^5\,\text{S m}^3/\text{day}$ in panel (a) and $k = 100\,\text{mD}$ in panel (b). 146

C.5 CMG estimates for the dispersed phase buoyancy fraction for different grid sizes. Here, consistent with figure C.4, $P_{\text{form}} = 100\,\text{bar}$, $Q_{\text{in}} = 2 \times 10^5\,\text{S m}^3/\text{day}$, $k = 100\,\text{mD}$, $\theta = 0°$, $t = 180\,\text{day}$ and $K_{\text{eff}} = 0.015$. 147

C.6 [Colour] Numerical software workflow visualization. 147

List of Symbols

Greek symbols

α	Dispersive entrainment coefficient
β	Solute contraction coefficient
η_β	Molar density of phase β
Γ	Upstream flow parameter
κ	Rock thermal conductivity
μ	Dynamic viscosity
μ_β	Viscosity of phase β
ν	Kinematic viscosity
ϕ	Porosity
ρ_β	Density of phase β
ρ_r	Rock density
θ	Inclination angle
ε	Entrainment coefficient
ξ	Fissure width (Chapter 2) or interbed layer thickness (Chapter 3 and 4)

Other symbols

$\tilde{A}_{\text{disp}}$	Fraction of area enclosed by the dispersed interface
A_{bulk}	Area enclosed by the bulk interface
A_{disp}	Area enclosed by the dispersed interface
a_L	Longitudinal dispersivity
a_T	Transverse dispersivity

b	Buoyancy
$\tilde{B}_{\text{disp}}$	Fraction of buoyancy enclosed by the dispersed interface
B_{bulk}	Buoyancy enclosed by the bulk interface
B_{disp}	Buoyancy enclosed by the dispersed interface
c	Concentration
c_r	Rock specific heat capacity
D	Dispersion coefficient
D_g^*	Gas phase effective molecular diffusion
D_g^{mol}	Gas phase standard molecular diffusion
D_{mol}	Molecular diffusion
D_g	Gas phase dispersion
d_p	Beads diameter
$\overline{E}$	Mean temporal error
F_g	Gas phase formation resistivity factor
g	Gravitational field
g'	Reduced gravity
h	Gravity current height
H_β	Hydrostatic pressure head of phase β
K	Permeability ratio of fissure (Chapter 2) or permeability ratio of interbed layer (Chapter 3 and 4)
k	Medium permeability
k_β	Relative permeability of phase β
k_b	Interbed layer permeability
k_f	Fissure permeability
K_{eff}	Effective permeability of interbed layer
l	Fissure depth (Chapter 2) or depth of drained fluid (Chapter **??** and 3)
P	Pressure
Pe	Péclet number

$q\,(Q)$ Volume flow rate

Ra Rayleigh number

Re Reynolds numbe

S_β Saturation of phase β

T Temperature

u Horizontal velocity

U_β Internal energy of phase β

u_β Velocity of phase β

V Darcy flux

w_d Drainage velocity

w_e Entrainment velocity

x_β^α Mole fraction of component α in phase β

x_f Fissure position

x_{N_b} Bulk phase nose position

x_{N_d} Dispersed phase nose position

Subscripts

0 Reference value

1 Bulk phase

2 Dispersed phase

s Source value

Superscripts

$*$ Non-dimensional value

Chapter 1

Introduction and overview

Modern global energy systems, which largely rely on hydrocarbon-based fuels, have undeniably played a significant role in contributing to climate change and environmental issues (United Nations, 2021,). Global CO_2 emissions are estimated to be 23-84 Gt annually by 2050, leading to an increase in Earth's surface temperature by 1.61°C (Metz *et al.*, 2005). The mitigation actions taken to reduce the discharge of anthropogenic CO_2 to the atmosphere e.g.

- Capture and store CO_2 in geological formations,
- Switch to clean energy sources such as hydrogen instead of fossil fuels,

have been implemented. There is a vast area of active fundamental research and commercial development, the details of which are highlighted below.

1.1 Geological carbon dioxide sequestration

Carbon dioxide (CO_2) can be captured from production sources (either stationary e.g. power plants or moving e.g. vehicles by bringing the exhaust gases into contact with a solvent to capture the CO_2), compressed to a supercritical state, and subsequently injected into deep oil and gas reservoirs, unmineable coal seams or saline formations (Keith *et al.*, 2004), see figure 1.1. An IEA report (2002)

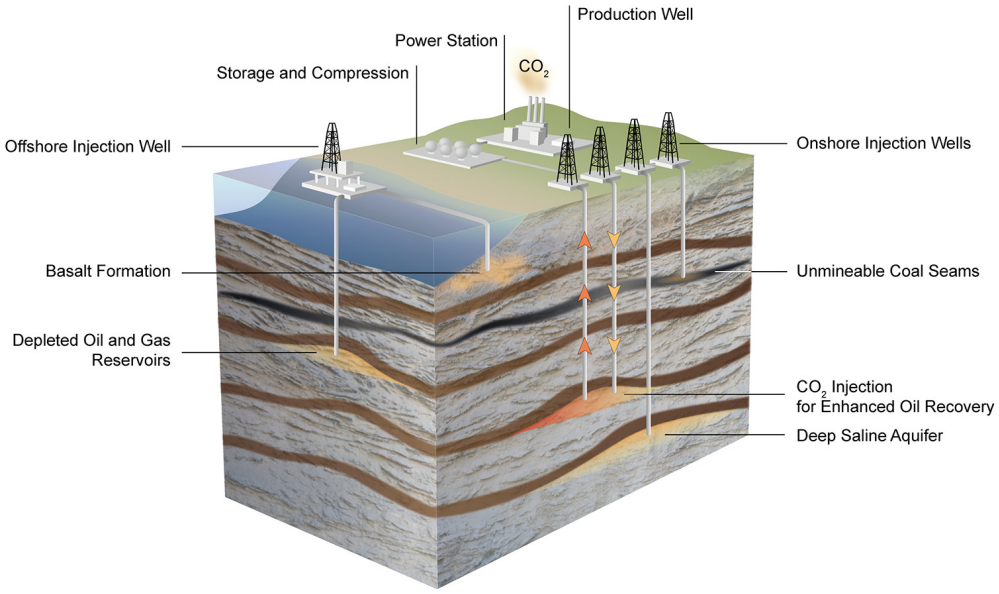

Figure 1.1: [Colour] Options for geological CO_2 storage. Adapted from Ali *et al.* (2022) under the terms of the Creative Commons CC-BY license.

highlights that saline aquifers have the capacity to store approximately ten trillion tons of CO_2 around the world. As a result, saline aquifers have been pursued with the greatest investment for carbon sequestration among geological storage strategies. After injection, the injected CO_2 is more buoyant than the surrounding brine, yielding a rising CO_2 plume (Bolster, 2014). Once the ascending plume encounters an impermeable boundary, it spreads laterally as a gravity current (Riaz *et al.*, 2006). The vertical and horizontal flow of CO_2 can cause its superficial leakage through local fractures or semi-permeable layers; however, various geophysical and chemical mechanisms, e.g. residual trapping, dissolution trapping and mineral trapping, might hinder such leakage (Luo *et al.*, 2022; Massarweh & Abushaikha, 2024).

- **Residual trapping**: When CO_2 moves in porous rock, it can become trapped within pore spaces due to physical and chemical interactions with the rock matrix (Zuo & Benson 2014; Rahman *et al.* 2016; Rasmusson *et al.* 2018; Amooie *et al.* 2024). In other words, as CO_2 encounters surfaces with varying wettabilities, capillary forces can trap it in smaller pore spaces due to the surface tension of the CO_2-fluid-rock interface (Huppert & Neufeld, 2014). Ide *et al.* (2007) showed that this trapping mechanism becomes stronger when the aquifer is

inclined because gravity can further contribute (by making a thinner and longer flow, thereby allowing it to contact a larger volume of the aquifer) to trapping and immobilize CO_2 in lower regions before it leaks to the upper regions of the aquifer. The amount of trapped CO_2 in this mechanism is also influenced by the relative permeability characteristics and heterogeneity of the aquifer rocks.

- **Dissolution trapping**: CO_2 can dissolve into brine within the pore spaces of the rock formation. Once dissolved, the CO_2 can be transported with the formation fluids over long distances. The brine saturated with dissolved CO_2 has a density greater than that of uncontaminated brine (Riaz *et al.*, 2006). Consequently, the contaminated brine moves downwards and might initiate finger-like instabilities. The instabilities occur when the boundary layer Rayleigh number in porous media, $Ra = (g\Delta\rho_c k\delta)/(\mu_w \phi D)$, is more than a critical Rayleigh number, Ra_c, (Huppert & Neufeld, 2014). Here, $\Delta\rho_c$ is the density difference between the pure brine and contaminated brine, k is the permeability, δ is the boundary layer thickness, μ_w is the brine viscosity, ϕ is the porosity and D is the diffusivity of CO_2 in water. Such instabilities effectively trap high amounts of CO_2 within the subsurface (Neufeld *et al.* 2010; MacMinn *et al.* 2012; Khan *et al.* 2022; Lyu & Voskov 2023).

- **Mineral trapping**: CO_2 might react chemically with minerals in the rock formation, leading to the formation of carbonate minerals, such as calcite or dolomite. This process, known as mineral trapping or mineral carbonation, can immobilize sequestered CO_2 over geological timescales by converting it into a solid form within the rock matrix (Gunter *et al.*, 1993; Bello *et al.*, 2024).

The relative importance of each trapping mechanism might change over time during CO_2 storage.

In addition to CO_2 sequestration in geological formations, there are other methods available. For example, CO_2 can be incorporated into concrete, trapping it within construction materials (Zhang *et al.*, 2024). Another option is to inject liquid CO_2 into the depths of the oceans, where high-pressure and cold conditions facilitate sequestration (Pryck & Boettcher, 2024). CO_2 can also react with naturally occurring minerals to form stable carbonates, which can then be used in

construction materials or safely stored (Kurusta *et al.*, 2023). We can utilize CO_2 as a feed-stock to produce chemicals and fuels, e.g. methanol and synthetic hydrocarbons (Mustafa *et al.*, 2020). By converting CO_2 into these valuable products, we help reduce its presence in the atmosphere.

1.2 Hydrogen as a substitute for fossil fuel

Hydrogen, one of the potential alternatives to hydrocarbon fuels, can be transformed into heat or electricity without producing CO_2 (Andrews & Shabani, 2012). However, the degree to which CO_2 emissions are eliminated by using hydrogen depends on the method of hydrogen production. For instance, green hydrogen (produced by using renewable energy sources to electrolyze water) yields no greenhouse gas emissions during production while grey and blue hydrogen (generated from natural gas using a chemical reaction called steam reforming) or brown and black hydrogen (generated from the gasification of coal) release greenhouse gases, principally CO_2, to the atmosphere (World Energy Council, 2019). In case of blue hydrogen, CO_2 is captured and stored rather than released to the atmosphere. Results show that coal-based hydrogen production without CO_2 sequestration releases 21 kg of CO_2 for each kg of hydrogen produced (Li *et al.*, 2022). One of the significant challenges in the widespread adoption of green hydrogen production is the intermittency of renewable energy sources like wind and solar. These sources are dependent on weather conditions and are not always available on demand. Therefore, storing excess hydrogen is crucial for ensuring reliable supply during times of high demand. Note that the imbalance in question may be measured hourly or seasonally depending on context and the size of production and storage facilities (Sainz-Garcia *et al.*, 2017). Hydrogen might be stored either at the surface in limited volumes or stored underground in large volumes.

1.2.1 Surface hydrogen storage

Hydrogen can be stored as a gas or liquid at the surface; in either case, safety concerns apply due to explosion hazards. As a gas, hydrogen is stored in high-pressure tanks at pressures up to 700 bar. This method is suitable for stationary applications and some vehicle applications but requires

strong and durable tanks to withstand such high pressures. As a liquid, hydrogen is is stored in cryogenic temperatures (-253°C) to stay in the liquid phase, reducing its volume significantly for storage. This method is commonly used in aerospace applications but requires energy-intensive liquefaction processes and specialized storage infrastructure. Therefore, high pressure tanks and cryogenic temperatures are required for gas and liquid storage, respectively, where, in either case, substantial costs may be incurred.

1.2.2 Underground hydrogen storage

A more appealing option, particularly when considering large volumes of hydrogen, may be underground hydrogen storage (UHS). Storage within geological strata leverages aquifers or depleted oil and gas reservoirs. Alternatively, solution mining may be used to generate voids within salt deposits such that hydrogen is stored within the so-produced salt cavern (Taylor *et al.*, 1986).

Salt caverns

Salt caverns can withstand high pressures, making them ideal for storing hydrogen in a compact form. However, there are several challenges associated with hydrogen storage in salt caverns, such as geographical limitations, high infrastructure costs, and environmental concerns. For example, suitable salt formations are not found everywhere, limiting potential storage locations. Additionally, the solution mining process used to create these caverns can have environmental impacts, including groundwater contamination if not properly managed. Despite the fact that gas can be withdrawn from salt caverns comparatively quickly, salt caverns are expensive and have smaller total gas storage capacity than do aquifers and depleted oil and natural gas reservoirs (Amid *et al.*, 2016; Salmachi *et al.*, 2024; Alinejad *et al.*, 2024).

Aquifers

Aquifer storage is appealing because aquifers are prevalent in all sedimentary basins and have a very large storage capacity. On the other hand, aquifer storage is associated with undesirable reactions

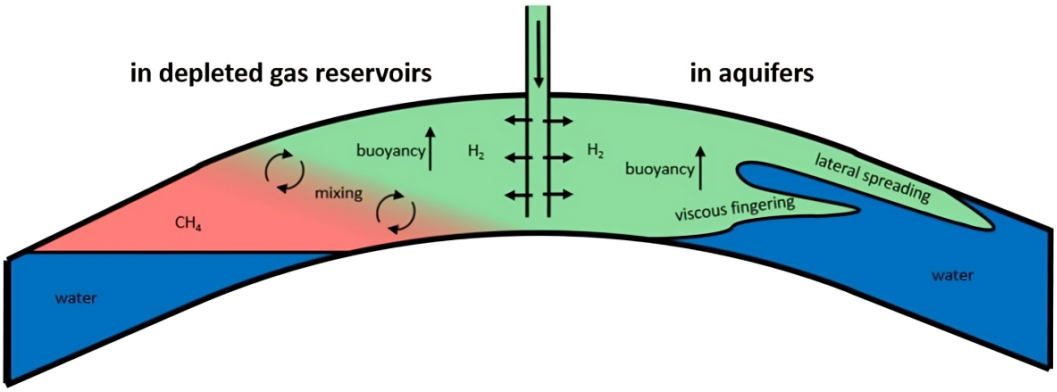

Figure 1.2: [Colour] Schematic of the hydrodynamic effects and gas mixing in an underground hydrogen storage facility. Adapted from Michelsen *et al.* (2023) and used with permission.

leading to the production of gases such as CH_4 with commensurate loss of hydrogen (Tarkowski, 2019). Also, UHS in aquifers is even more expensive than that in salt caverns (Tarkowski, 2019). The high mobility contrast between hydrogen and brine in aquifers increases the possibility of viscous fingering instabilities, which can cause hydrogen to bypass much of the pore space depending on the geological characteristics of the formation – see figure 1.2. This may lead to uncontrolled hydrogen spreading in aquifers and reduce the average hydrogen saturation within the pore spaces (Jafari Raad *et al.*, 2022). Additionally, hydrogen's high buoyancy compared to the resident formation brine creates a strong upward migration (gravity segregation), driven by the large density contrast. While gravity segregation can effectively separate injected hydrogen from the formation brine, it also heightens the risk of uncontrolled subsurface migration, hydrogen leakage, and loss (Jafari Raad *et al.*, 2022).

Depleted reservoirs

Hydrogen storage in depleted gas and oil reservoirs involves using existing underground formations, which previously contained natural gas or oil, to store hydrogen. This method leverages the infrastructure and geological characteristics that are already in place, providing a potentially cost-effective and large-scale storage solution. Oil reservoirs involve more complexity in terms of contamination and infrastructure modification.

Here, we consider hydrogen storage in depleted reservoirs wherein existing infrastructure in the form of pipelines, etc. may often be leveraged to reduce capital costs. In particular, we focus on depleted natural gas reservoirs for which chemical reactions between hydrogen and residual oil are avoided. Throughout the hydrogen storage cycle, the gas that is permanently held in the reservoir is referred to as the cushion gas. It maintains the parameters needed for proper functioning of the storage medium, such as pressure range, flow rate, and avoiding withdrawal contamination. When hydrogen is injected into reservoirs, a portion of it may mix with the cushion gas, as illustrated in Figure 1.2, or dissolve in the existing water. This fraction of hydrogen becomes trapped underground and cannot be withdrawn in its pure state. Amid *et al.* (2016) reported that hydrogen loss due to dissolution or diffusion into water from underlying aquifers is insignificant. However, the authors stated that losses resulting from the mixing of hydrogen and cushion gas in the reservoir needs to be quantified more carefully. Feldmann *et al.* (2016) identified mechanical dispersion, along with density differences, and molecular diffusion, as the most significant factors contributing to gas-gas mixing during UHS in gas reservoirs. Effective molecular diffusion is regarded as a slow process in comparison to mechanical dispersion in advective or convective transport (Tek, 1989). Feldmann *et al.* (2016) and Sahu & Neufeld (2023) also reported that mechanical dispersion is more severe in heterogeneous reservoir where hydrogen can leak to other layers. There is considerable uncertainty surrounding the mixing of hydrogen and cushion gas in depleted gas reservoirs, particularly in terms of the parameters and mechanisms influencing hydrogen dispersivity. This has led to a significant knowledge gap in this area.

The hydrodynamic behaviour of hydrogen coupled with formation heterogeneities make it difficult to simulate the precise details of hydrogen migration. Moreover, tracking the movement of the injectate plume in hydrogen storage operations can be costly. Therefore, it is imperative to create realistic conceptual models of hydrogen flow, drainage, and dispersion in order to guide crucial procedures involved in the techno-economic assessment of hydrogen storage projects. To this end, and in the interests of simplicity, we defer to future investigations consideration of additional effects such as viscous fingering, capillary effects, bio-geochemical reactions and, when residual liquid may be present, capillarity, dissolution and chemical reaction. On the other hand, we do specifically

consider the technical details of dispersion and buoyancy-driven flow, as is appropriate when considering the flow evolution away from the point of injection. Throughout, and unless otherwise noted from this point forward, we assume an injectate that is dense relative to the surrounding ambient fluid. Although this description does not apply to the case of hydrogen storage, the above assumption makes our study consistent with key seminal works e.g. that of Huppert & Woods (1995) discussed below. And, in any event, there is no difference, dynamically-speaking, between a dense vs. buoyant injectate provided density contrasts are relatively modest so that the Boussinesq approximation applies. Thus do we illuminate key physical processes in a framework that becomes independent of orientation in the Boussinesq limit of small density contrast. The Boussinesq approximation allows us to assume that viscosity is independent of buoyancy/concentration effects, leading to the simplification of treating the viscosity as constant for both the mixed and unmixed fluids.

1.3 Buoyancy-driven flow in porous media

Buoyancy-driven flow is mainly governed by density differences, stemming from either temperature and/or concentration gradient. When a denser fluid is placed above a lighter fluid within a porous medium, gravity acts on the density difference, causing the denser fluid to sink while the lighter fluid rises. This movement creates flow patterns within the porous medium. Such flow patterns might be a primarily vertical, downward or upward, plume or a primarily horizontal gravity current – see figure 1.3 (Note that Figure 1.3(a) shows a primarily vertical flow with no barriers obstructing the downward movement whereas in figure 1.3(b) an impermeable layer causes the fluid to spread out as a gravity current).

The dynamics of buoyancy-driven flow in porous media are influenced by several factors, i.e.

- **Density contrast ($\Delta\rho$)**: The density difference between the fluids involved in the flow strongly influences the magnitude of the buoyancy force and thus the flow rate.
- **Porous Medium Properties**: The porosity (ϕ), permeability (k), and pore structure of

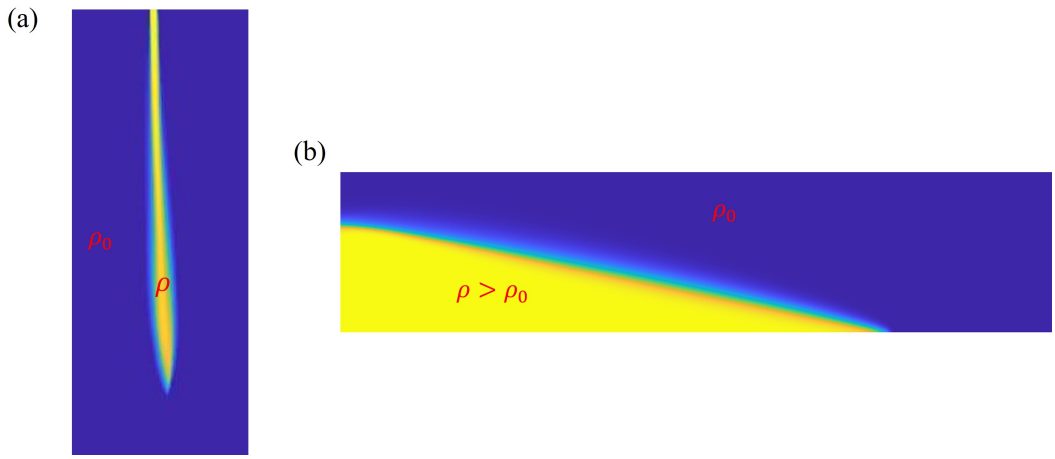

Figure 1.3: [Colour] (a) Dense plume and (b) dense gravity current with density ρ within a uniform porous medium. This figure is generated by running COMSOL simulations of the type described in Chapter 2 and Chapter 3.

the medium greatly influence the flow behavior. Highly permeable and well-connected pore networks facilitate faster fluid movement.

- **Fluid properties**: The viscosity (ν) and other properties of the fluids involved affect their ability to flow through porous media.

- **Boundary conditions**: The presence of impermeable/semi-permeable boundaries or other obstructions can alter the flow patterns and affect the overall behavior of buoyancy-driven flow in porous media.

Accordingly, porous media flows typically are categorized by two non-dimensional numbers: the Reynolds number, $\mathrm{Re} = \frac{Ud_o}{\nu}$, and Péclet number, $\mathrm{Pe} = \frac{Ud_o}{D_{\mathrm{mol}}}$, where U is a characteristic velocity, d_o is a characteristic length characteristic of the pore size and D_{mol} is molecular diffusion. The Reynolds number indicates the proportion of inertia compared to viscous dissipation. If $\mathrm{Re} < 10$, the flow is Darcy and momentum conservation follows Darcy's law; however, flow deviates from Darcy's law when $\mathrm{Re} > 10$. In this $\mathrm{Re} > 10$ scenario, inertial effects must be incorporated in the momentum conservation equation. Alternatively, the Péclet number compares mass transport by mechanical dispersion to mass transport by molecular diffusion. If $\mathrm{Pe} \ll 1$ molecular diffusion is the dominant factor over mechanical dispersion, whereas when $\mathrm{Pe} \gg 1$, mechanical dispersion

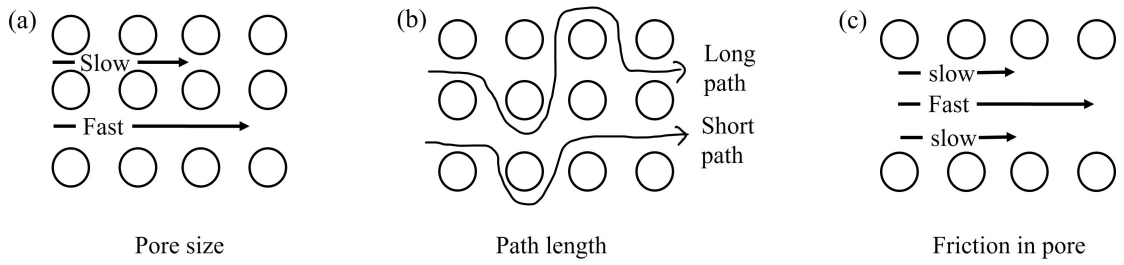

Figure 1.4: Physical mechanisms cause dispersion in porous media.

takes precedence. Dispersion is the macro-scale manifestation of pore-scale mechanisms that cause fluid particles, originally adjacent, to spread apart from one another. Such mechanisms are (i) a difference of fluid velocity in pores with different sizes (figure 1.4a); (ii) a difference of flow path length (figure 1.4b); and (iii) a difference in fluid velocity owing to position within a pore in a pore channel (figure 1.4c) (Bear, 1972). Dispersion can mix fluid in the direction of the flow in which case it is referred to as longitudinal dispersion. Alternatively, dispersion can mix perpendicular to the flow direction in which case it is referred to as transverse dispersion (Bear, 1972).

Understanding buoyancy-driven flow in porous media is crucial for various applications, including underground hydrogen storage, geological CO_2 sequestration, groundwater management, oil and gas recovery, and geothermal energy production. Given this critical importance, researchers have been exploiting mathematical models, laboratory experiments, and numerical simulations to study and predict the behavior of porous media buoyancy-driven flow and to develop strategies for its control and optimization.

1.3.1 Literature review

Plume

Wooding (1963) derived similarity solutions for laminar plumes in porous media under the assumption of a Darcy's flow with a Péclet number $\mathrm{Pe} \ll 1$, such that flow is diffusion dominant. For both rectilinear and axisymmetric geometries, the formulas for the plume volume flux are provided as

follows:

$$\text{Rectilinear}: \; Q = \left(\frac{36\, D_{\text{mol}}\, \phi\, F_0\, k\, \Lambda^2\, z}{\nu}\right)^{1/3}, \quad \text{and} \quad \text{Axisymmetric}: \; Q = 8\,\pi\, D_{\text{mol}}\, \phi\, z\,, \tag{1.1}$$

where F_0 is the source buoyancy flux and Λ is the source width perpendicular to the paper. Meanwhile z is the vertical distance from the source. Equation (1.1) illustrates how the plume volume flux increases with distance from the source in the porous medium, with the dependency on the permeability and porosity of the medium.

Wooding's solution was later extended to dispersion dominant flow by Sahu & Flynn (2015) for infinite porous media, and by Gilmore *et al.* (2021) for semi-infinite porous media, which is confined by an impermeable vertical boundary at the injection elevation. The former study suggests the following expressions for volume flux and reduced gravity of a rectilinear plume:

$$Q = \left[\left(\frac{16\, F_0\, k\, \Lambda}{\pi\, \nu}\right)^2 a_T\, \phi\, z\right]^{1/4}, \tag{1.2a}$$

$$g' = \left[\left(\frac{\pi\, F_0\, \nu}{16\, k\, \Lambda}\right)^2 \frac{1}{a_T\, \phi\, z}\right]^{1/4}, \tag{1.2b}$$

respectively. Here, a_T is the transverse dispersivity. The latter study reports the following relationships for plume volume flux and reduced gravity:

$$Q = \left[\left(\frac{8\, F_0\, k\, \Lambda}{\pi\, \nu}\right)^2 a_T\, \phi\, z\right]^{1/4}, \tag{1.3a}$$

$$g' = \left[\left(\frac{\pi\, F_0\, \nu}{8\, k\, \Lambda}\right)^2 \frac{1}{a_T\, \phi\, z}\right]^{1/4}, \tag{1.3b}$$

respectively. These results illustrate that the dispesivity coefficient becomes important rather than diffusion coefficient when flow is dispersion dominant.

Gravity current

Huppert & Woods (1995) conducted a seminal study of gravity current flow in porous media, specifically analyzing a two-dimensional rectilinear geometry along an impermeable boundary with

an arbitrary slope angle, θ. Assuming a hydrostatic pressure distribution and using Darcy's law, the authors derived an equation for the gravity current along-slope velocity, u, which reads

$$u = -\frac{kg'}{\nu}\Big(\frac{\partial h}{\partial x}\cos\theta - \sin\theta\Big)\,, \tag{1.4}$$

where ν is the kinematic viscosity, $g' = g\,\Delta\rho/\rho$ is the reduced gravity and h is the gravity current height. Huppert & Woods (1995) averaged the mass conservation equation in the gravity current perpendicular to the slope and obtained the following evolution equation for h:

$$\phi\,\frac{\partial h}{\partial t} - \frac{kg'}{\nu}\frac{\partial}{\partial x}\Big[\Big(\frac{\partial h}{\partial x}\cos\theta - \sin\theta\Big)\,h\Big] = 0\,. \tag{1.5}$$

Lyle *et al.* (2005) expanded Huppert and Woods's findings to axisymmetric gravity currents with $\theta = 0°$. They found that the horizontal velocity measured in axisymmetric coordinates is

$$u = -\frac{kg'}{\nu}\,\frac{\partial h}{\partial r}\,, \tag{1.6}$$

in which r indicates radial direction. Therefore, (1.5) becomes

$$\phi\,\frac{\partial h}{\partial t} - \frac{kg'}{\nu}\,\frac{1}{r}\,\frac{\partial}{\partial r}\Big(r\frac{\partial h}{\partial r}h\Big) = 0\,. \tag{1.7}$$

Although (1.5) and (1.7) share some similarities –both of them are non-linear heat equations– their predictions are not the same. Thus does a gravity current spread as $t^{2/3}$ and its height varies as $t^{1/3}$ in a rectilinear geometry while the gravity current (with the identical source and initial conditions) spreads as $t^{1/2}$ and its height is constant with time in an axisymmetric scenario. Later, Nordbotten *et al.* (2005) and Pegler *et al.* (2014) studied gravity currents within the vertically-confined porous media. Their research revealed that confinement introduces fundamentally different dynamics compared to unconfined porous media. While the ambient fluid effects are not important for gravity currents spreading in unconfined media (Huppert & Woods, 1995), vertical confinement contributes ambient flow effects due to the restriction on the total thickness of the exchange flow. As a result of the ambient counter flow, the dense gravity current is retarded, and the ambient fluid

viscosity becomes significant in confined settings. According to Pegler *et al.* (2014) for a porous media with thickness H, the two equations for the gravity current flow and ambient flow are given by

$$\phi\,\frac{\partial h}{\partial t} - \frac{k}{\mu}\frac{\partial}{\partial x}\Big(h\frac{\partial P}{\partial x}\Big) = 0\,, \tag{1.8a}$$

$$\frac{\partial}{\partial x}\Big[\Big(\frac{k}{\mu}h + \frac{k}{\mu_a}(H-h)\Big)\,\frac{\partial P}{\partial x} - \frac{kg'}{\nu_a}(H-h)\frac{\partial h}{\partial x}\Big] = 0\,. \tag{1.8b}$$

Here, subscript 'a' indicates ambient fluid. Equations (1.8a) and (1.8b) form a coupled hyperbolic-elliptic system for h and P, where the latter variable denotes the background pressure due to the ambient counter flow.

In the geological context, gravity currents could potentially extend along cap rock, exposing pathways for leakage. The leakage associated with gravity currents may be either localized (such as through a discrete fracture) or distributed (as through seeping into a lower layer characterized by relatively low permeability). Upon fluid drainage from the gravity current underside, (1.5) modifies to

$$\phi\,\frac{\partial h}{\partial t} - \frac{kg'}{\nu}\frac{\partial}{\partial x}\Big[\Big(\frac{\partial h}{\partial x}\cos\theta - \sin\theta\Big)\,h\Big] = w_d\,, \tag{1.9}$$

where $w_d\,(<0)$ is the drainage velocity within the gravity current. Pritchard (2007) modeled gravity current flow within a porous medium over a cap rock layer intersected by line fissures. This model employed numerical integration to describe drainage driven by the hydrostatic pressure from the fluid column above the fissure(s). For the same source and initial conditions as described above, the authors found that leading edge of the gravity current spreads as $t^{1/2}$, which is slower than the prediction made by Huppert & Woods (Huppert & Woods, 1995). Pritchard (2007) proposed that entirely draining the gravity current with fractures might be challenging, particularly if the system has a few large fractures instead of many smaller ones. Later, Neufeld *et al.* (2009) expanded the Pritchard (2007) model to examine porous media gravity current flow over a single line fissure. They considered a fissure of width W and permeability k_f positioned a distance x_f from the source.

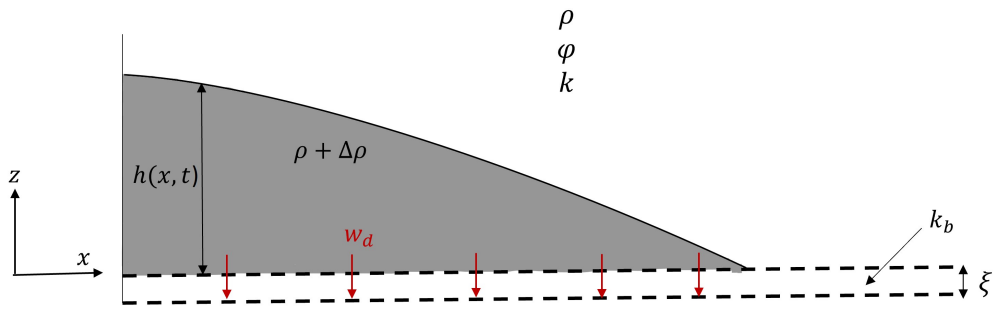

Figure 1.5: Gravity current over a narrow permeable layer.

They assumed that $W \ll x_f$ and expressed the vertical draining velocity within the fissure as

$$w_d = -\frac{k_f\, g'}{\nu}\left(1 + \frac{h}{\xi}\right), \tag{1.10}$$

in which ξ indicates the fissure thickness. The authors then validated the above expression by comparing it with the outcomes of a Hele-Shaw cell experiment. Farcas & Woods (2013) found that when multiple fractures are present in the boundary, the system ultimately behaves like a scenario with distributed drainage from the gravity current through a permeable layer with permeability k_b, which is given by

$$k_b \simeq \int_0^W (k_f / D_f)\, \mathrm{d}x\,. \tag{1.11}$$

Here, D_f is the distance between fractures. For the case of distributed drainage, Pritchard *et al.* (2001) modeled the drainage term by considering leakage along a thin semi-permeable layer – see figure 1.5. They assumed the permeability of this thin layer $k_b \ll k$ and its thickness, ξ, to be much smaller than the ambient thickness. Therefore, the drainage velocity becomes

$$w_d = -\frac{k_b\, g'}{\nu}\left(1 + \frac{h}{\xi}\right). \tag{1.12}$$

Here, the drainage velocity is similar to that in Neufeld *et al.* (2009) but distributed rather than localized at a fissure. Goda & Sato (2011) increased the depth of the lower/draining layer and modeled the drainage from the gravity current through a deep permeable layer. By doing so, the depth of the drained fluid in the lower layer, $l(x,t)$, should be considered when deriving an

expression for the drainage velocity. Accordingly, their revised theoretical estimate for w_d reads

$$w_d = -\frac{k_b\, g'}{\nu}\left(1 + \frac{h}{l}\right). \tag{1.13}$$

Goda & Sato (2011) ignored ambient fluid entrainment into the drained fluid in the lower layer. As a result, the reduced gravities g' in the upper and lower layers are equal. However, Rayleigh–Taylor-type instabilities in the lower layer cause a significant entrainment of ambient fluid into the drained fluid. Therefore, Sahu & Flynn (2017) accounted for entrainment in the lower layer and defined different reduced gravities for the upper layer, g'_u, and for the lower layer, g'_l. Subsequently, (1.13) was modified to

$$w_d = -\frac{k_b\, g'_l}{\nu}\left(1 + \frac{g'_u}{g'_l}\,\frac{h}{l}\right). \tag{1.14}$$

The authors suggested an empirical correlation for g'_l/g'_u experimentally based on source reduced gravity and volume flow rate. Later, Bharath *et al.* (2020) extended the Sahu & Flynn (2017) model for inclined gravity currents with arbitrary inclination angle, θ. They expressed the drainage velocity as

$$w_d = -\frac{k_b\, g'_l}{\nu}\left(1 + \frac{h}{l}\cos\theta\right). \tag{1.15}$$

Although it is mentioned in sections 1.1 and 1.2.2 that mass transfer between ambient and injected fluid is important in the context of CO_2 sequestration and underground hydrogen storage, all the aforementioned studies consider a sharp interface and therefore exclude the possibility of mass transfer by dispersion. Sahu & Neufeld (2020), theoretically and experimentally, studied mixing in horizontal porous media gravity currents elongating over an impermeable boundary. They demonstrated that considerable mixing between the gravity current and the surrounding ambient fluid takes place as a result of mechanical dispersion. Looking to incorporate these observations into a theoretical model, Sahu & Neufeld (2020) only considered the transverse component of dispersion and ignored its longitudinal counterpart to quantify the dispersive mixing in the gravity current.

Based on their theoretical model, the amount of ambient fluid mixed into the gravity current is

$$V_e = \alpha \Big(\frac{q\, k\, g'}{\nu \phi^2} \Big)^{2/3} t^{4/3}\,, \tag{1.16}$$

in which q is source volume flux and α is the dispersive entrainment coefficient. They conducted dye-attenuation-based laboratory experiments and estimated $\alpha \simeq 0.01$ for the case where there is no drainage of gravity current fluid. Their theoretical model was thereby validated against the experimental outcomes. Sahu & Neufeld (2020) anticipated that α and subsequently V_e increase when the gravity current experiences drainage. Therefore, Sahu & Neufeld (2023) conducted an experimental study on the behavior of gravity currents in multi-layered porous media to investigate the effects of heterogeneity and drainage on dispersive mixing. Their study revealed that the existence of transverse gravity-induced fingers and a leading blunt edge within layered materials intensify the mixing within gravity currents. Sahu & Neufeld (2023) presented semi-empirical formulas based on their experimental measurements. These semi-empirical equations can be used to predict the dynamics of gravity current flow and mixing in a heterogeneous medium on a significantly larger scale by accurately specifying the depth-averaged parameters and 'jump factors' that characterize the heterogeneity of the medium.

1.4 Knowledge gap

The inherent characteristics of porous media within a majority of geological formations typically remain unknown, and the monitoring of fluid flow incur substantial expenses. Consequently, researchers and engineers benefit greatly from simplified theoretical frameworks and statistical methodologies to comprehend and predict the fluid behavior within these geological structures. Despite progress by various researchers, as outlined in section 1.3, there is still substantial room for enhancing the capacity to predict the patterns in buoyancy-driven flows in relation to CO_2 sequestration or underground hydrogen storage. Notably, compared to the extensive research on gravity currents supporting a sharp interface, the mixing in gravity currents is far less thoroughly explored. As the benefits and challenges of depleted reservoir storage are mentioned in section

1.2.2, we aim to investigate mixing due to mechanical dispersion in miscible porous media gravity currents that is relative to flow in depleted gas reservoirs. We specifically focus on UHS rather than CO_2 sequestration because (i) CO_2 has been much more thoroughly studied and industrial projects have been up and running for decades, (ii) the decreasing reliance on fossil fuels in the future will eventually reduce the need for CO_2 sequestration. This investigation addresses following knowledge gaps:

1. Previous studies related to dispersive mixing in porous media gravity currents (Sahu & Neufeld, 2020; Sahu & Neufeld, 2023) did not predict the mixing zone clearly by separating bulk and dispersed fluid phases. However, in practical applications and as depicted in figure 1.2, figure 5 of Feldmann *et al.* (2016) and figure 3 e of Sahu & Flynn (2017), the mixing zone is a vital parameter in leaky gravity currents because the fluid in the mixing zone likely will not be recovered owing to the high capital and operating costs of surface separation facilities. Therefore, to predict the dispersive mixing behaviour in a porous media gravity current, it is necessary to assign an interface between the bulk and dispersed phases. This distinction between bulk and dispersed fluid can quantify the amount of dispersion within gravity currents. Once the requisite theoretical scaffolding is in place, the effects of parameters e.g. source conditions and mass loss by drainage on the amount of dispersion can be investigated.

2. In geological contexts, the orientation of porous layers is generally influenced by the topography of the landscape and can often be inclined at a certain angle, as depicted in figure 1.1. This inclination can significantly affect the dynamics of fluid flow through these layers. Sahu & Neufeld (2020) and Sahu & Neufeld (2023) investigated the dispersive mixing in horizontal gravity currents. However, inclined boundaries may lead to non-trivial interactions between gravity and the non-uniform permeability in the media, potentially resulting in different mixing rates. Further research is required to understand how these inclined layers impact fluid flow and mixing.

3. In the context of leaky porous media gravity currents, various real-world scenarios exist where

fluid flow encounters localized or distributed drainage. For instance, faults or fractures in cap rocks can cause local drainage by providing distinct, high permeability pathways for fluids to escape. Distributed drainage, on the other hand, occurs throughout sedimentary layers as fluids progressively drain through the (tight) porous matrix. To the best of our knowledge, there are currently no thorough theoretical works that address dispersive mixing in porous media gravity currents that experience either distributed or local drainage.

4. Although it is suggested by Sahu & Neufeld (2023) that their semi-empirical formulations can be applied to geological scales, real underground storage sites exhibit a wide range of geological conditions, including varying layer orientations, thermodynamic conditions, and complex interactions between the injectate and ambient fluid. These factors can significantly alter the flow dynamics and mixing behavior as predicted even in simplified theoretical models and controlled experimental setups. No thorough investigation has been conducted to confirm whether the findings of studies on dispersive mixing in buoyancy-driven gravity currents can be successfully applied to practical uses such as underground hydrogen storage.

We will therefore deploy a gravity current model that is similar to, but more detailed than, that leading to (1.9). In so doing, we implicitly make the following set of assumptions: (i) flow velocities are sufficiently small and Reynolds numbers sufficiently modest that the porous media flow is appropriately modeled as Darcy, (ii) the gravity current is long and thin such that the pressure distribution within the gravity current is hydrostatic, (iii) the Péclet number is sufficiently large, allowing us to ignore diffusion relative to mechanical dispersion, (iv) the density difference is solely attributed to concentration, while the effect of pressure on density difference is disregarded.

1.5 Thesis outline

In this thesis, we fill in the gaps in our understanding as mentioned in section 1.4 by applying theory and CFD methods. To this end, the thesis has three goals. These are (i) Utilize a theoretical model describing the flow of a miscible gravity current subject to local drainage to identify key dispersion-

influencing parameters (e.g. those associated with the source vs. fissure). (ii) Extend the preceding analysis to include a gravity current experiencing distributed drainage. (iii) Apply our findings to practical instances of underground hydrogen storage, this for the purposes of evaluating the strengths and weaknesses of our analytical models vis-à-vis engineering operations in the field. Accordingly, chapter 2, chapter 3 and chapter 4, which are further described below, fulfill these goals.

A simplified hydrodynamic theoretical model is developed in chapter 2 to predict the dispersive mixing behavior of gravity currents subjected to localized drainage. We supplement our theoretical work with similitude CFD simulations conducted using COMSOL in order to assess the accuracy of our theoretical predictions. Such validation is especially important because our theoretical model takes a binary view and assigns gravity current into one of two categories, i.e. bulk vs. dispersed. By measuring the volume of fluid predicted to reside in the dispersed phase, we propose a new metric to assess the degree of mixing. With the metric so defined, we can then assess the relative importance of various control parameters.

In chapter 3, we extend our theoretical framework and COMSOL numerical model to investigate dispersive mixing dynamics in gravity currents experiencing basal distributed drainage through a thin interbed layer. By the integration of theoretical modeling and COMSOL simulations, we examine the behaviour of the drained fluid and its impact on the gravity current mixing. Key parameters on the mixing dynamics of the leaky gravity currents are studied using the metric from the previous chapter.

In chapter 4, we model the process of hydrogen storage in depleted gas reservoirs using sophisticated reservoir simulation software, namely CMG and OpenGoSim. Our primary objective is to assess the applicability and accuracy of the reduced-order hydrodynamic model of chapter 3 in predicting the behavior of actual geological flows. In addition to validating our theoretical model, we extend our investigation to explore mixing behaviors in flow scenarios that go beyond the original scope of the theoretical model. We specifically study the dynamics of hydrogen flow and mixing in confined reservoirs, where the flow is constrained by impermeable layers or boundaries, and in

anticline reservoirs.

Chapter 5 provides a summary of the major conclusions and ideas for future research that stem from the current analysis.

Chapters from this thesis have been published and presented at various conferences/symposiums. A relevant summary is given in tables 1.1 and 1.2 below.

Table 1.1: Scientific contributions of this thesis.

Chapter	Journal	Status	Co-author(s)
2	*J. Fluid Mech.*	Published	M. R. Flynn, C. K. Sahu
3	*J. Fluid Mech.*	Published	M. R. Flynn
4	*Int. J. of Hydrogen Energy*	Submitted	M. R. Flynn

Table 1.2: List of scientific meetings at which the author has presented portions of this thesis. Abbreviations are as follows: APS - DFD: American Physical Society - Division of Fluid Dynamics, IGR: Institute of Geophysical Research, FEGRS: The Faculty of Engineering Graduate Research Symposium. Furthermore, Interpore is an annual conference organized by the International Society of Porous Media.

Chapter(s)	conferences/symposiums	Location	Month and Year
2	13^{th} Interpore	Online	May-June 2021
2	APS - DFD	Online	Nov. 2022
2, 3	15^{th} Interpore	Edinburgh, Scotland	May 2023
3	FEGRS	Univ. of Alberta	Aug. 2023
3, 4	16^{th} Interpore	Online	May 2024
2, 3, 4	IGR Symposia	Univ. of Alberta	Nov. 2022, Apr. 2023 Nov. 2023, Apr. 2024

Chapter 2

Dispersion effects in porous media gravity currents experiencing local drainage [1]

2.1 Abstract

We develop a theoretical model to study (dense) two-dimensional gravity current flow in a laterally extensive porous medium experiencing leakage through a discrete fissure situated along this boundary at some finite distance from the injection point. Our model, which derives from the depth-averaged mass and buoyancy equations in conjunction with Darcy's law, considers dispersive mixing between the gravity current and the surrounding ambient by allowing two different gravity current phases. Thus do we define a bulk phase consisting of fluid whose density is close to that of the source fluid and a dispersed phase consisting of fluid whose density is close to that of the ambient. We characterize the degree of dispersion by estimating, as a function of time, the buoyancy of the dispersed phase and the separation distance between the bulk nose and the dispersed nose. On this basis, it can be shown that the amount of dispersion depends on flow conditions upstream of the fissure, the fissure permeability, and the vertical and horizontal extent of the fissure. We also show that dispersion is larger when the gravity current propagates along an inclined barrier rather than along a horizontal barrier. Model predictions are fitted against numerical simulations. The

[1] Sheikhi. S., Sahu, C. K. & Flynn, M. R. 2023 Dispersion effects in porous medium gravity currents experiencing local drainage. *J. Fluid Mech.* **975**, A18.

simulations in question are performed using COMSOL and consider different inclination angles and fissure and upstream flow conditions. Our study is motivated by processes related to underground H_2 storage (UHS) e.g. an irrecoverable loss of H_2 when it is injected into the cushion gas saturating an otherwise depleted natural gas reservoir.

2.2 Introduction

Among possible substitutes for hydrocarbon fuels, hydrogen has a high energy density and can be converted into heat or electricity without emitting CO_2 (Andrews & Shabani, 2012). Although there is an obvious incentive to generate hydrogen from renewables, it is difficult to do so on a temporally-consistent basis given the variability of e.g. wind forcing and solar radiation. As such, options for H_2 storage must be pursued so that H_2 produced in excess may be stored then used when demand outstrips supply (Sainz-Garcia *et al.*, 2017). An appealing option for H_2 storage, particularly when considering large volumes of H_2, may be underground storage (Panfilov, 2016). The technical and economic feasibility of underground H_2 storage (UHS) has been studied in various locales e.g. Bulgaria, United States, United Kingdom, Poland, Spain and Turkey (Flesch *et al.*, 2018). Here, we consider UHS in the context of depleted reservoirs. In particular, we focus on depleted natural gas reservoirs, which avoid a possible contamination of H_2 by the longer chain organic molecules present in depleted oil reservoirs.

UHS in depleted natural gas reservoirs requires cushion gas, gas stored permanently in formation to maintain pressure for optimum injection and withdrawal. Although the cushion gas may be H_2, it is more typically a dissimilar (heavier) gas such as CO_2 or N_2 (Feldmann *et al.*, 2016). Thus H_2 injection into cushion gas may be associated with significant mixing, whether due to diffusion or dispersion. Mixing may be exacerbated by buoyancy effects, which result from the small size of the H_2 molecule. In turn, H_2 has a high mobility in formation and may therefore travel long lateral distances or else leak into adjoining stratigraphic layers (Lubon & Tarkowski, 2021). Leakage often arises from local fault(s), which act as pathways through otherwise impermeable layers – see e.g. Flett *et al.* (2005). Complicating matters are the facts that (i) local faults may prove difficult

to detect in surveys, and, (ii) monitoring injectate migration in UHS operations is nontrivial and expensive. There is a need, therefore, for tractable conceptual models of buoyancy-driven flow, drainage and dispersion that may inform key processes important to the techno-economic evaluation of UHS projects. Of course, such conceptual models might additionally consider effects such as viscous fingering, capillary effects, bio-geochemical reactions and, when residual liquid is present, capillarity, dissolution and chemical reaction. However, and in the interests of simplicity, we do not examine such additional effects here.

Another possible application of our work is to CO_2 sequestration. In this related (and better-studied) problem, one likewise considers the eventual fate of a fluid that is injected at high pressure into a porous medium. Similar to UHS, the success of CO_2 sequestration relies, in part, on considerations of the mixing (e.g. by dissolution c.f. MacMinn *et al.* 2012; Khan *et al.* 2022) between the injectate with the ambient fluid (i.e. brine) that occupies the pore space. CO_2 sequestration flows are, however, complicated by surface tension effects and the possibility of capillary trapping, which arise because of the relative immiscibility of CO_2 and brine.

Buoyancy-driven flow in porous media is bookended by two canonical scenarios: a vertically ascending or descending plume and a horizontally-propagating gravity current. Wide attention has been devoted to gravity current flow in porous media since the seminal work of Huppert & Woods (1995), who studied the evolution of finite releases of fluid propagating in an expansive rectilinear porous medium. They considered that (dense[2]) fluid moves under gravity along either horizontal or inclined boundaries and through a medium whose permeability is either uniform or else changes normal to the lower (impermeable) boundary. Huppert and Woods's analysis was extrapolated to axisymmetric geometries by Lyle *et al.* (2005). Further extensions to Huppert & Woods's work have considered gravity current flow in shallow porous media (MacMinn *et al.*, 2012; Pegler, Huppert & Neufeld, 2014), through horizontally heterogeneous media (Zheng, Christov & Stone, 2014), and through layered porous media that are either horizontal (Pritchard *et al.*, 2001;

[2]For analytical convenience, many previous studies assume that the gravity current density is larger than that of the surrounding ambient. To be consistent with this earlier body of research, a similar assumption shall be adopted here. In this respect, the gravity currents to be described quantitatively in e.g. section 2.3 are "upside-down" relative to those expected in real UHS operations.

Goda & Sato, 2011; Sahu & Flynn, 2017), or else make an angle to the horizontal (Bharath *et al.*, 2020). Studies have further considered non-Newtonian gravity currents (Ciriello *et al.*, 2016) and gravity currents consisting of fluid having spatially-variable densities (Pegler, Huppert & Neufeld, 2016).

Notable in the above summary of previous research are investigations involving a leakage of fluid from the gravity current underside. This leakage may be either localized (e.g. through a discrete fissure) or else distributed (e.g. into a lower layer of comparatively small permeability). Pritchard (2007) modeled gravity current flow in a porous medium with a series of line fissures in which drainage is due to the hydrostatic pressure exerted by the column of gravity current fluid situated directly above a particular fissure. Neufeld *et al.* (2009) expanded this analysis by additionally considering the weight of the dense fluid inside and below the fissure. More recently, Gilmore *et al.* (2021) combined Neufeld et al.'s description with the plume solution of Sahu & Flynn (2015) to study flow in faults cross-cutting multiple aquifers. Meanwhile Avci (1994) studied local drainage in separated confined aquifers taking into account the effect of the injection pressure and the natural contrast of hydraulic head in two separated aquifers. Nordbotten *et al.* (2004) extended Avci's work for multiple abandoned leaky wells. The above studies mostly invoke a sharp interface approximation and so ignore mass transfer between gravity currents and the surrounding ambient fluid e.g. through dissolution, diffusion or dispersion. However, in miscible flow e.g. gas reservoir storage of H_2, the numerical simulations of Feldmann *et al.* (2016) indicate that mixing between the injected and ambient fluids may be nontrivial. As we shall see, this feature becomes more prominent in the presence of draining.

Mixing in porous media involves dispersion and diffusion. Diffusion is a process driven at the molecular scale by concentration differences while dispersion is advection-driven and is related to the macro-scale flow phenomena. Dispersion in a porous medium is influenced by the grain characteristics in several ways: the pore size affects the tortuosity of flow paths; variations in channel width alter the velocity distribution within the pores; different grain sizes modify the permeability and contribute to medium heterogeneity by creating diverse flow paths; and the surface area variations impact the dispersion process (Bear, 1972). Mathematically, dispersion (D) can be

expressed as $D = a \cdot V$, in which a is dispersivity and V is Darcy velocity. Dispersivity depends on factors such as pressure, temperature, flow velocity, and the tortuosity and heterogeneity of the porous medium (Michelsen *et al.*, 2023). The mixing that occurs between miscible fluids in porous media flow depends on the Péclet number which characterizes the importance of advection to diffusion. Mixing is due to diffusion for $\mathrm{Pe} \ll 1$ and due to dispersion (transverse and longitudinal) for $\mathrm{Pe} \gg 1$ (Delgado, 2007). Studies that explore mixing in the context of buoyancy-driven porous media flow include Szulczewski & Juanes (2013). They examined mixing due to diffusion for lock exchange flows consisting of two fluids in vertically confined permeable rock. Szulczewski & Juanes (2013) showed that if a constant volume of dense fluid is released into light fluid, there is an evolution through the following regimes: (i) diffusion-dominated flow, (ii) slumping in which the interface between the two fluids is sharp and tilts in an S-shaped curve, (iii) slumping in which the interface remains sharp but changes from an S-shaped curve to a straight line, (iv) Taylor slumping where mixing increases due to Taylor dispersion at the aquifer scale and decelerates the flow, and, (v) late diffusion where, similar to (i), transport occurs primarily by diffusion. Hinton & Woods (2018) modeled longitudinal shear dispersion due to a vertical gradient of permeability. They demonstrated that the pattern of longitudinal dispersion depends on a number of factors including (i) the viscosity (or mobility) ratio, and, (ii) the severity of the vertical permeability gradient. Huyakorn *et al.* (1987) considered interfacial mixing associated with sea water intrusions into coastal aquifers. The study of Paster & Dagan (2007) also applied boundary layer approximations and the von Kármán integral method to solve for the velocity-dependent transverse dispersion in sea water intrusions having a non-uniform flux field. Mixing in miscible gravity currents is studied directly by Sahu & Neufeld (2020). In their study, the authors used the depth-averaged mass and buoyancy conservation equations to provide a theoretical model for porous media gravity currents experiencing transverse dispersion only. Theoretically speaking, they determined that the gravity current buoyancy flux can be described by a self-similar solution. However, in contrast to the sharp interface case, the gravity current height and concentration are not self-similar.

A limitation of the study by Sahu & Neufeld (2020) is that it ignored longitudinal dispersion. Furthermore, they considered a dispersed interface only and did not define the bulk interface

separately from the dispersed interface. The gravity current nose position is therefore identical to that predicted by a sharp interface formulation. Sahu & Neufeld's model works well when the lower boundary is impermeable, however, when draining is allowed to occur (either locally or in a distributed fashion), experimental evidence from Sahu & Flynn (2015) (e.g. their figure 3e) and from Bharath *et al.* (2020) shows that a significant separation may arise between the fronts for the bulk and dispersed phases of the gravity current.

Due to these shortcomings in the literature, we seek to provide a theoretical model for porous media gravity current flow where the bulk and dispersed phases are accounted for separately using the depth-averaged mass and buoyancy conservation equations for each phase. Also important is to develop a complementary numerical model (e.g. using COMSOL Multiphysics) to validate our theoretical model. In section 2.3, we derive a theoretical model for gravity currents experiencing dispersion and local drainage. Section 2.4 describes the numerical simulations meant to corroborate model output. In section 2.5, we discuss results and compare the predictions of the theoretical model with those due to the numerical simulations. Section 2.6 illustrates the application of our theoretical model to UHS in depleted reservoirs. Finally, current work is summarized and ideas for future research are outlined in section 2.7.

2.3 Theoretical model

2.3.1 Governing equations

We consider gravity current flow due to a dense fluid injection of density ρ_s along a punctured boundary that makes an angle θ with the horizontal as depicted in figure 2.1. Simplifying assumptions are as follows: (i) Initially, the porous medium is saturated with ambient fluid of uniform density ρ_0. (ii) The source fluid and ambient fluid are incompressible and also miscible i.e. capillary effects can be ignored both in the medium as well as in the fissure. (iii) The gravity current consists of a bulk phase and a dispersed phase both of which remain long and thin such that the gravity current flow is everywhere hydrostatic, i.e. the Dupuit approximation is applicable. In addition,

the depth of the ambient is much larger than the gravity current depth. (iv) Consistent with the Boussinesq approximation, the dynamic viscosity, μ, is independent of concentration and therefore the viscosity of the bulk and dispersed phases are assumed equal. (v) At least until the location of the isolated fissure, the leading edge of the dispersed phase remains close to that of the bulk phase such that negligible drainage of dispersed fluid occurs (vi) Pe $\gg 1$ such that diffusion is ignored. (vii) Broadly analogous to the dissolution study of MacMinn *et al.* (2012), whatever mixing occurs along the bulk-dispersed boundary leaves, within the bulk phase, a core of fluid whose density remains ρ_s. This core of bulk fluid remains upstream of the dispersed phase and, in time, must extend downstream of the fissure.

Following Vella & Huppert (2006), the coordinate system (x, z) associated with the along- and cross-slope directions is obtained by a clockwise rotation of the natural coordinates (X, Z) through an angle θ. The origin of both coordinate systems is coincident with the isolated source, which is indicated by the red dot in figure 2.1. In the analysis to follow, we restrict attention to $x \geq 0$.

If the gravity current experiences local drainage through a fissure situated at $x = x_f$ and having width ξ, the continuity equation as applied to the bulk phase reads

$$\phi \frac{\partial h_1}{\partial t} + \frac{\partial}{\partial x} \int_0^{h_1} u_1 \, \mathrm{d}z = -w_{e1} - w_d \, F(x, x_f, \xi) \,, \tag{2.1}$$

where ϕ is the porosity, h_1 is the height of the bulk phase and w_{e1} and w_d are the Darcy velocities respectively accounting for entrainment from the bulk to the dispersed phase and drainage through the fissure. Meanwhile $F(x, x_f, \xi)$ is a boxcar function centered on the fissure, which is zero everywhere except within the interval $x_f - \frac{\xi}{2} < x < x_f + \frac{\xi}{2}$. Because the pressure is hydrostatic, the bulk phase velocity u_1 does not change significantly in a direction perpendicular to the bottom boundary. Thus u_1 can be considered independent of z in (2.1) (Happel & Brenner, 1991). Accordingly, (2.1) may be simplified to

$$\phi \frac{\partial h_1}{\partial t} + \frac{\partial}{\partial x}(u_1 h_1) = -w_{e1} - w_d \, F(x, x_f, \xi) \,. \tag{2.2}$$

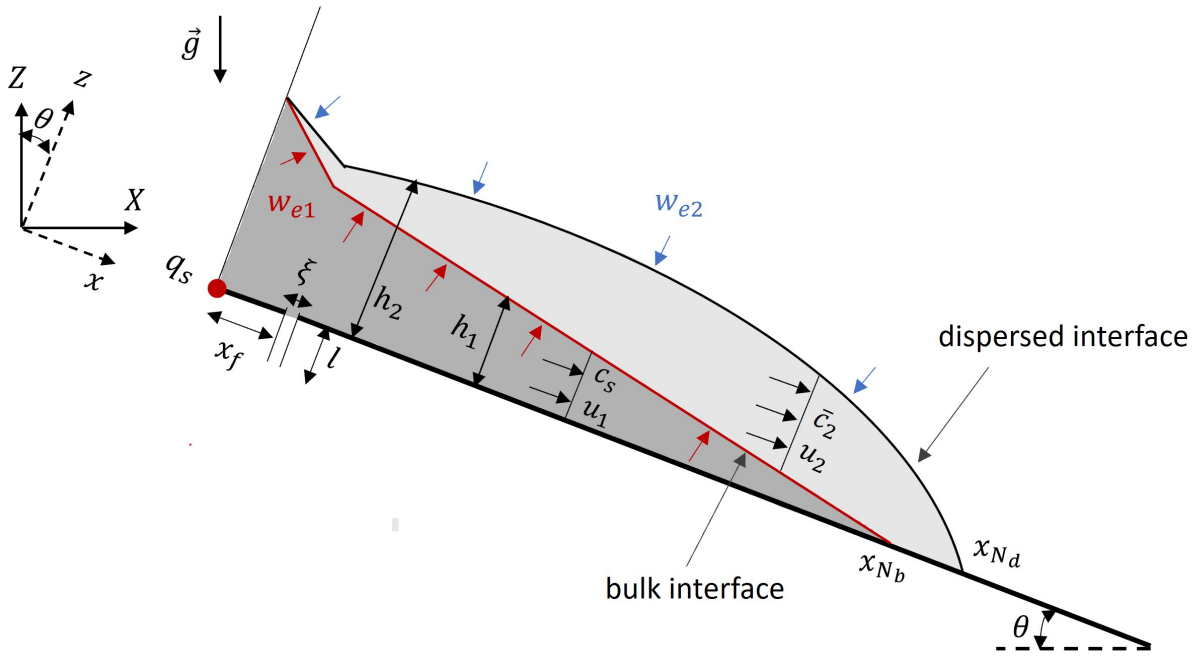

Figure 2.1: [Colour] Schematic of a leaky gravity current propagating along an inclined boundary with local drainage through an isolated fissure. The gravity current consists of bulk and dispersed phases. Variables h_1 (bulk phase height), h_2 (overall height), u_1 (bulk phase velocity), u_2 (dispersed phase velocity), w_{e1} (entrainment velocity from bulk phase), w_{e2} (entrainment velocity from ambient), and $\bar{c}_2$ (average concentration in dispersed phase) are function of x and t. Meanwhile, variables x_{N_b} (bulk phase nose position) and x_{N_d} (dispersed phase nose position) are function of t only.

The solute concentration in the bulk phase is assumed to be equal to the source concentration, c_s; consequently, it is unnecessary to apply a solute conservation equation in the bulk phase.

The continuity equation for the dispersed phase is

$$\phi\frac{\partial(h_2-h_1)}{\partial t}+\frac{\partial}{\partial x}\int_{h_1}^{h_2}u_2\,\mathrm{d}z=w_{e1}+w_{e2}\,, \tag{2.3}$$

in which h_2-h_1 and u_2 are, respectively, the thickness and speed of the dispersed phase. (Note that, consistent with the caption to figure 2.1, u_2 is assumed independent of z). Finally, w_{e2} is the entrainment velocity from the ambient to the dispersed phase. By simplifying and exploiting (2.2), the above result can be rewritten

$$\phi\frac{\partial h_2}{\partial t}+\frac{\partial}{\partial x}\big[u_2(h_2-h_1)\big]=-\frac{\partial}{\partial x}(u_1h_1)+w_{e2}-w_d\,F(x,x_f,\xi)\,. \tag{2.4}$$

Finally, solute conservation in the dispersed phase provides

$$\phi \frac{\partial}{\partial t} \int_{h_1}^{h_2} c_2 \, \mathrm{d}z + \frac{\partial}{\partial x} \int_{h_1}^{h_2} u_2 c_2 \, \mathrm{d}z = w_{e1} c_s \, . \tag{2.5}$$

Here, w_{e1} is defined only over the interval $0 \leq x \leq x_{N_b}$ (see figure 2.1). By defining the dispersed phase buoyancy as $b_2 = \overline{c}_2 (h_2 - h_1)$, in which $\overline{c}_2$ is the z-averaged solute concentration in the dispersed phase, (2.5) can be further simplified to

$$\phi \frac{\partial b_2}{\partial t} + \frac{\partial}{\partial x} (u_2 b_2) = w_{e1} c_s \, . \tag{2.6}$$

Because the bulk buoyancy, $b_1 = c_s h_1$, equals the source buoyancy, solute conservation in the bulk phase is trivial.

Similar to the classical entrainment hypothesis that was proposed for flow in free jets by Ellison & Turner (1959), we consider that the entrainment of ambient fluid is proportional to the gravity current characteristic velocity. This entrainment hypothesis explains the inclusion of ambient fluid into and mixing it with a free shear jet, driven by differences in velocity, as the jet traverses the surrounding medium. The entrainment velocity is perpendicular to the interface between the jet and the ambient fluid, and is assumed to be a linear function of the jet's velocity. Of greater relevance to buoyancy-driven flow in porous media, Sahu & Neufeld (2020) also used a linear relationship between the entrainment and characteristic velocities in their study of dispersive gravity currents. Motivated by this latter work most especially, we define $w_{e1} = \varepsilon_1 u_1$ and $w_{e2} = \varepsilon_2 u_2$ where ε_1 and ε_2 are entrainment coefficients that account for the effects of dispersive mixing. Theoretically speaking, there is no reason that ε_1 and ε_2 have to be different. Therefore, we assume $\varepsilon_1 = \varepsilon_2 = \varepsilon$ so as to reduce the number of free parameters in our problem. (The preliminary accuracy of this assumption can be assessed in the context of the agreement between theory and numerical simulation to be presented later. A more detailed assessment of the relative magnitudes of ε_1 and ε_2 requires a dedicated study and so is left for future work.) On the other hand, and motivated by analog studies of turbulent free gravity currents (Ellison & Turner, 1959; Reeuwijk *et al.*, 2019), we allow the possibility that ε varies with the inclination angle of the bottom boundary, θ. Such a

dependence will be explored below.

Pressure in the bulk and dispersed phases is defined as

$$p_1(x,z,t) = \big[\Delta\overline{\rho}_2 g h_2 + \big(\Delta\rho_1 - \Delta\overline{\rho}_2\big) g h_1 - \rho_s g z\big]\cos\theta + \rho_0\, g\, x \sin\theta + P_0 \quad 0 \le z \le h_1\,, \tag{2.7}$$

$$p_2(x,z,t) = \big[\Delta\overline{\rho}_2 g h_2 - \overline{\rho}_2 g z\big]\cos\theta + \rho_0\, g\, x \sin\theta + P_0 \qquad h_1 \le z \le h_2\,, \tag{2.8}$$

in which P_0 is a reference pressure evaluated at $x = z = 0$ outside of the gravity current, ρ_s is the source (or bulk) fluid density and $\bar{\rho}_2$ is the z-averaged density in the dispersed phase. Moreover, $\Delta\rho_1 = \rho_0 \beta c_s$ is the density difference between the bulk and ambient phases and $\Delta\overline{\rho}_2 = \rho_0 \beta\, \overline{c}_2$ is the corresponding density difference for the dispersed phase, averaged over z. In deriving the previous expressions for $\Delta\rho_1$ and $\Delta\bar{\rho}_2$, reference is made to a linear equation of state of the form $\rho = \rho_0(1 + \beta c)$ in which ρ_0 is a reference density and β is the solute contraction coefficient. There is, in fact, a more subtle assumption associated with the derivation of (2.8) namely that vertical variation of ρ_2 small enough such that

$$\frac{1}{h_2 - z}\int_z^{h_2} \rho_2\, \mathrm{d}z \simeq \frac{1}{h_2 - h_1}\int_{h_1}^{h_2} \rho_2\, \mathrm{d}z \equiv \overline{\rho}_2\,. \tag{2.9}$$

Stated differently, the above assumption suggests a dispersed phase hydrostatic balance of the form

$$\frac{\partial p_2}{\partial z} = -\overline{\rho}_2\, g \tag{2.10}$$

rather than

$$\frac{\partial p_2}{\partial z} = -\rho_2\, g\,. \tag{2.11}$$

Our assumption that (2.10) and (2.11) are approximately equal is, of course, consistent with the principal of ignoring the vertical variation of concentration and of velocity in the dispersed phase.

By combining (2.7) and (2.8) with Darcy's law, i.e.

$$\boldsymbol{V} = -\frac{k}{\mu}(\nabla p - \rho \boldsymbol{g})\,, \tag{2.12}$$

where $\boldsymbol{V}$ is the Darcy flux, μ is the dynamic viscosity and k is the (assumed constant) medium permeability, the calculation steps of Appendix A.1 suggest that

$$u_1(x,t) = -\frac{kg\beta}{\nu}\Big[\frac{\partial b_2}{\partial x}\cos\theta + c_s\Big(\frac{\partial h_1}{\partial x}\cos\theta - \sin\theta\Big)\Big]\,, \tag{2.13}$$

$$u_2(x,t) = -\frac{kg\beta}{\nu}\Big[\frac{\partial\,(\bar{c}_2 h_2)}{\partial x}\cos\theta - \bar{c}_2\sin\theta\Big] \equiv -\frac{kg\beta}{\nu}\Big[\frac{\partial}{\partial x}\Big(\frac{b_2 h_2}{h_2 - h_1}\Big)\cos\theta - \bar{c}_2\sin\theta\Big]\,. \tag{2.14}$$

Here, $\nu = \mu/\rho_0$ is the kinematic viscosity.

If we assume drainage to be hydrostatically-driven through a fissure having permeability k_f, width ξ and depth l, application of Darcy's law (2.12) similar to Neufeld *et al.* (2009) yields the following expression for the drainage velocity:

$$w_d(x,t) = \frac{k_f g\beta}{\nu}\Big(\frac{c_s h_1 + b_2}{l} + c_s\Big)\cos\theta \tag{2.15}$$

(see Appendix A.2). Upon substituting (2.13-2.15) and the expressions for the entrainment velocities w_{e1} and w_{e2} into (2.2), (2.4) and (2.6), the following modified governing equations result:

$$\phi\frac{\partial h_1}{\partial t} + \frac{kg\beta}{\nu}\frac{\partial(h_1 U)}{\partial x} = -\varepsilon\frac{kg\beta}{\nu}U - \frac{k_f g\beta}{\nu}\Big(\frac{c_s h_1 + b_2}{l} + c_s\Big)\cos\theta \times F(x, x_f, \xi)\,, \tag{2.16}$$

$$\begin{aligned}\phi\frac{\partial h_2}{\partial t} - \frac{kg\beta}{\nu}\frac{\partial}{\partial x}\Big[(h_2 - h_1)\Big(\frac{\partial\Psi}{\partial x} - C\Big) - h_1 U\Big] = \\ -\varepsilon\frac{kg\beta}{\nu}\Big(\frac{\partial\Psi}{\partial x} - C\Big) - \frac{k_f g\beta}{\nu}\Big(\frac{c_s h_1 + b_2}{l} + c_s\Big)\cos\theta \times F(x, x_f, \xi)\,,\end{aligned} \tag{2.17}$$

$$\phi\frac{\partial b_2}{\partial t} - \frac{kg\beta}{\nu}\frac{\partial}{\partial x}\Big[b_2\Big(\frac{\partial\Psi}{\partial x} - C\Big)\Big] = \varepsilon\frac{kg\beta c_s}{\nu}U\,. \tag{2.18}$$

In the above equations, and for the sake of notational economy, we have introduced the following symbols:

$$U = -\Big(\frac{\partial b_2}{\partial x} + c_s\frac{\partial h_1}{\partial x}\Big)\cos\theta + c_s\sin\theta\,, \tag{2.19}$$

$$\Psi = \frac{b_2 h_2}{h_2 - h_1}\cos\theta\,, \tag{2.20}$$

$$C = \frac{b_2}{h_2 - h_1}\sin\theta\,. \tag{2.21}$$

The variables U, Ψ and C are introduced only to simplify the notation; we do not regard these variables as having a noteworthy physical significance. Equations (2.16-2.18) contain three unknowns, namely h_1, h_2 and b_2. The equations are solved with the boundary conditions listed below.

2.3.2 Boundary conditions

Boundary conditions for (2.16-2.18) are

$$-\frac{kg\beta}{\nu}\Big[\Big(\frac{\partial b_2}{\partial x} + c_s\frac{\partial h_1}{\partial x}\Big)h_1\cos\theta - c_s h_1\sin\theta\Big]_0 = q_s\,, \qquad h_1|_{x_{N_b}} = 0\,, \tag{2.22a,b}$$

$$h_2|_0 = h_1|_0\,, \qquad h_2|_{x_{N_d}} = 0\,, \tag{2.22c,d}$$

$$b_2|_0 = 0\,, \qquad b_2|_{x_{N_d}} = 0\,. \tag{2.22e,f}$$

Here, x_{N_b} and x_{N_d} are the bulk and dispersed nose positions, respectively as indicated in figure 2.1. Note that (2.22a) represents the influx boundary condition, $q_s = \big(u_1 h_1\big)_0$, at the source. It is not required to take $b_1|_{x_{N_b}} = 0$ because the source concentration is fixed (and finite) so $b_1|_{x_{N_b}} = 0$ is automatically-satisfied by (2.22b). From boundary condition (2.22c), we assume that the thickness, $h_2 - h_1$, of the dispersed phase is zero at $x = 0$; we investigate the validity of this assumption below. Finally, the expressions of global volume balance in the bulk phase and the expression of global buoyancy/solute balance for the combined bulk and dispersed phases can be written as

$$q_s t = \phi\int_0^{x_{N_b}} h_1\,\mathrm{d}x - \xi\int_0^t w_d\,\mathrm{d}t - \int_0^t\int_0^{x_{N_b}} w_{e1}\,\mathrm{d}x\,\mathrm{d}t\,, \tag{2.23a}$$

$$q_s c_s t = \phi\, c_s\int_0^{x_{N_b}} h_1\,\mathrm{d}x - \xi c_s\int_0^t w_d\,\mathrm{d}t + \phi\int_0^{x_{N_d}}(h_2 - h_1)\bar{c}_2\,\mathrm{d}x\,. \tag{2.23b}$$

The first term on the right-hand side of (2.23a) represents the volume of the bulk phase fluid, the second term represents the volume of bulk fluid drained through the fissure and the third term

represents the volume of fluid lost by the bulk phase to the dispersed phase. The first term on right-hand side of (2.23b) represents the buoyancy in the bulk phase, the second term represents the buoyancy lost by the bulk phase due to fissure drainage and the third term represents buoyancy in the dispersed phase where we have assumed implicitly that $h_1 = 0$ for $x_{N_b} < x < x_{N_d}$.

2.3.3 Non-dimensional governing equations

Consistent with Neufeld *et al.* (2009), we respectively define the characteristic downdip length scale, the characteristic across-dip length scale and the characteristic timescale as

$$X = x_f\,, \qquad H = \Big(\frac{x_f\, q_s \phi\nu}{k g_s'}\Big)^{1/2}, \qquad \text{and} \qquad T = \Big(\frac{x_f^3 \phi\nu}{k g_s' q_s}\Big)^{1/2}, \tag{2.24a-c}$$

where $g_s' = g_1' = g\beta c_s$ is the source reduced gravity and x_f denotes the fissure position – see figure 2.1. Thus do we define the following non-dimensional (starred) variables:

$$c_2^* = \frac{\overline{c}_2}{c_s}\,, \quad x^* = \frac{x}{X}\,, \quad \xi^* = \frac{\xi}{X}\,, \quad h_1^* = \frac{h_1}{H}\,, \quad h_2^* = \frac{h_2}{H}\,, \quad l^* = \frac{l}{H}\,, \quad t^* = \frac{t}{T}\,. \tag{2.25a-g}$$

Neufeld *et al.* (2009) defined a parameter to characterise the drainage through an isolated fissure of width ξ. With reference to this parameter and their equation (2.12), we define, for the flow depicted in figure 2.1, an upstream flow parameter Γ and a fissure permeability ratio K as

$$\Gamma = \frac{\frac{x_f\, h_0}{q_s}}{\frac{x_f}{u_b}}\,\frac{x_f}{h_0} = \frac{u_b x_f}{q_s} \equiv \frac{k g_s' x_f}{\phi\nu q_s}\,, \tag{2.26a}$$

$$K = \frac{k_f}{k}\,, \tag{2.26b}$$

respectively. In (2.26a), h_0 is the height of the gravity current at the source and $u_b = \frac{k g_s'}{\phi\nu}$ is the buoyancy velocity associated with a source concentration c_s. There are a variety of different ways to interpret the upstream flow parameter Γ. Firstly, Γ can be thought of as the analog of the Richardson number because its definition includes the ratio of the time, $t_s = \frac{x_f\, h_0}{q_s}$, for fluid to flow from the source to the fissure based on the source volume flux, to the time, $t_f = \frac{x_f}{u_b}$, for fluid to

flow from the source to the fissure based on the source reduced gravity. Keeping with a ratio of timescales, Γ can also be interpreted as a ratio including t_f and $t_b = \frac{q_s}{u_b^2}$, which is a characteristic time of the flow. Finally, $\Gamma\,(= x_f/(\frac{q_s}{u_b}))$ can be thought of as the ratio of the fissure distance, x_f, to the flow thickness, $\frac{q_s}{u_b}$. As the above definitions of Γ make clear, the larger the value of Γ, the more the gravity current flow is influenced by its density contrast with the ambient. The fissure permeability ratio $K(< 1)$ corresponds to the ratio of the flow resistance through the porous medium to the drainage resistance through the fissure. Therefore, the larger K, the greater the volume of fluid that can drain through the fissure for a fixed depth of gravity current.

Applying the above definitions, (2.16-2.18) may be rewritten in non-dimensional form as

$$\frac{\partial h_1^*}{\partial t^*} + \frac{\partial (h_1^* U^*)}{\partial x^*} = -\varepsilon\,\Gamma^{1/2}\,U^* - K\,\Gamma\Big(\frac{h_1^* + b_2^*}{l^*} + 1\Big)\cos\theta \times F(x^*, 1, \xi^*)\,, \tag{2.27}$$

$$\frac{\partial h_2^*}{\partial t^*} - \frac{\partial}{\partial x^*}\Big[\Big(h_2^* - h_1^*\Big)\Big(\frac{\partial \Psi^*}{\partial x^*} - C^*\Big) - h_1^* U^*\Big] = - \varepsilon\,\Gamma^{1/2}\Big(\frac{\partial \Psi^*}{\partial x^*} - C^*\Big) - K\,\Gamma\Big(\frac{h_1^* + b_2^*}{l^*} + 1\Big)\cos\theta \times F(x^*, 1, \xi^*)\,, \tag{2.28}$$

$$\frac{\partial b_2^*}{\partial t^*} - \frac{\partial}{\partial x^*}\Big[b_2^*\Big(\frac{\partial \Psi^*}{\partial x^*} - C^*\Big)\Big] = \varepsilon\,\Gamma^{1/2}\,U^*\,. \tag{2.29}$$

Here,

$$b_2^* = c_2^*\left(h_2^* - h_1^*\right), \tag{2.30}$$

$$U^* = -\Big(\frac{\partial b_2^*}{\partial x^*} + \frac{\partial h_1^*}{\partial x^*}\Big)\cos\theta + \Gamma^{1/2}\sin\theta\,, \tag{2.31}$$

$$\Psi^* = \frac{b_2^*\,h_2^*}{h_2^* - h_1^*}\cos\theta\,, \tag{2.32}$$

$$C^* = \Gamma^{1/2}\,\frac{b_2^*}{h_2^* - h_1^*}\sin\theta\,. \tag{2.33}$$

Also, the boundary conditions (2.22) now read

$$\phi\,\Big[\Big(\frac{\partial b_2^*}{\partial x^*} + \frac{\partial h_1^*}{\partial x^*}\Big)h_1^*\cos\theta - \Gamma^{1/2} h_1^* \sin\theta\Big]_0 = -1\,, \qquad h_1^*|_{x_{N_b}^*} = 0\,, \tag{2.34a,b}$$

$$h_2^*|_0 = h_1^*|_0\,, \qquad h_2^*|_{x^*_{N_d}} = 0\,, \tag{2.34c,d}$$

$$b_2^*|_0 = 0\,, \qquad b_2^*|_{x^*_{N_d}} = 0\,. \tag{2.34e,f}$$

Assuming a fixed value for the medium porosity, ϕ, there are five dynamically-significant dimensionless groups in (2.27-2.34), namely Γ, K, ξ^*, l^*, and θ. These dimensionless groups characterize the fluid, medium and fissure properties.

The governing equations are solved using an explicit finite difference algorithm where spatial derivatives are discretized using backward finite differences because the source is situated on the upstream side (see Appendix A.3 for more details). Sample results are shown in figure 2.2 for $\theta = 0°$ and for $\theta = 5°$. Because bulk fluid drains through the fissure but not so dispersed fluid, significant separation of the bulk and dispersed interfaces occurs only downstream of $x^* = 1$. Figure 2.2 illustrates a sharp change in the leading edge profile of the dispersed phase, especially at late times. The slope of this leading edge is set by a balance between the advection and dispersion. When, as is the case here, advection dominates, the nose of the dispersed phase is expected to change abruptly (though not discontinuously) as $x^* \to x^*_{N_d}$.

Accordingly, we focus on the dispersed phase and its fraction, relative to the gravity current as a whole, of buoyancy (per unit box width) and of area (volume per unit box width). In symbols, these quantities are denoted as B and A, respectively. In performing the requisite calculations, we first evaluate the area enclosed by the bulk interface (the thick lines in figure 2.2) and by the dispersed interface (the thin lines in figure 2.2). Areas are calculated from

$$A^*_{\rm bulk} = \int_0^{x^*_{N_b}} h_1^*\,{\rm d}x^* \qquad \text{and} \qquad A^*_{\rm disp} = \int_0^{x^*_{N_d}} (h_2^* - h_1^*)\,{\rm d}x^*\,. \tag{2.35a,b}$$

The dispersed area fraction $\tilde{A}^*_{\rm disp}$ is found from

$$\tilde{A}^*_{\rm disp} \;=\; \frac{A^*_{\rm disp}}{A^*_{\rm bulk} + A^*_{\rm disp}}\,. \tag{2.36}$$

Buoyancies in the bulk and dispersed phases are respectively determined from

$$B^*_{\rm bulk} = \int_0^{x^*_{N_b}} h^*_1 \, {\rm d}x^* = A^*_{\rm bulk} \qquad \text{and} \qquad B^*_{\rm disp} = \int_0^{x^*_{N_d}} b^*_2 \, {\rm d}x^* \,, \tag{2.37a,b}$$

The quantities $B^*_{\rm bulk}$ and $A^*_{\rm bulk}$ are equal because concentrations are scaled by c_s. Similar to (2.36), the dispersed buoyancy fraction is given by

$$\tilde{B}^*_{\rm disp} \;=\; \frac{B^*_{\rm disp}}{B^*_{\rm bulk} + B^*_{\rm disp}} \,. \tag{2.38}$$

Figures 2.3 a,b show time-series of $\tilde{A}^*_{\rm disp}$ and $\tilde{B}^*_{\rm disp}$ for $\theta = 0^\circ$ and $\theta = 5^\circ$. As these figures make clear, dispersion increases when the bottom boundary is inclined and more solute will then reside in the dispersed phase. This phenomenon can be understood with reference to the significantly larger characteristic value for u_1 measured in the case of the sloping boundary, i.e. at $t^* = 60$, the magnitude of u_1 when $\theta = 5^\circ$ is approximately 30% larger than that for $\theta = 0^\circ$. A parametric study that more carefully documents the impact of the non-dimensional parameters θ, Γ, K, ξ^*, and l^* on the evolution of the gravity current is included in section 2.5 below.

2.4 Numerical investigation

COMSOL simulations were performed so as to illustrate the effects of dispersive mixing in gravity currents within porous media and to assess our mathematical model in various scenarios. COMSOL utilizes the finite element method to discretize the governing equations (given below).

Our COMSOL model is validated in two complementary ways. First, we model the flow of a porous media gravity current along an impermeable boundary (in which dispersion is comparatively small) and thereby demonstrate excellent agreement with the sharp interface solution of Huppert & Woods (1995). Second, we confirm that our COMSOL model correctly predicts the degree of dispersion in a scenario where fluid density differences are absent, i.e. the scalar is passive rather than active. More specifically, we model the mixing of two miscible fluids in a long capillary

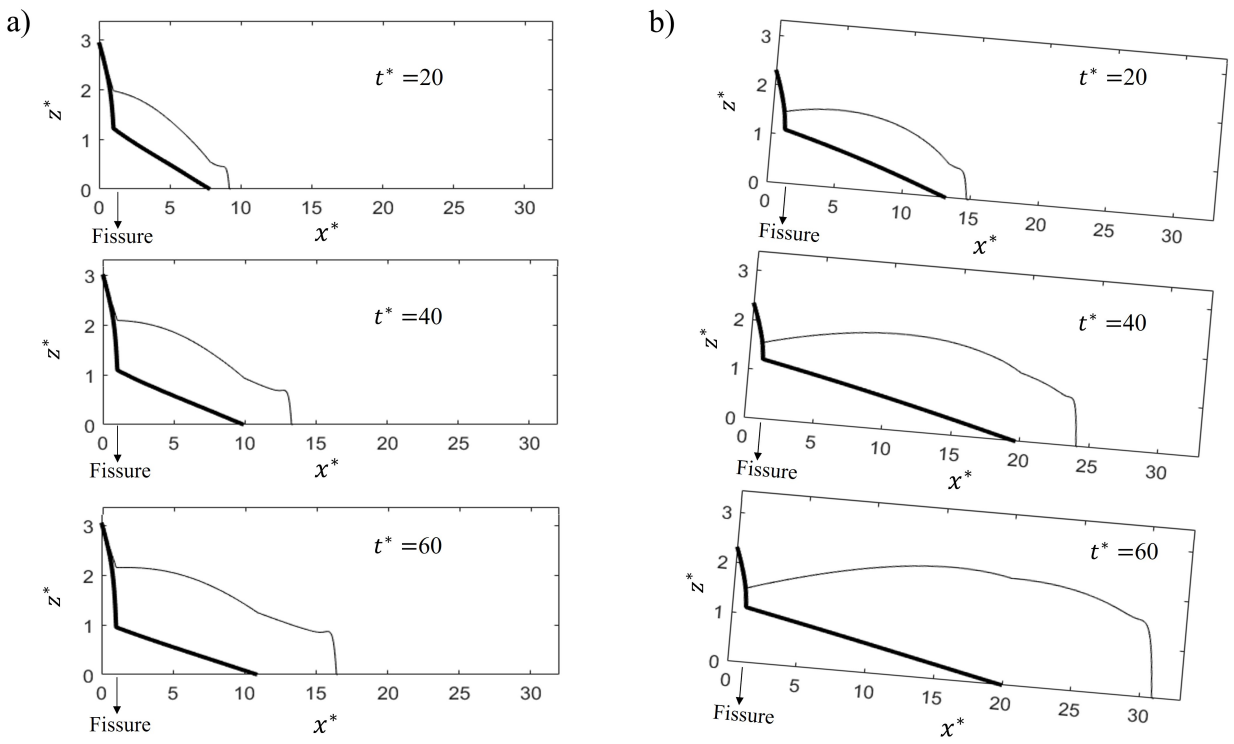

Figure 2.2: Theoretical predictions showing, for different times, gravity current profiles for (a) $\theta = 0°$ and (b) $\theta = 5°$. The thick line represents the bulk interface and the thin line represents the dispersed interface. The location of the fissure is as indicated. Here, $\Gamma = 35$, $K = 0.5$, $l^* = 0.79$ and $\xi^* = 0.04$. As we will justify in section 2.4.5, we consider $\varepsilon = 0.0125$ when $\theta = 0°$ and $\varepsilon = 0.0086$ when $\theta = 5°$.

tube. As considered by Bear (1972), section 10.6, the up-and downstream fluids have initial solute concentrations of 0 and c_s, respectively, but mix as a result of dispersion. Here again, we observe excellent agreement between the theoretical solution and the corresponding COMSOL-based numerical result – see Appendix C.1.1 for more details.

2.4.1 Numerical set-up

Simulations are conducted in a 2-D rectangular box 400 cm long × 25 cm deep filled with a porous medium saturated with water having a density $\rho_0 = 0.998\,\mathrm{g\,cm^{-3}}$. The medium porosity is $\phi = 0.38$ based on the assumption of a random close packing of beads (Happel & Brenner (1991)). The permeability is $2.18 \times 10^{-4}\,\mathrm{cm^2}$ and by inverting Rumpf & Gupte's relation (Rumpf & Gupte,

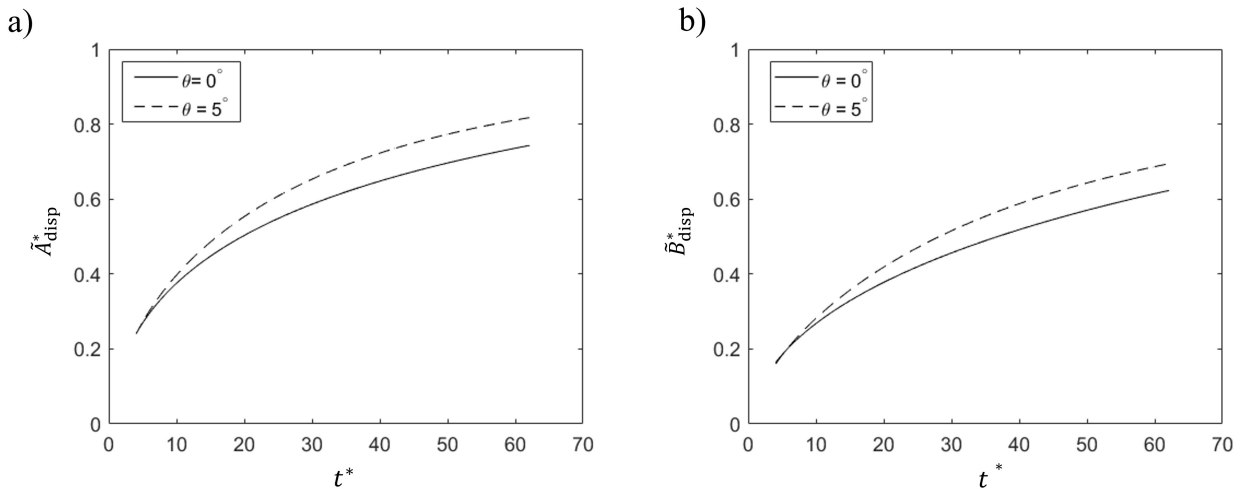

Figure 2.3: Percentage of the gravity current (a) volume and (b) buoyancy that remains in the dispersed phase for $\theta = 0^\circ$ with $\varepsilon = 0.0125$ and $\theta = 5^\circ$ with $\varepsilon = 0.0086$. Here, consistent with figure 2.2, $\Gamma = 35$, $K = 0.5$, $l^* = 0.79$ and $\xi^* = 0.04$.

1971)

$$k = \frac{1}{5.6} d_p^2 \, \phi^{5.5} \,, \tag{2.39}$$

we determine that the equivalent bead diameter measures $d_p = 5\,\text{mm}$, which is broadly consistent with the related experiments of Sahu & Flynn (2017) and Bharath *et al.* (2020) for which the Reynolds number is on the order of 0.3. The salt water of fixed concentration is discharged at a constant rate from a source located in the bottom-left corner of the numerical domain – see figure 2.4. The source has a vertical expanse of 1 cm; Broadly comparable to Neufeld *et al.* (2009) the fissure is situated at a distance of $x_f = 7.5\,\text{cm}$ from the source. At this location, deviation from a hydrostatic pressure gradient is small.

Two different COMSOL physics interfaces are used, i.e.

1. The Darcy's law (dl) interface is used to model fluid flow within the porous medium specifically

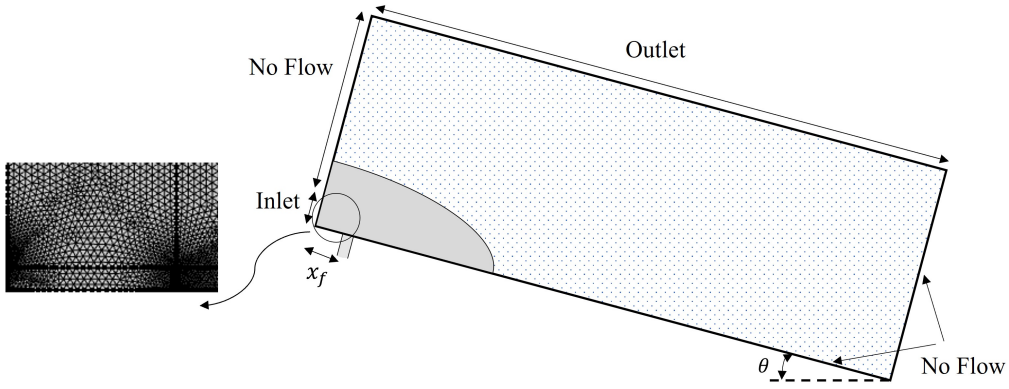

Figure 2.4: Schematic of the numerical set-up.

by solving the following mass and momentum equations:

$$\frac{\partial u}{\partial x} + \frac{\partial w}{\partial z} = 0\,, \tag{2.40a}$$

$$\frac{1}{\rho_0}\frac{\partial p}{\partial x} + \frac{\nu}{k}u = -\frac{\rho}{\rho_0}g\sin\theta\,, \tag{2.40b}$$

$$\frac{1}{\rho_0}\frac{\partial p}{\partial z} + \frac{\nu}{k}w = \frac{\rho}{\rho_0}g\cos\theta\,. \tag{2.40c}$$

2. Solute transport is modeled using the transport of diluted species in porous media (tds) interface where the underlying equation to be solved reads

$$\phi\frac{\partial c}{\partial t} + u\frac{\partial c}{\partial x} + w\frac{\partial c}{\partial z} = \phi\Big[\frac{\partial}{\partial x}\Big(D_{xx}\frac{\partial c}{\partial x} + D_{xz}\frac{\partial c}{\partial z}\Big) + \frac{\partial}{\partial z}\Big(D_{xz}\frac{\partial c}{\partial x} + D_{zz}\frac{\partial c}{\partial z}\Big)\Big]\,. \tag{2.41}$$

Here, c is concentration and D_{ij} is a dispersion coefficient. The dispersion tensor D_{ij} is defined as

$$D_{ij} = D_{\text{mol}} + a_{ijlm}\frac{V_l V_m}{|\boldsymbol{V}|}\,. \tag{2.42}$$

Here, D_{mol} is the coefficient of molecular diffusion, $V_{()}$ is a component of the velocity whose overall magnitude is given by $|\boldsymbol{V}|$ and a_{ijlm} is the geometrical dispersivity of the porous medium. Scheidegger (1961) showed that a_{ijlm} is a sparse matrix in which only terms $a_{1111} = a_{2222} = a_L$, $a_{1122} = a_{2211} = a_T$ and $a_{1212} = a_{2121} = a_{1221} = a_{2112} = \frac{1}{2}(a_L - a_T)$ are non-zero for two-dimensional

porous media flow. The dispersion coefficients for such a two-dimensional flow can therefore be defined as follows:

$$D_{xx} = D_{\text{mol}} + a_L \frac{u^2}{|\boldsymbol{V}|} + a_T \frac{w^2}{|\boldsymbol{V}|}\,, \tag{2.43a}$$

$$D_{zz} = D_{\text{mol}} + a_L \frac{w^2}{|\boldsymbol{V}|} + a_T \frac{u^2}{|\boldsymbol{V}|}\,, \tag{2.43b}$$

$$D_{xz} = D_{\text{mol}} + (a_L - a_T) \frac{|uw|}{|\boldsymbol{V}|}\,. \tag{2.43c}$$

The variables a_L and a_T are called the longitudinal dispersivity and the transverse dispersivity, respectively. The dispersivities do not assume universal values and are, instead, resolved by curve fitting relevant experimental data corresponding to various regions of the parameter space e.g. as defined by the Schmidt (Sc) and Péclet (Pe) numbers. Notwithstanding this complication, we can adapt (3) and (4) of Delgado (2007) to derive reasonable predictions for these two parameters for the Péclet numbers relevant to our flow. For mathematical convenience in practical applications and as suggested by Sahimi (2011), the power of Pe in (3) of Delgado (2007) is considered to be unity for $5 < \text{Pe} < 300$. Therefore, the longitudinal and transverse dispersivities in this region are

$$a_L = 0.5\, d_p\,, \tag{2.44a}$$

$$a_T = 0.025\, d_p\,, \tag{2.44b}$$

respectively. For $300 < \text{Pe} < 10^5$, the relevant equations are

$$a_L = (1.8 \pm 0.4)\, d_p\,, \tag{2.45a}$$

$$a_T = 0.025\, d_p\,. \tag{2.45b}$$

In this work, we take a_L to be $1.8\, d_p$ for $300 < \text{Pe} < 10^5$.

2.4.2 Initial conditions

Consistent with the theory of section 2.3, we assume the porous medium is saturated with quiescent fresh water at $t = 0$. The initial pressure distribution is therefore hydrostatic and the initial solute concentration is everywhere zero. The source concentration is related to the source density, ρ_s, via the equation of state, i.e.

$$c_s = \frac{\rho_s - \rho_0}{\rho_0 \beta} \,.$$

Here, β is considered constant so the effects of temperature and pressure are ignored. According to the study of Millero & Poisson (1981), β is 0.82 cm^3/g. After defining the source concentration for desired ρ_s, the linear equation of state $\rho = \rho_0(1 + \beta\, c)$ is used to relate the density to the concentration field c.

2.4.3 Meshing and solver

Equations (2.40) and (2.41) are discretized using an unstructured triangular mesh. As shown in figure 2.4, grid refinement is applied in the vicinity of the source and of the fissure because these are regions of significant velocity shear. Figure 2.5 shows, for $t^* = 40$, $\tilde{A}^*_{\text{disp}}$ for various grid sizes from coarse to fine. The dispersed phase area fraction is sufficiently close to its asymptotic value when the grid is comprised of 81715 $\simeq 10^{4.91}$ triangles; at and beyond this point, we deem the numerical results to be grid-independent.

To discretize the equations in space, cubic shape functions are chosen for (2.40), whereas quadratic shape functions are selected for (2.41). Note that due to stability concerns, the order of the shape function for the former equation must be higher than the that of the latter equation. For (2.41), a third-order implicit Backward Differentiation Formula (BDF) is applied such that

$$\phi\, \frac{11c^{n+1} - 18c^n + 9c^{n-1} - 2c^{n-2}}{6\Delta t} = \left[\phi \frac{\partial}{\partial x}\left(D_{xx}\frac{\partial c}{\partial x} + D_{xz}\frac{\partial c}{\partial z}\right) + \phi \frac{\partial}{\partial z}\left(D_{xz}\frac{\partial c}{\partial x} + D_{zz}\frac{\partial c}{\partial z}\right) - u\frac{\partial c}{\partial x} - w\frac{\partial c}{\partial z}\right]^{n+1} , \quad (2.46)$$

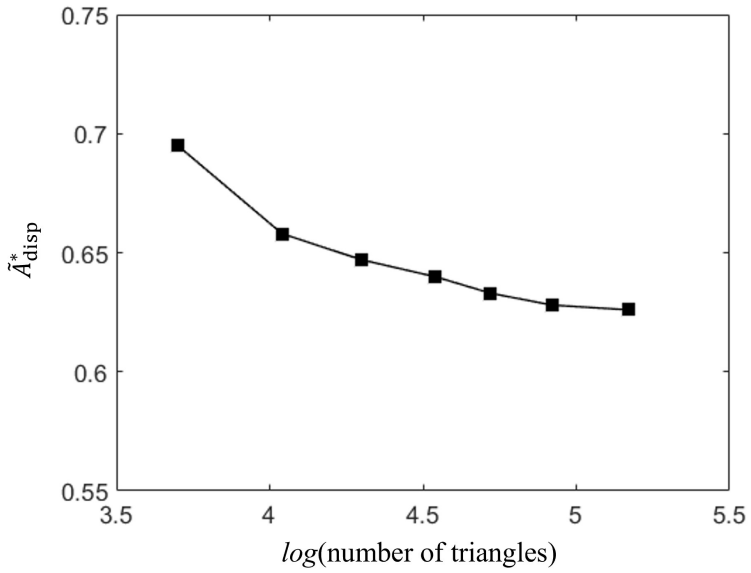

Figure 2.5: Numerically-determined estimates for the dispersed phase area fraction for different grid sizes. Here, consistent with figure 2.2, $\theta = 0°$, $\Gamma = 35$, $K = 0.5$, $l^* = 0.79$ and $\xi^* = 0.04$.

where n is the time increment. Increasing the order of shape functions or order of time discretization method does not lead to significant changes in the results, but it requires substantially more computational effort to solve.

We implement a two-step sequential method to solve (2.40) and (2.41) by using a two-step segregated solver within COMSOL. In the first step, (2.40a-c) are solved by considering the fluid density, ρ, as known. Then in the second step, velocities calculated in step one are applied to solve (2.41) for concentration. Thus the Darcy and species equations are solved in sequence at each time step until convergence is achieved. In this work, we consider a relative convergence tolerance of 0.001.

2.4.4 Qualitative observations (horizontal bottom boundary)

One of the key assumptions applied in the model of section 2.3.1 is that there persists a bulk gravity current within which the solute concentration is effectively the same as the source concentration, c_s. The numerical simulations afford us the opportunity to test the validity of this assumption in different regions of the parameter space. To this end, numerical simulations indicate that the bulk

phase concentration decreases downstream of the fissure and is less than c_s due to the dispersion that arises in conjunction with drainage. This discrepancy between the bulk phase concentration and the source concentration can, for sufficiently vigorous dispersive mixing, affect the accuracy of our theoretical model. It is necessary, therefore, to estimate the parametric regime where such vigorous dispersive mixing is/is not significant. The degree to which the bulk phase concentration deviates from c_s depends on the upstream flow parameter, Γ, the permeability ratio, K, and the non-dimensional fissure width, ξ^* – see figure 2.6. Although there is an additional dependence on the vertical extent, l^*, of the fissure, this dependence is weak and so is not considered in the figure. Concentrations in the regime diagram of figure 2.6 are measured at $x^* = 2$, $z^* = 0$ and at a time t^* when the dispersed nose position $x^*_{N_d} = 10$. Based on figure 2.6, we surmise that the theoretical model predicts the bulk interface with good accuracy for arbitrary Γ and K. On the other hand, our model does a comparatively poor job of predicting the location of the dispersed interface when $c^*(2,0) \equiv c(2,0)/c_s < 0.8$. Among other challenges when $c^*(2,0) < 0.8$ is the fact that the bulk phase terminates at the location of the fissure, i.e. any gravity current fluid appearing downstream of $x^* = 1$ has a density nontrivially less than ρ_s. This limitation notwithstanding, there remains a large parametric domain over which our theoretical model works well. Figure 2.6 suggests that as the upstream flow parameter Γ decreases, so too does the front speed. Less dispersive mixing is therefore observed and the solute concentration after the fissure decreases relatively slowly. As a result, there is a broader range of K over which our theoretical model generates predictions in reasonable agreement with the output of the numerical model. Of course, the degree of agreement between theory and numerics is related to the numerical value of the entrainment coefficient, ε, which appears e.g. in (2.16-2.18). We discuss the procedure for determining ε in the following subsection.

2.4.5 Determining the entertainment coefficient

Comparisons such as that depicted in figure 2.6 (and also figures 2.8 and 2.9 below) require that a value be specified for the entrainment coefficient, ε. This coefficient is found based on our numerical results. More specifically, we specify ε such that the separation distance, $x^*_{N_d} - x^*_{N_b}$, between the

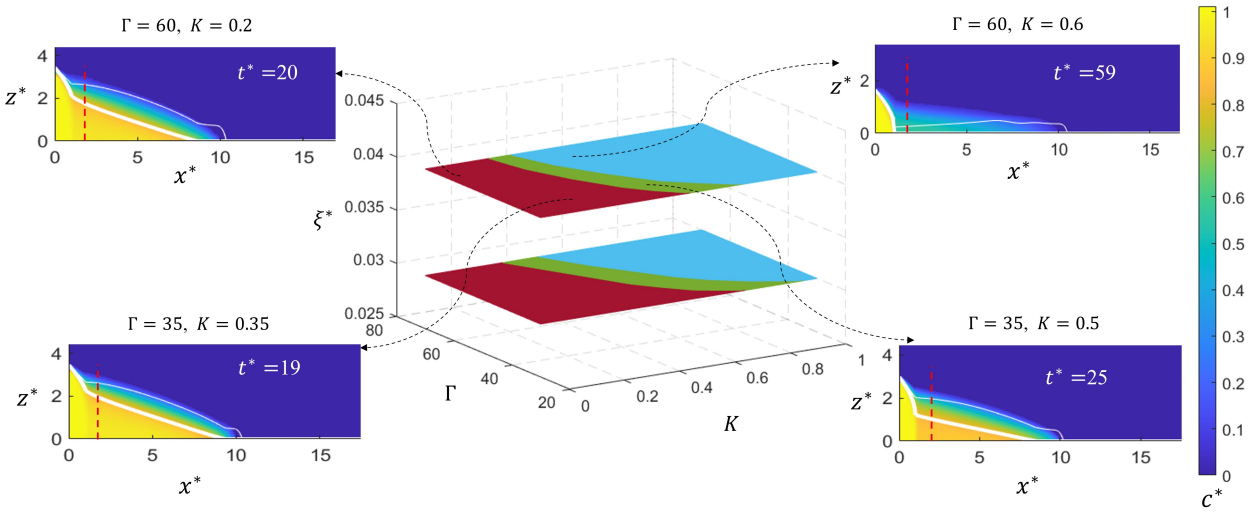

Figure 2.6: [Colour] Bulk phase concentration reduction beyond the fissure for $\theta = 0°$ and $l^* = 0.79$. The red area shows $c^* > 0.9$, the green area shows $0.8 < c^* < 0.9$ and the blue area shows $c^* < 0.8$. Boundaries are drawn based on an interpolation performed over a total of 14 simulations for each of the lower and upper surfaces. The inset images show a comparison between theory and numerical simulations for different combinations of Γ and K. The thick (thin) white line is the bulk (dispersed) interface as predicted by the theoretical model of section 2. Meanwhile colored contours show the output of the COMSOL numerical model. Red dashed lines indicate the location $x^* = 2$, where concentrations are evaluated in constructing the regime diagram.

dispersed and bulk nose positions matches as closely as possible the distance measured numerically. A mean temporal error is therefore defined as

$$\overline{E} = \int_{t_1^*}^{t_2^*} \frac{\left|\left(x^*_{N_d} - x^*_{N_b}\right)_{\text{theory}} - \left(x^*_{N_d} - x^*_{N_b}\right)_{\text{num}}\right|}{\left(x^*_{N_d} - x^*_{N_b}\right)_{\text{num}}} \, \mathrm{d}t^* \,. \tag{2.47}$$

Where $\left(x^*_{N_d} - x^*_{N_b}\right)_{\text{num}}$ is evaluated from the numerical model of section 2.4 and $\left(x^*_{N_d} - x^*_{N_b}\right)_{\text{theory}}$ is evaluated from the theoretical model of section 2.3 for various ε. The (unique) ε that minimizes $\overline{E}$ is referred to as the optimum entrainment coefficient. For simplicity, we assume that this optimum value does not depend on Γ and K; a justification for this assumption is given in the next paragraph. However, and motivated by the work of Ellison & Turner (1959), we allow the error-minimizing value of ε to vary with the inclination angle, θ, of the bottom boundary. Results associated with (2.47) and the minimization of $\overline{E}$ are displayed in figure 2.7. They suggest that the optimum value of ε experiences a nontrivial decrease as the slope angle is increased and the gravity current

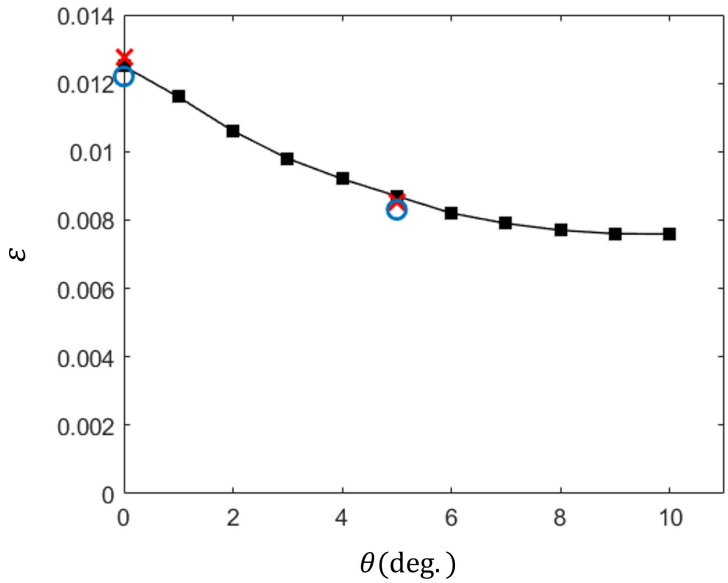

Figure 2.7: [Colour] Error-minimizing value of ε vs. θ. Here we consider $\Gamma = 45$, $K = 0.3$, $l^* = 0.79$ and $\xi^* = 0.04$. Blue circles consider $\Gamma = 45$, $K = 0.2$ and red crosses consider $\Gamma = 30$, $K = 0.3$ Also, and with reference to (2.47), $t_1^* = 20$ and $t_2^* = 70$.

propagates more rapidly downdip.

Also included in 2.7 are data corresponding to different values of Γ and K. The blue circles indicate the same value of Γ but a different value of K. The red crosses indicate the same value of K but a different value of Γ. In all cases, we see but a minor deviation from the quantitative data indicated by the black line. In principle, larger changes of K can be imagined, however, these would be inconsistent with figure 2.6, i.e. we limit ourselves to changes of K or Γ that keep us strictly within the red or green sections of the regime diagram.

2.5 Results and discussion

Within the region of model validity defined in subsection 2.4.4, theoretical results are compared in figure 2.8 against COMSOL numerical output. Also included in figure 2.8 is a sharp interface solution that is obtained by setting $\varepsilon = 0$ in (2.16) and (2.17). The sharp interface model over-predicts the nose position while under-predicting the height of the gravity current especially when the bottom boundary is inclined. A comparison of inclined vs. horizontal gravity currents reveals

that the height of the dispersed interface has a monotone variation with x^* when $\theta = 0°$ but a non-monotone variation with x^* when $\theta > 0°$. The non-monotone variation in question becomes more pronounced as time increases.

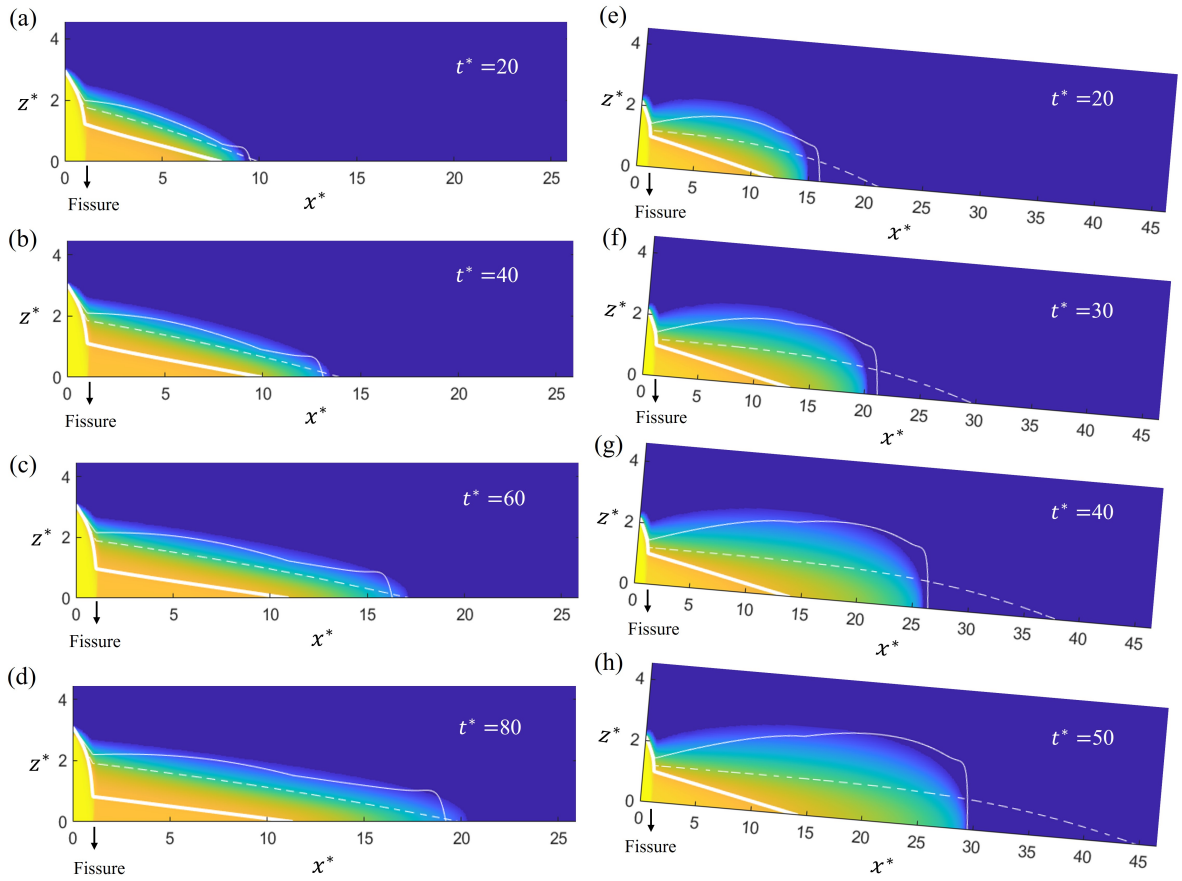

Figure 2.8: [Colour] Gravity current profiles as predicted theoretically and numerically. Line types are as follows: thick solid line – bulk interface; thin solid line – dispersed interface; dashed line – sharp interface solution obtained by setting $\varepsilon = 0$ in (2.16) and (2.17). Numerical output is indicated by the colour contours. (a-d) $\theta = 0°$, $\Gamma = 35$, $K = 0.5$, $\xi^* = 0.04$, and $l^* = 0.79$. (e-h) $\theta = 5°$, $\Gamma = 70$, $K = 0.3$, $\xi^* = 0.04$, and $l^* = 1.11$. The variation of parameter values between the left- and right-hand side panels is deliberate and illustrates model predictions over a broad range of the parameter space. Note that the scale of the horizontal axis in the left- and right-hand side images is different.

To quantify dispersion effects in gravity currents, we examine the time variation of $\tilde{A}^*_{\text{disp}}$ from (2.36) and $\tilde{B}^*_{\text{disp}}$ from (2.38) – see figures 2.9 (c,d,e). Each panel includes both theoretical and numerical data and considers a different value for K. Whether K is comparatively large (0.4) or

small (0.2), the same general trend appears: theory underpredicts the area and buoyancy fraction at early times, however, for sufficiently large t^*, good agreement is achieved. The early time discrepancy likely appears because the theoretical model assumes a long and thin gravity current. Although the gravity current evolves into a shape that is long and thin for large t^*, such a large aspect ratio does not apply initially. Furthermore, and for mathematical convenience, our theory is predicated on the assumption that $h_2(x = 0) = h_1(x = 0)$ however a careful inspection of our numerical results (not shown) indicates some nontrivial initial height of the dispersed phase, at least for not small times. From a theoretical standpoint, we lack precise insights into the height of the dispersed phase at $x = 0$. While it is possible to determine the value of $h_2(x = 0) - h_1(x = 0)$ through experimental or numerical simulations, we find that this value is a function of time. Therefore we jeopardize the local accuracy in the neighborhood of $x = 0$ for convenience by assuming no dispersed fluid near the source. Fortunately, the consequence of ignoring dispersed fluid in the neighborhood of the source becomes smaller as time progresses and the cumulative volume occupied by the (elongating) gravity current grows.

Whereas figures 2.9 (c,d,e) assume the same value for Γ, i.e. $\Gamma = 45$, the influence of the upstream flow parameter is explored in figures 2.9 (a,b) where Γ appears as the x-axis variable. The different curves of figure 2.9 (a,b) correspond to $K = 0.2, 0.3$ and 0.4 such that, with $\Gamma = 45$, the red and green regions of figure 2.6 are spanned appropriately. Curves are drawn at $t^* = 40$ by which time the gravity current is indeed long and thin, i.e. the comparison is not unduly influenced by effects related to the early time evolution of the flow. The area and buoyancy fractions increase with Γ and also with K. When the upstream flow parameter is large, there is more dispersive mixing because of larger velocities in the gravity current so the fraction of buoyancy and area associated with the dispersed phase increases. By increasing K, draining of bulk fluid is more robust causing the gravity current to elongate more slowly. Although this has a secondary effect on the dispersed phase (which is, after all, fed by the bulk phase), the overall impact of increasing K is to likewise increase the area and buoyancy fractions occupied by the dispersed phase in comparison to the bulk phase. Correspondingly, one might expect that, as K increases, so too does the separation distance between the bulk and dispersed nose positions. Figures 2.9 (f,g,h) both confirm this hypothesis and indicate

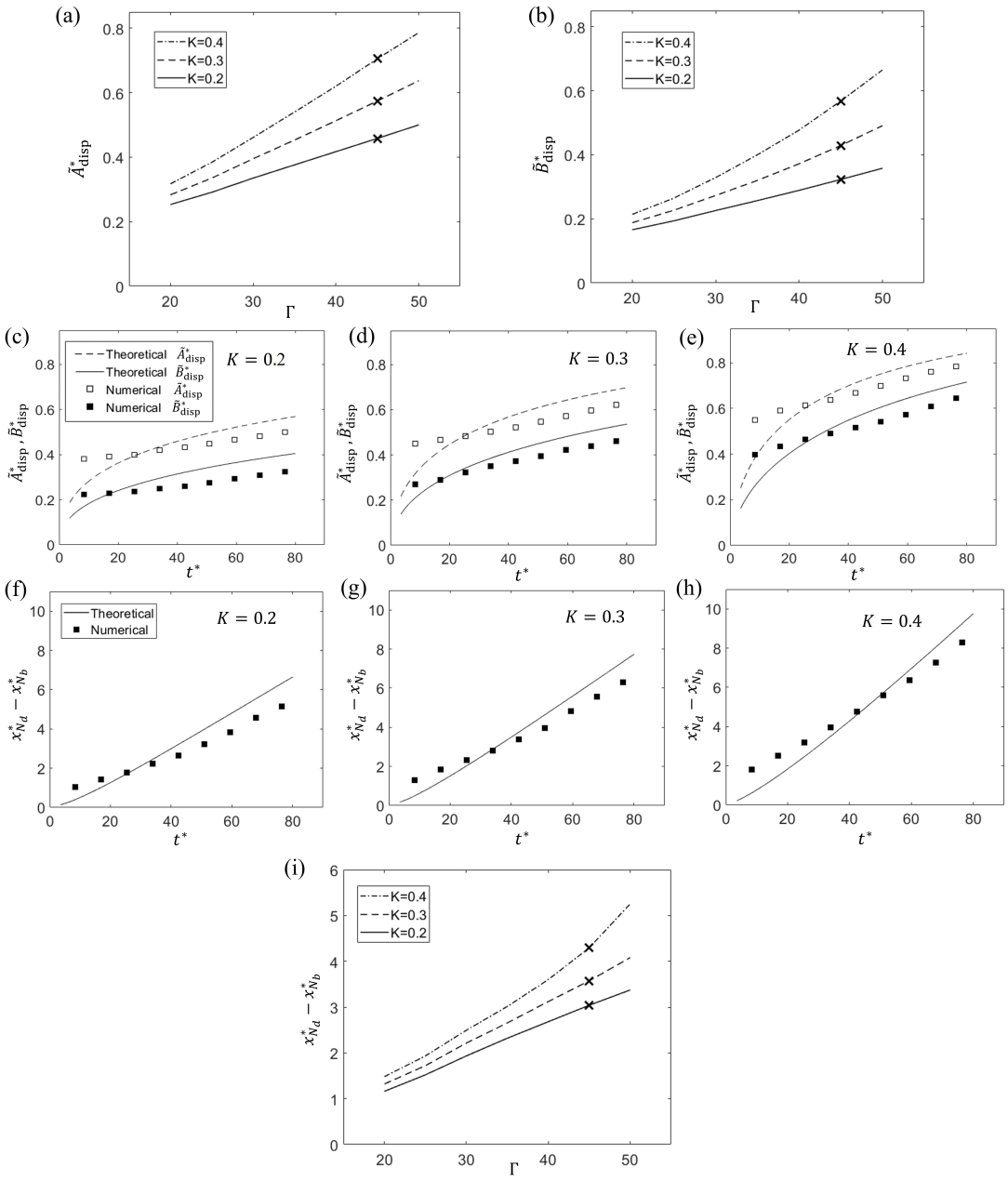

Figure 2.9: (a) Area fraction (equation 2.36) and (b) buoyancy fraction (equation 2.38) as a function of the upstream flow parameter (equation 2.26 a) for three different values of the fissure parameter (equation 2.26 b). Here, we consider a horizontal bottom boundary such that $\theta = 0°$ and $t^* = 40$. Crosses indicate the solutions for $\Gamma = 45$, for which corresponding time series data are given in panels (c), (d) and (e) for $K = 0.2$, 0.3 and 0.4, respectively. These same three K values are considered in the time series of panels (f), (g) and (h), which consider, again for $\Gamma = 45$ and $\theta = 0°$, the difference of nose position between the bulk and the dispersed gravity currents. This nose position difference is shown as a function of Γ in panel (i) where we again consider $t^* = 40$.

that the theory matches well with the analog numerical result. Whereas figures 2.9 (f,g,h) assume the same value for Γ, i.e. $\Gamma = 45$, the influence of the upstream flow parameter is explored in figure 2.9 (i) where Γ again appears along the abscissa. The different curves of figure 2.9 (i) correspond to $K = 0.2, 0.3$ and 0.4 and are drawn at $t^* = 40$. Figure 2.9 (i) indicates that $x^*_{N_d} - x^*_{N_b}$ increases with both Γ and K.

Analogue results have been generated for $\theta = 5^\circ$ to quantify dispersion effects for the case of inclined gravity currents – see figure 2.10. Comparing this figure against figure 2.9 shows that, as expected, dispersion is more robust when $\theta > 0^\circ$. For instance, and when $t^* = 60$, figure 2.10 g suggests the nose separation for $\theta = 5^\circ$ is almost twice of that in figure 2.9 g for $\theta = 0^\circ$. This is because of the larger characteristic velocity in the inclined case, which leads to more entrainment to the dispersed phase either from the ambient or the bulk phase. This point notwithstanding, very similar trends are observed in figures 2.9 and 2.10, e.g. in both cases the separation between the bulk and dispersed noses increases with K (due to a stronger drainage) and also with Γ (due to a larger characteristic velocity). Moreover, theory and numerical simulation demonstrate satisfactory agreement with generally better overlap observed for larger t^*.

Further to the comparison between figures 2.9 and 2.10, the sensitivity of our model predictions to the slope of the bottom boundary is more thoroughly explored in figure 2.11. Figure 2.11 a shows, for $t^* = 45$, the difference of nose positions for the bulk vs. dispersed phases. Meanwhile figure 2.11 b shows the corresponding area and buoyancy fractions for dispersed phase fluid, i.e. $\tilde{A}^*_{\text{disp}}$ and $\tilde{B}^*_{\text{disp}}$. Both panels of figure 2.11 include theoretical and numerical data and confirm the hypothesis that dispersion increases with θ.

Because fissure dimensions directly impact drainage, ξ^* and l^* also influence the degree of dispersion. Figure 2.12 confirms that increasing the fissure width, ξ^*, leads to more dispersion, whether measured in terms of $x^*_{N_d} - x^*_{N_b}$ or $\tilde{A}^*_{\text{disp}}$. On the other hand, bulk fluid drainage decreases by increasing the vertical extent, l^*, of the fissure. As a result, there is less dispersion as l^* is increased – see figure 2.13. Consistent with our previous results, figures 2.12 and 2.13 indicate that inclined gravity currents experience more dispersion than do horizontal gravity currents.

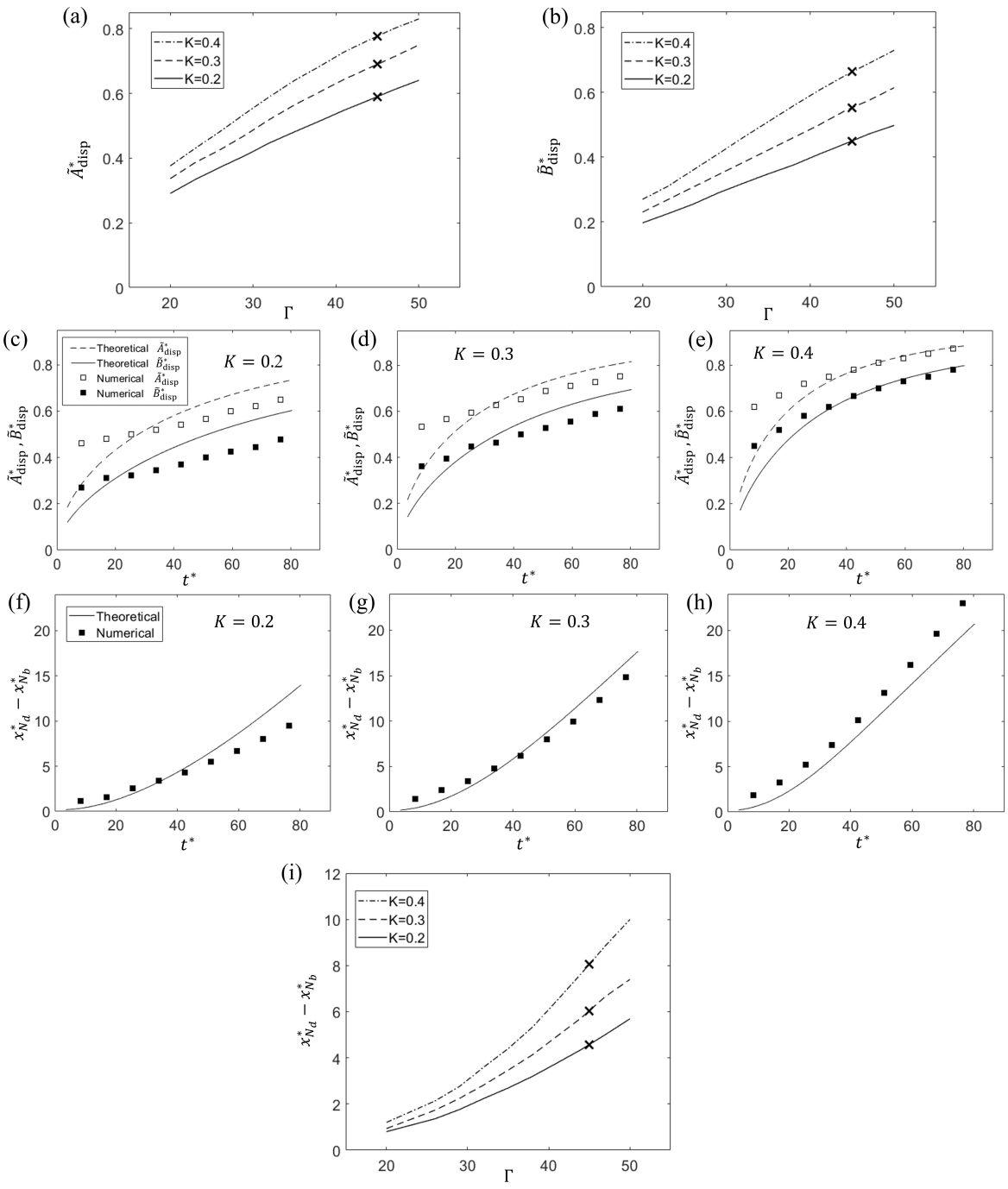

Figure 2.10: As in figure 2.9 but with an inclined boundary ($\theta = 5^\circ$).

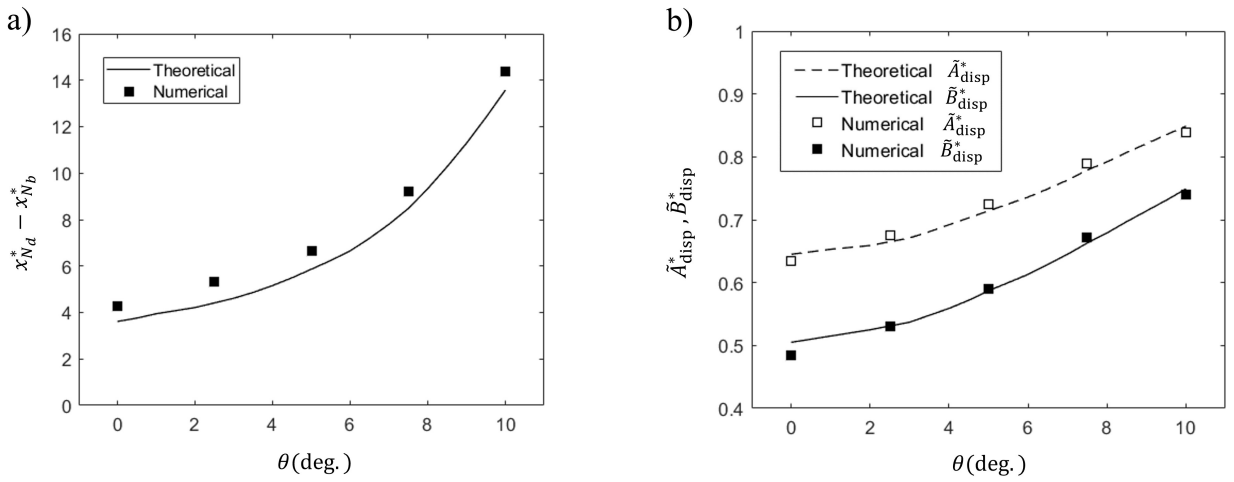

Figure 2.11: Difference of (a) nose positions and of (b) dispersed phase area and buoyancy fractions vs. θ. Here, $t^* = 45$, $\Gamma = 35$, $K = 0.5$, $l^* = 0.79$ and $\xi^* = 0.04$.

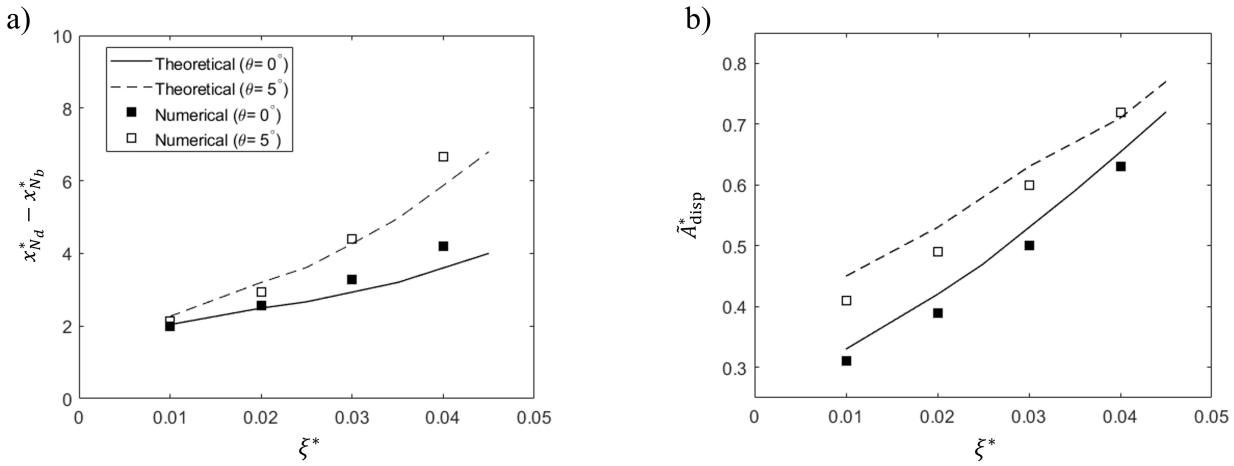

Figure 2.12: Difference of (a) nose position and (b) area fraction in the dispersed phase for $\theta = 0°$ with $\varepsilon = 0.0125$ and $\theta = 5°$ with $\varepsilon = 0.0086$ for various ξ^*. Here, $t^* = 45$, $\Gamma = 35$, $K = 0.5$, and $l^* = 0.79$.

2.6 Application to UHS

To illustrate the application of our results, we return to the example of UHS considered in section 2.2. More specifically, and for the idealized case of an unbounded reservoir, we wish to estimate the fraction of H_2 that will be lost to dispersion as a function of, say, the source volume flow rate. To this end, we consider a line, rather than a point, source such that q_s is expressed in units of standard

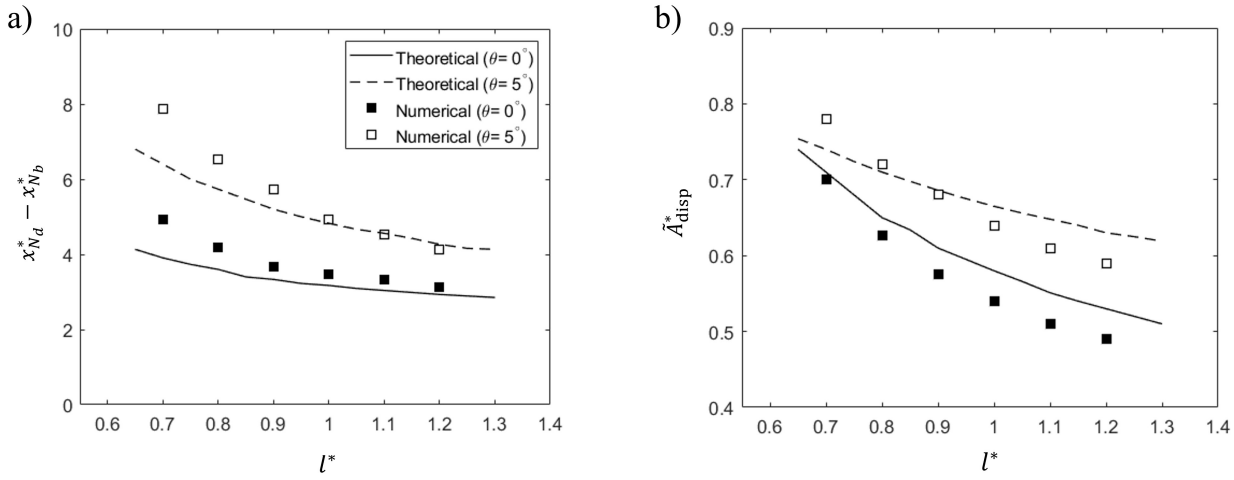

Figure 2.13: As in figure 2.12 but considering the influence of l^* for $\xi^* = 0.04$.

$\mathrm{m}^3/\mathrm{m}/\mathrm{day}$ or $\mathrm{S\,m}^2/\mathrm{day}$. Motivated by the numerical investigation of Feldmann *et al.* (2016), we further suppose that H_2 is injected into a sandstone layer, bounded above and below by clay layers, where the cushion gas consists of 80 mol% N_2 and 20 mol% CH_4. The reservoir pressure is 170 bar such that the density contrast between the H_2 and the cushion gas is approximated as $118\,\mathrm{kg}/\mathrm{m}^3$. The sandstone layer has a porosity of $\phi = 13.08\%$ and a permeability of $k = 22.4\,\mathrm{mD}$. Meanwhile the clay layer through which the injected H_2 drains is idealized as being impermeable except for an isolated fissure situated at a horizontal distance $x_f = 50\,\mathrm{m}$ from the source. The fissure is assumed to have a width and depth of 2 m and 1 m, respectively, and is characterized by $K = 0.3$, 0.5 or 0.7. Finally, we assume $\theta = 0°$ and consider the evolution of the flow over a 10 year period.

Given all of the above parameters, figure 2.14 shows $\tilde{B}^*_{\text{disp}}$ as a function of q_s. As expected from the model predictions of the previous section, the proportion of H_2 that mixes with the cushion gas through dispersion decreases with the source volume flow rate. Moreover, and as expected, $\tilde{B}^*_{\text{disp}}$ is larger when more H_2 is allowed to drain, i.e. when K is comparatively large. Results such as those shown in figure 2.14 are helpful because they can, for given K, identify the minimum source volume flow rate necessary to limit losses by dispersion to a particular value. For example, if, as suggested by the dashed line of figure 2.14, the maximum loss fraction were set to 5%, the minimum possible q_s could be identified for different fissure permeabilities. Note that this minimum value of

the source volume flow rate, $(q_s)_{\min}$ decreases with K. Obviously, as K tends to zero (indicating a fissure of very limited outflow capacity), $(q_s)_{\min}$ also tends to zero.

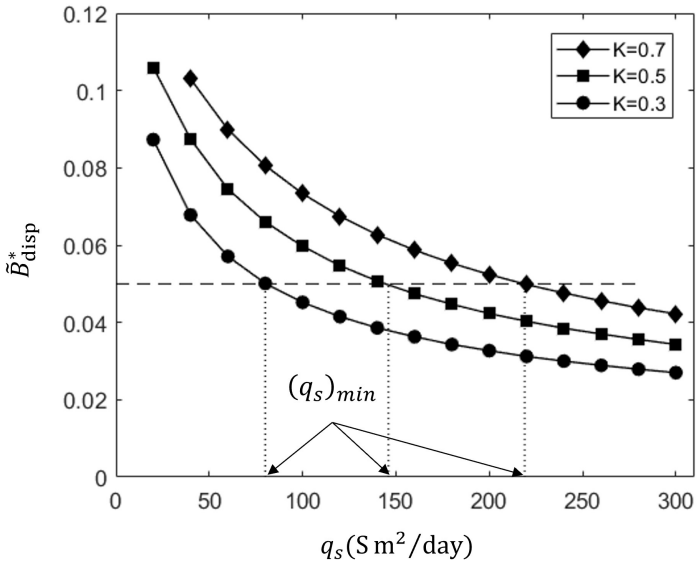

Figure 2.14: Fraction of H_2 lost to dispersion vs. source volume flow rate for the example of section 2.6. The horizontal dashed line assumes a maximum loss fraction of 5%.

The preceding analysis can be criticized for prioritizing injectate losses due to dispersion over those due to draining. Indeed, H_2 losses by either mechanism have the potential to make otherwise profitable ventures unattractive economically. On the other hand, there are scenarios such as the "selective technology" advocated by Feldmann *et al.* (2016) for which H_2 injection or withdrawal occur simultaneously to/from adjacent sandstone layers. In such a scenario, H_2 drained from one layer can be extracted from another layer and so is not necessarily lost to the geological formation. Rather different considerations apply to dispersion because any attempt to produce H_2 that has mixed with cushion gas requires the ability, at the surface, to separate H_2 from, say, CH_4 or N_2. The expenses associated with such surface separation operations justify our emphasis on dispersion vs. draining as a key loss mechanism for H_2.

Notwithstanding the conclusion of the previous paragraphs, it should be recalled that our analysis neglects a concentration dependence on viscosity. Strictly speaking, this assumption is incorrect for UHS-type applications: the viscosity of pure H_2 is less than that of a mixture of H_2 and cushion gas. Because we do not account for the greater mobility of the bulk vs. the dispersed phase, our

model likely overestimates the volume of the latter relative to the former though by how much is not straightforward to quantify. In a similar, though more complicated, spirit our model obviously falls well short of permitting the kinds of fingering instabilities that may arise as a result of a Taylor-Saffman-type instability and the injection of a less viscosity fluid into a more viscous fluid. The modification of our momentum equations to include a concentration-dependent viscosity shall be the subject of future investigations.

2.7 Summary and conclusions

A theoretical model is developed for a porous media gravity current consisting of a bulk phase and a dispersed phase – see figure 2.1. Our theoretical model of section 2.3 considers local drainage along the bottom boundary, which may be either horizontal or inclined. Model equations are robust enough to capture the essential physical processes of draining and dispersion but are simple enough to be solved using a straightforward numerical algorithm. To this end, we solve the non-dimensional governing equations by defining five non-dimensional parameters namely the inclination angle, θ, the upstream flow parameter, Γ, of (2.26 a), the permeability ratio, K, of (2.26 b), the fissure width, ξ^*, and the fissure length, l^*. We surmise that all five non-dimensional parameters influence the degree of dispersion. However, l^* exerts a subordinate influence compared to Γ, K, ξ^* and θ. Increasing one or both of Γ and θ increases the gravity current front speed and so increases the degree of dispersion. With reference to the definition of the entrainment velocities w_{e1} and w_{e2}, increasing the gravity current speed makes the entrainment more robust. This supports the idea that the volume of the dispersed phase is significantly larger when we increase parameters such as Γ or θ that increase the driving force for gravity current flow. Dispersion may also be augmented by causing more (bulk phase) fluid to drain through the fissure, which is realized as either of K or ξ^* is increased or l^* is decreased. Because drainage directly removes mass from the bulk phase, increasing the drainage leads to more separation between the leading edges (or nose positions) of the bulk and dispersed phases.

Complementing our theoretical results, a COMSOL-based numerical model is developed – see

section 2.4. The numerical model is exploited to estimate the approximate optimum value of the entrainment coefficient, ε, which appears as a parameter in the theoretical model e.g. (2.16-2.18). Through this analysis, we find that the error minimizing value of ε is a function of the inclination angle, θ, as depicted graphically in figure 2.7. With the appropriate value of ε so selected, we find from figures such as 2.8, 2.9 and 2.10 generally good agreement between theory and numerical simulation. In other words, our model of section 2.3 does a reasonable job of predicting the fractions of fluid or solute that appear in the dispersed phase. Our theoretical model also provides generally accurate estimates of the separation distance between the noses of the bulk and dispersed phases. Note, however, that comparisons are restricted to the region of the parameter space for which the degree of draining and subsequent dispersion is not too severe. The results of figure 2.6 suggest that our theoretical model makes inaccurate predictions of the shape of the dispersed phase when K is so large and draining is so vigorous that little or no bulk fluid appears downstream of the source. The modeling of this more complicated case is left for future investigations.

Our study is motivated by the need to address uncertainties in H_2 storage in depleted natural gas reservoirs. Mixing of H_2 with resident cushion gas is an inevitable facet of depleted reservoir-based UHS systems, particulaly in the medium to long term (Feldmann *et al.*, 2016). Granted our theoretical and numerical models are predicated on a number of simplifying assumptions e.g. ignoring viscosity variations, compressibility effects, ambient counterflow, or possible bio-geochemical reactions involving H_2. Progressively relaxing these (and related) assumptions are topics for future study. It would also be interesting to consider not localized but rather distributed drainage c.f. Pritchard *et al.* (2001), Goda & Sato (2011) and Bharath *et al.* (2020). Work on this latter problem is already underway and will be reported upon in a future publication.

Chapter 3

Porous media gravity current flow over an interbed layer: the impact of dispersion and distributed drainage [1,2]

3.1 Abstract

Motivated by buoyancy-driven flows within geological formations, we study the evolution of a (dense) gravity current in a porous medium bisected by a thin interbed layer. The gravity current experiences distributed drainage along this low-permeability boundary. Our theoretical description of this flow takes into account dispersive mass exchange with the surrounding ambient fluid by considering the evolution of the bulk and dispersed phases of the gravity current. In turn, we model basal draining by considering two bookend limits, i.e. no mixing versus perfect mixing in the lower layer. Our formulations are assessed by comparing model predictions against the output of complementary numerical simulations run using COMSOL. Numerical output is essential both for determining the value of the entrainment coefficient used within our theory and for assessing the reasonableness of key modeling assumptions. Our results suggest that the degree of dispersion depends on the dip angle and the depth and permeability of the interbed layer. We further find that the nose position predictions made by our theoretical models are reasonably accurate up to

[1]Sheikhi. S. & Flynn, M. R. 2024 Porous media gravity current flow over an interbed layer: the impact of dispersion and distributed drainage *J. Fluid Mech.* **984**, A33.

[2]Here, a positive inclination angle is defined as up-dip rather than down-dip in previous chapter to maintain consistency with the flow in geological layers.

the point where the no mixing model predicts a retraction of the gravity current front. Thereafter, the no mixing model significantly under-predicts, and the perfect mixing model moderately over-predicts, numerical data. Reasons for the failure of the no mixing model are provided, highlighting the importance of convective instabilities in the lower layer. A regime diagram is presented that defines the parametric region where our theoretical models do versus do not yield predictions in good agreement with numerical simulations.

3.2 Introduction

In layered porous media, the flow of a dense (buoyant) fluid into a buoyant (dense) ambient leads to the formation of gravity currents, where predominantly the flow velocity is aligned with the bottom (top) boundary. Porous media gravity currents are associated with a wide variety of geophysical flows, whether naturally-occuring, e.g. seawater contamination of coastal aquifers (Werner *et al.*, 2013; Costall *et al.*, 2020), or else related to human activities, e.g. underground hydrogen storage (UHS) (Feldmann *et al.*, 2016; Tarkowski, 2019; Muhammed *et al.*, 2023) or CO_2/acid gas sequestration (Ajayi *et al.*, 2019; Ali *et al.*, 2022; Warnecki *et al.*, 2021). Not surprisingly, a significant volume of research has been driven by the need to understand the dynamics of porous media gravity currents, particularly as they relate to energy industry applications.

In a pioneering study, Huppert & Woods (1995) established initial models for porous media gravity current flow. They proposed a similarity solution that was then verified through laboratory experiments. Huppert & Woods (1995) showed that a gravity current spreads as $t^{2/3}$ when fed by a constant-flux source. (Separately, they also derived similarity solutions for a general power-law influx condition). Many extensions to the Huppert & Woods seminal analysis have been pursued. For example, Hesse *et al.* (2007), MacMinn *et al.* (2012), Pegler, Huppert & Neufeld (2014) and Zheng *et al.* (2015) have examined similar examples of buoyancy-driven flow but in porous media that are confined vertically. A question of recent interest, which is more relevant to the research described in this study, is the impact of a heterogeneous porous medium, particularly when some fraction of the injectate is allowed to drain through local or distributed fissures. For example,

Anderson, McLaughlin & Miller (2003) investigated the movement of gravity currents in strongly heterogeneous porous media using homogenization methods. They found that by employing appropriate coefficients, one can project the similarity solution appropriate for a (long and thin) gravity current in a uniform medium to gravity current flow in horizontally- or vertically-layered porous media. Moreover, Pritchard *et al.* (2001) and Farcas & Woods (2009) studied distributed drainage over a thin permeable layer. Pritchard's investigation considered miscible flow with drainage along a horizontal layer while Farcas & Woods (2009) studied immiscible flow with drainage along an inclined layer. Meanwhile, Neufeld & Huppert (2009) studied the flow of gravity currents of supercritical CO_2 in thin layers representing the Utsira formation beneath the North Sea. In contrast to the modeling approach of Pritchard *et al.* (2001) who did not consider the possible dynamical influence of the drained fluid on the evolution of the gravity current, Neufeld & Huppert (2009) hypothesized that when gravity current fluid drains into the interbed layers that separate adjacent permeable layers, such an influence is manifest. More precisely, the weight of the drained fluid adds to the driving force for draining so that, over time, the velocities of drainage and of the gravity current front become respectively large and small. Neufeld & Huppert (2009) thereby identified three distinct regimes for the drainage of (dense) gravity current fluid, i.e. drainage is driven primarily by (i) the weight of the gravity current, (ii) the combined weight of the gravity current and the fluid already drained into the lower layer, and (iii) the weight of the drained fluid. Regimes (ii) and (iii) are respectively associated with the arrest and retraction of the gravity current front. Similar kinds of flow behavior have been documented in the related studies of Goda & Sato (2011), Acton *et al.* (2001), Sahu & Flynn (2017) and Bharath *et al.* (2020) who examined, theoretically and experimentally, distributed drainage over a deep lower layer having a relatively small permeability. Most notably, and consistent with Pritchard *et al.* (2001) and Farcas & Woods (2009), these related studies found that gravity currents stop elongating when the rate of basal drainage from the gravity current underside matches the source influx.

Most of the above research ignores mass transfer between the gravity current and the ambient fluid saturating the porous medium, e.g. by application of a "sharp interface" assumption in theoretical models. By contrast, and in the context of CO_2 sequestration, Neufeld *et al.* (2010),

MacMinn *et al.* (2012), Pegler, Huppert & Neufeld (2014) and Khan *et al.* (2022) investigated mixing due to convective dissolution in porous media buoyancy-driven flow. Also, mass transfer processes associated with seawater intrusions into coastal aquifers were considered by Huyakorn *et al.* (1987) and Paster & Dagan (2007). In such examples of miscible porous media flow, the key modes of mass transfer are diffusion and hydrodynamic dispersion. Mixing by dispersion is likewise important when considering the societally-important possibility of storing hydrogen (H_2) in depleted natural gas reservoirs. Indeed, the combination of H_2 leakage through cap-rock and the dispersive mixing of H_2 into the "cushion gas" that otherwise occupies the porous medium reduces the volume of H_2 that can be recovered economically. Quantifying such details is challenging; e.g. the study by Lubon & Tarkowski (2021) estimated the amount of recoverable H_2 as anywhere from 50% to 80% depending on, among other factors, the number of H_2 injection cycles and the degree of heterogeneity within the medium. As regards this latter variable, Feldmann *et al.* (2016) highlighted the possibility of leakage through semi-permeable boundaries by examining H_2 migration through a heterogeneous porous medium consisting of sandstone layers separated by tight clay interlayers.

Also in the context of miscibility, Szulczewski & Juanes (2013) studied, theoretically, mixing when a fixed amount of dense fluid is released in vertically confined porous media. They reported evidence of various regimes associated with the flow evolution. At early and more especially late times, diffusion is vital, especially when it is coupled with Taylor dispersion. However, at intermediate times, diffusion is insignificant, such that application of the sharp interface assumption is approximately correct. Meanwhile, Sahu & Neufeld (2020) studied, theoretically and experimentally, the mixing that occurs in a homogeneous porous medium due to velocity-dependant transverse dispersion in gravity currents. In their theoretical model, they exploited mass and buoyancy conservation laws in conjunction with a semi-empirical expression for dispersion, analog to turbulent entrainment in free shear flows. Sahu & Neufeld (2020) tuned the associated entrainment coefficient from their theoretical model with measured results from the laboratory. Although transverse dispersion leads, through 'dispersive entrainment,' to a thickening of the gravity current, the neglect of longitudinal dispersion means that the gravity current length predicted by Sahu &

Neufeld (2020) must match that anticipated by the sharp interface model of Huppert & Woods (1995).

The equivalence documented at the end of the previous paragraph runs contrary to the experimental observations of Bharath *et al.* (2020). They studied gravity currents propagating along a permeability jump and demonstrated that dispersion leads to enhanced gravity current elongation. The difference of length compared to the sharp interface case was attributed to longitudinal dispersion. The Sahu & Neufeld model therefore appears most effective in describing gravity current flow through homogeneous media where drainage is not dynamically-significant. Recognizing that real geological media are not always so ideal, Sahu & Neufeld (2023) conducted laboratory experiments to examine dispersive mixing in gravity currents over layered strata. They showed that the mixing that occurs in heterogeneous media is approximately twice that in homogeneous media having otherwise identical properties. To quantify the effects of heterogeneity on mixing, Sahu & Neufeld (2023) introduced a term called the 'jump factor,' which characterizes the degree of layering within a porous medium. Sahu & Neufeld (2023) further demonstrated that the early-time entrainment into the gravity current renders it thick with a rounded nose. Therefore, the long and thin assumption, which is vital in developing a theoretical model, becomes suspect. Sahu & Neufeld (2023) used their experimental findings to derive semi-empirical equations that estimate the gravity current height and length as functions of time and other parameters. The semi-empirical correlations in question do not, however, distinguish between bulk and dispersed phases within the gravity current. A pioneering theoretical attempt at drawing such a distinction was made by Sahu & Neufeld (2020), whose approach was later expanded upon by Sheikhi *et al.* (2023). The authors of this latter investigation separated the bulk and dispersed phases to study dispersive mixing in gravity currents elongating over inclined porous media and experiencing local drainage through discrete fissures. Sheikhi *et al.* (2023) thereby extended the theoretical model of Sahu & Neufeld (2020) by introducing two entrainment velocities, i.e. w_{e1}, which is associated with entrainment from the bulk phase to the dispersed phase, and w_{e2}, which is associated with entrainment from the surrounding ambient to the dispersed phase. They assumed an identical entrainment coefficient associated with w_{e1} and w_{e2}, and determined the numerical value of this entrainment coefficient by

fitting theoretical predictions against COMSOL-based numerical simulations meant to mimic similitude laboratory experimental conditions. Their theoretical model, combined with the COMSOL numerical simulations, revealed that five parameters can affect the amount of dispersive mixing in porous media gravity currents experiencing local drainage: (i) Γ, which represents flow conditions upstream of the local fissure(s); (ii) K, which represents the permeability ratio (fissure-to-medium); (iii) ξ, which represents the fissure width; (iv) l, which represents the fissure depth; and (v) θ, which represents the dip angle.

A primary objective of this study is to extend the work of Sheikhi *et al.* (2023) to gravity currents experiencing distributed drainage, as is more representative of many geological flows compared to the case of localized drainage. To do so, we suppose that the gravity current propagates through a porous medium and over a thin interbed layer having a lower – possibly substantially lower – permeability. We develop a theoretical model and a complementary numerical model to study the details of the dispersive mixing relevant to this case. In the former case, our formulation is predicated on two linearizations of the real behavior. The first pertains to fluid mechanics and supposes a linear entrainment law of the type proposed for high-Reynolds number shear flows by Ellison & Turner (1959) and for low-Reynolds number porous media flows by Sahu & Neufeld (2020). The second pertains to thermodynamics and supposes a linear equation of state, i.e. a linear relationship between fluid density and solute concentration. The latter linearization in particular seems well-justified in a UHS context: measured data from Hassanpouryouzband *et al.* (2020) suggest that nonlinear terms in the equation of state describing H_2/CH_4 mixtures have minor significance. Meanwhile, the validity of the former linearization is discussed in more detail below. A further objective of our study is to characterize the drainage of gravity current fluid into the interbed layer and, from there, into a semi-infinite layer of larger permeability below[3].

The rest of the Chapter is organized as follows: Section 3.3 derives the theoretical model for the gravity current by incorporating a distributed drainage formulation. Particular attention is

[3]For analytical convenience and consistent with previous studies (e.g. Huppert & Woods 1995; Neufeld & Huppert 2009; Bharath *et al.* 2020, and Sahu & Neufeld 2020), we assume a dense rather than a light gravity current. As a result, the gravity current appears "upside-down" relative to those expected e.g. in UHS-type flows. Note, however, that the flow orientation does not impact the flow dynamics provided we apply the Boussinesq approximation, which supposes relatively modest density differences between the injectate and the ambient fluid.

paid to two limiting cases, which assume either no mixing or perfect mixing in the lowest of the porous layers. In section 3.4, we outline the COMSOL-based numerical simulations conducted to validate and contextualize the predictions of the theoretical model. In section 3.5, we discuss these predictions in more detail and contrast the predictions with complementary output from the numerical simulations. Finally, key findings of the current work are reviewed, and prospects for future research are identified in section 3.6.

3.3 Theoretical model

3.3.1 Governing equations

We examine the flow of a gravity current, $z \geq 0$ in figure 3.1, that occurs when a dense fluid with a density of ρ_s is injected into a uniform porous medium with a constant permeability k. This medium is intersected by a thin interbed layer of permeability $k_b < k$ with inclination angle θ and depth ξ. Thus the interbed layer occupies the vertical expanse $-\xi < z < 0$. In general, and with the application of (buoyant) H_2 storage in an anticline structure in mind, we consider an up-dip inclination angle. The (x, z) coordinate system that describes the directions along and perpendicular to the slope, is derived by rotating the natural coordinates (X, Z) in a clockwise direction by the dip angle θ. The red dot shown in figure 3.1 signifies the isolated source, and the origin for both coordinate systems is located at this same point.

The continuity equation for the bulk (or unmixed) phase of the gravity current experiencing drainage over its lower boundary reads

$$\frac{\partial h_1}{\partial \tilde{t}} + \frac{\partial}{\partial x}(u_1 h_1) = -w_{e1} - w_{d1}\,. \tag{3.1}$$

Here, h_1 is the height of the bulk phase, u_1 is the bulk phase velocity, and w_{e1} and w_{d1} are velocities that respectively account for entrainment from the bulk to the dispersed phase and drainage from the bulk phase through the lower layer. Also, $\tilde{t} = t/\phi$, in which ϕ is the porosity. (Note that all velocities in our theoretical model are Darcy velocities.)

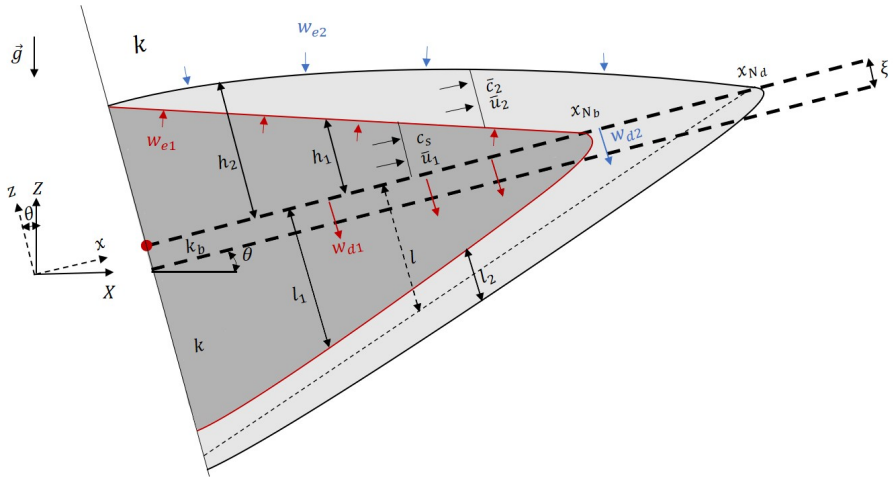

Figure 3.1: [colour] Schematic of a leaky gravity current propagating along, and draining through, the permeability jump associated with an interbed layer of thickness ξ. We assume equal permeability k in the upper and lower layers, and a reduced permeability k_b in the interbed layer. The gravity current and the fluid that drains from the gravity current consist of bulk and dispersed phases. These are respectively confined by the red and black curves. Meanwhile, the dashed curve that is drawn through the lower two layers signifies the equivalent depth of draining fluid, assuming that this draining fluid consists solely of bulk fluid, i.e. has a density that matches the source density. The variables h_1, h_2, u_1, u_2, w_{e1}, w_{e2} and $\bar{c}_2$ depend on x and $\tilde{t}$. Conversely the variables x_{N_b} and x_{N_d} depend only on $\tilde{t}$. The vertical scale is exaggerated in this schematic.

Similarly, the continuity equation for the dispersed phase can be stated as

$$\frac{\partial h_2}{\partial \tilde{t}} + \frac{\partial}{\partial x}\big[u_2(h_2 - h_1)\big] = -\frac{\partial}{\partial x}(u_1 h_1) + w_{e2} - w_{d1} - w_{d2}\,, \tag{3.2}$$

where $h_2 - h_1$ is the thickness of the dispersed phase, u_2 (assumed independent of z) is the advection speed of the dispersed phase, w_{e2} is the entrainment velocity from the ambient to the dispersed phase, and w_{d2} is the drainage velocity from the dispersed phase through the lower layer. The latter velocity must be interpreted with some care because it is not defined everywhere along the extent $0 \le x \le x_{N_d}$ occupied by the dispersed phase (and likewise for w_{d1}). We clarify this situation when formally defining the draining velocities w_{d1} and w_{d2} below.

Although the solute concentration in the bulk phase is equal to the source concentration c_s by assumption, the concentration in the dispersed phase varies between 0 and c_s. Therefore a z-averaged solute concentration $\bar{c}_2$ is defined in the dispersed phase. Solute conservation in the

dispersed phase can be expressed as

$$\frac{\partial b_2}{\partial \tilde{t}} + \frac{\partial}{\partial x}(u_2 b_2) = w_{e1} c_s \, \mathrm{H}(x_{N_b} - x) - w_{d2} \bar{c}_2 \,, \tag{3.3}$$

in which $b_2 = \bar{c}_2(h_2 - h_1)$ is the buoyancy of the dispersed phase, averaged over depth. Meanwhile $\mathrm{H}(x_{N_b} - x)$ is a Heaviside step function, which is zero everywhere except when $x_{N_b} > x$, where x_{N_b} indicates the front position of the bulk phase. In this study, we follow previous work on entraining flows from either the turbulent free shear flow literature (e.g. Ellison & Turner 1959) or, much more importantly, the porous media flow literature (e.g. Sahu & Neufeld 2020) and so consider a linear entrainment relationship. Accordingly, the entrainment velocities are defined as $w_{e1} = \varepsilon u_1$ and $w_{e2} = \varepsilon u_2$ where ε is the dispersive entrainment coefficient. Extrapolation of these relationships to more complicated formulations (e.g. $w_{e1} = \varepsilon_1 u_1$ and $w_{e2} = \varepsilon_2 u_2$ with $\varepsilon_1 \neq \varepsilon_2$ or $w_{ei} \propto u_i^\lambda$ or $w_{e1} \propto |u_1 - u_2|$) remains a topic to be examined in future studies. Our reluctance to pursue such a line of inquiry here stems not from the physical illogicality of these alternative formulations but rather from our desire to minimize model complexity and the number of variables whose value must be set by comparison with numerical output.

By considering a hydrostatic pressure gradient throughout the gravity current and using Darcy's law, the horizontal velocity in each phase is given by

$$u_1(x, \tilde{t}) = -\frac{kg\beta}{\nu}\Big[\frac{\partial b_2}{\partial x}\cos\theta + c_s\Big(\frac{\partial h_1}{\partial x}\cos\theta + \sin\theta\Big)\Big] \,, \tag{3.4}$$

$$u_2(x, \tilde{t}) = -\frac{kg\beta}{\nu}\Big[\frac{\partial\,(\bar{c}_2 h_2)}{\partial x}\cos\theta + \bar{c}_2 \sin\theta\Big] \equiv -\frac{kg\beta}{\nu}\Big[\frac{\partial}{\partial x}\Big(\frac{b_2 h_2}{h_2 - h_1}\Big)\cos\theta + \bar{c}_2 \sin\theta\Big] \tag{3.5}$$

– see Sheikhi *et al.* (2023). Here, β is the solute contraction coefficient, which we borrow from the (assumed linear) equation of state $\rho = \rho_0(1 + \beta\, c)$ in which ρ_0 is the density of the uncontaminated ambient fluid. Also, ν is the kinematic viscosity, which we assume to be the same throughout the bulk and dispersed phases. By inserting (3.4-3.5) and the expressions for the entrainment velocities

$w_{e,1}$ and $w_{e,2}$ into (2.2-3.3), we obtain the following modified governing equations:

$$\frac{\partial h_1}{\partial \tilde{t}} + \frac{kg'_s}{\nu}\frac{\partial (h_1 U)}{\partial x} = -\varepsilon \frac{kg'_s}{\nu} U - w_{d1}\,, \tag{3.6}$$

$$\frac{\partial h_2}{\partial \tilde{t}} - \frac{kg'_s}{\nu}\frac{\partial}{\partial x}\Big[(h_2 - h_1)\Big(\frac{\partial \Psi}{\partial x} + C\sin\theta\Big) - h_1 U\Big] = -\varepsilon \frac{kg'_s}{\nu}\Big(\frac{\partial \Psi}{\partial x} + C\sin\theta\Big) - w_{d1} - w_{d2}\,, \tag{3.7}$$

$$\frac{\partial b_2}{\partial \tilde{t}} - \frac{kg'_s}{\nu}\frac{\partial}{\partial x}\Big[b_2\Big(\frac{\partial \Psi}{\partial x} + C\sin\theta\Big)\Big] = \varepsilon \frac{kg'_s}{\nu} U c_s\, H(x_{N_b} - x) - w_{d2}\, C\, c_s\,. \tag{3.8}$$

In the above equations, we have introduced the following symbols:

$$U = -\Big(\frac{1}{c_s}\frac{\partial b_2}{\partial x} + \frac{\partial h_1}{\partial x}\Big)\cos\theta - \sin\theta\,, \tag{3.9}$$

$$\Psi = \frac{b_2 h_2}{c_s(h_2 - h_1)}\cos\theta\,, \tag{3.10}$$

$$C = \frac{\overline{c}_2}{c_s} \equiv \frac{b_2}{c_s(h_2 - h_1)}\,. \tag{3.11}$$

Note that U, Ψ and C are defined solely for the purpose of simplifying our notation, i.e these variables do not carry any particular physical meaning. Before studying (3.7-3.8) in more detail, it is necessary to define the drainage velocities w_{d1} and w_{d2}. These velocities are influenced by the degree of mixing occurring in the lower layer of the porous medium. Because predicting the extent of mixing in this lower layer is a complicated task that relies on numerous factors (see e.g. figure 10 in Bharath *et al.* (2020) and the discussion thereof), we will confine ourselves to two limiting scenarios, which we label as perfect mixing and no mixing. Both of the perfect mixing and no mixing cases are idealizations. Consistent with Pritchard *et al.* (2001), the former assumes that dense fluid that drains through the interbed layer immediately dissolves into lower layer ambient fluid. Meanwhile the latter scenario supposes that mixing details can be ignored in this lower layer (even though they figure prominently in our description of the gravity current flow). Thus do we assume that the draining flows evolve as depicted in figure 3.1. The perfect mixing and no mixing idealizations are helpful bookend-limiting cases that we expect to often bound the true behavior of the evolving flow.

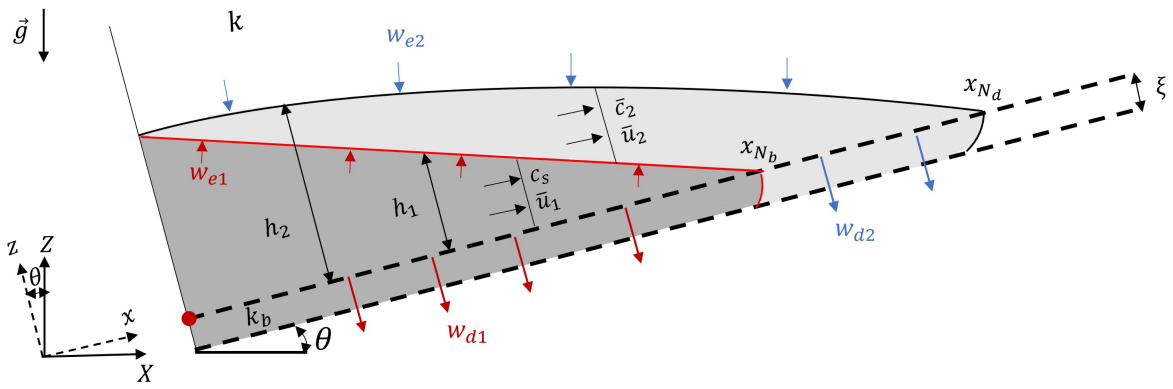

Figure 3.2: [colour] Schematic of a leaky gravity current experiencing perfect mixing in (and therefore immediate removal from) the lower layer. The red line indicates the bulk interface and the black line indicates the dispersed interface.

Perfect mixing

As noted above, the perfect mixing regime considers an immediate and total dissolution of drained gravity current fluid when this dense fluid reaches the lower layer. In turn, and because this lower layer is semi-infinite in extent, it maintains a negligible solute concentration. The perfect mixing regime is supposed to be approached when the density difference between the gravity current fluid and the ambient fluid is comparatively large, or when the permeability in the interbed layer is much smaller than elsewhere. As suggested by figure 3.2, perfect mixing is analogous to a situation where drained fluid is removed from the domain as soon as it exits the interbed layer. Note that such a removal does not invalidate the equations of subsection 3.3.1, which are focused on the flow dynamics in the domain $z > 0$.

From figure 3.2, the drainage velocities w_{d1} and w_{d2} can be determined by using the z-component of Darcy's law, i.e.

$$\frac{\partial p}{\partial z} = -\rho g' \cos\theta - \frac{\mu}{k} w \,, \tag{3.12}$$

where μ is the dynamic viscosity, p is the pressure, and $g' = g\beta c$ is the reduced gravity. We enforce

continuity of pressure and of the vertical flux at $z = 0$ and thereby conclude that

$$w_{d1}(x,\tilde{t}) = \begin{cases} \frac{k_b g_s'}{\nu}\left(\frac{c_s h_1 + b_2}{c_s\,\xi} + 1\right)\cos\theta & 0 \le x < x_{N_b} \\ 0 & x_{N_b} \le x \le x_{N_d} \end{cases} . \tag{3.13}$$

This last result considers the draining of bulk phase fluid through the upper and interbed layers. Meanwhile, and by examining the dispersed phase, it can be shown that

$$w_{d2}(x,\tilde{t}) = \begin{cases} 0 & 0 \le x < x_{N_b} \\ \frac{k_b g_s'}{\nu}\,C\left(\frac{h_2}{\xi} + 1\right)\cos\theta & x_{N_b} \le x \le x_{N_d} \end{cases} . \tag{3.14}$$

(The derivation of equations 3.13 and 3.14 is outlined in Appendix B.1). Note that the (degenerate) limit $\xi \to 0$ is not necessarily associated with the appearance of singularities in (3.13) and (3.14) because $\xi \to 0$ likewise implies $k_b \to 0$.

No mixing

If no mixing occurs in the lower layer, then the solute concentration of the drained fluid is the same as the solute concentration of the gravity current fluid directly above it. In this case, the drainage velocities are obtained by applying (3.12) for both the bulk and dispersed phases and through all three layers of figure 3.1. To wit,

$$w_{d1}(x,\tilde{t}) = \begin{cases} \frac{k_b g_s'}{\nu}\cos\theta \begin{cases} \left(\frac{c_s h_1 + b_2}{c_s\,l} + 1\right) & l < \xi \\ \frac{c_s h_1 + b_2 + c_s l}{(1-K)c_s\,\xi + K c_s\,l} & l \ge \xi \end{cases} & 0 \le x < x_{N_b} \\ 0 & x_{N_b} \le x \le x_{N_d} \end{cases} , \tag{3.15}$$

and

$$w_{d2}(x,\tilde{t}) = \begin{cases} 0 & 0 \le x < x_{N_b} \\ \frac{k_b g_s'}{\nu}\cos\theta \begin{cases} \left(\frac{h_2}{l} + 1\right) & l < \xi \\ \frac{h_2 + l}{(1-K)\,\xi + K l} & l \ge \xi \end{cases} & x_{N_b} \le x \le x_{N_d} \end{cases} . \tag{3.16}$$

(The derivation of equations 3.15 and 3.16 is outlined in Appendix B.2; No corresponding expressions are provided for u_{d1} and u_{d2} because, in the rotated or $x-z$ coordinate system, u_{d1} and u_{d2} do not impact the evolution of l.) Here, $K = \frac{k_b}{k}$ is the permeability ratio. When $\xi \to \infty$, (3.15)-(3.16) are consistent with the drainage formulation of Acton *et al.* (2001) for a gravity current propagating over a deep layer that is permeable but "tight". By contrast, we again avoid consideration of the limit $\xi \to 0$: in the absence of an interbed layer, figure 3.1 must be redrawn completely because source fluid will now fall vertically in the form of a descending plume. Such a flow, studied at some length by Sahu & Flynn (2015) and Gilmore *et al.* (2021), is not the focus of the current work.

Finally, and in defining the depth of the contaminated fluid in the lower layer, we simplify the analysis by defining $l(x, \tilde{t})$ as an equivalent depth such that all of the drained fluid in the lower layer has the same uniform solute concentration c_s. The evolution equation for l therefore reads

$$\frac{\partial l}{\partial \tilde{t}} = \begin{cases} w_{d1} & 0 \le x < x_{N_b} \\ C\, w_{d2} & x_{N_b} \le x \le x_{N_d} \end{cases} . \tag{3.17}$$

In solving (3.17), we acknowledge that we do not distinguish rigorously between the bulk and dispersed phases for $z < 0$. On the other hand, no such sacrifice applies for $z > 0$ and thus our dynamical description of the bulk and dispersed phases of the gravity current is not jeopardized.

3.3.2 Boundary conditions

As shown in Sheikhi *et al.* (2023), boundary conditions for a gravity current consisting of bulk and dispersed phases are

$$-\frac{k g_s'}{\nu}\Big[\Big(\frac{1}{c_s}\frac{\partial b_2}{\partial x} + \frac{\partial h_1}{\partial x}\Big) h_1 \cos\theta + h_1 \sin\theta\Big]_0 = q_s\,, \qquad h_1|_{x_{N_b}} = 0\,, \tag{3.18a,b}$$

$$h_2|_0 = h_1|_0\,, \qquad h_2|_{x_{N_d}} = 0\,, \tag{3.18c,d}$$

$$b_2|_0 = 0\,, \qquad b_2|_{x_{N_d}} = 0\,. \tag{3.18e,f}$$

Whereas the last five of these expressions are self-explanatory, the first (influx) boundary condition merits some additional discussion. In this spirit, (3.18 a) signifies that all of the injectate supplied by the source is added to the rear of the gravity current such that the source volume flux matches the gravity current volume flux measured at $x = 0$. Thereafter, and consistent with the numerical treatment of the source to be described in section 3.4, gravity current fluid may propagate down-dip or else drain into the interbed layer.

3.3.3 Non-dimensional governing equations

Following Goda & Sato (2011), we define a characteristic length scale, Π_1, and a characteristic time scale, Π_2, as

$$\Pi_1 = \frac{\nu q_s}{k g_s'} \qquad \text{and} \qquad \Pi_2 = q_s \left(\frac{\nu}{k g_s'} \right)^2 , \tag{3.19a,b}$$

respectively. Thus do we define the following dimensionless (starred) variables:

$$x^* = \frac{x}{\Pi_1} , \quad \xi^* = \frac{\xi}{\Pi_1} , \quad h_1^* = \frac{h_1}{\Pi_1} , \quad h_2^* = \frac{h_2}{\Pi_1} , \quad l^* = \frac{l}{\Pi_1} , \quad t^* = \frac{\tilde{t}}{\Pi_2} , \quad w^* = w \frac{\Pi_2}{\Pi_1} . \tag{3.20a-g}$$

Also, $c_2^* = \frac{c_2}{c_s}$. Note that for notational simplicity, we drop the superscript * such that all variables are now to be interpreted as dimensionless. (By necessity, however, we revert to dimensional variables in subsection 3.4.1 and in the appendices.) Accordingly, (3.7-3.8) may be rewritten as

$$\frac{\partial h_1}{\partial t} + \frac{\partial (h_1 U)}{\partial x} = -\varepsilon U - w_{d1} , \tag{3.21}$$

$$\frac{\partial h_2}{\partial t} - \frac{\partial}{\partial x} \Big[(h_2 - h_1) \Big(\frac{\partial \Psi}{\partial x} + C \sin\theta \Big) - h_1 U \Big] = -\varepsilon \Big(\frac{\partial \Psi}{\partial x} + C \sin\theta \Big) - w_{d1} - w_{d2} , \tag{3.22}$$

$$\frac{\partial b_2}{\partial t} - \frac{\partial}{\partial x} \Big[b_2 \Big(\frac{\partial \Psi}{\partial x} + C \sin\theta \Big) \Big] = \varepsilon U \, H(x_{N_b} - x) - w_{d2} \, C . \tag{3.23}$$

Here,

$$b_2 = c_2 \left(h_2 - h_1 \right) , \tag{3.24}$$

$$U = -\Big(\frac{\partial b_2}{\partial x} + \frac{\partial h_1}{\partial x} \Big) \cos\theta - \sin\theta , \tag{3.25}$$

$$\Psi = \frac{b_2\, h_2}{h_2 - h_1} \cos\theta\,, \tag{3.26}$$

$$C = \frac{b_2}{h_2 - h_1}\,. \tag{3.27}$$

Equations (3.21)-(3.23) comprise three equations in three unknowns, namely h_1, h_2 and b_2. The dimensionless boundary conditions to be coupled to these equations read

$$\Big[\Big(\frac{\partial b_2}{\partial x} + \frac{\partial h_1}{\partial x}\Big) h_1 \cos\theta + h_1 \sin\theta\Big]_0 = -1\,, \qquad h_1|_{x_{N_b}} = 0\,, \tag{3.28a,b}$$

$$h_2|_0 = h_1|_0\,, \qquad h_2|_{x_{N_d}} = 0\,, \tag{3.28c,d}$$

$$b_2|_0 = 0\,, \qquad b_2|_{x_{N_d}} = 0\,. \tag{3.28e,f}$$

When a state of perfect mixing can be assumed for the lower layer, the dimensionless drainage velocities that appear in (3.21)-(3.23) are given by

$$w_{d1} = K\cos\theta \begin{cases} \left(\frac{h_1+b_2}{\xi} + 1\right) & 0 \le x < x_{N_b} \\ 0 & x_{N_b} \le x \le x_{N_d} \end{cases}, \tag{3.29}$$

and

$$w_{d2} = K\cos\theta \begin{cases} 0 & 0 \le x < x_{N_b} \\ C\left(\frac{h_2}{\xi} + 1\right) & x_{N_b} \le x \le x_{N_d} \end{cases}, \tag{3.30}$$

where K is the aforementioned permeability ratio. For the no mixing case, by contrast, we write

$$w_{d1} = \begin{cases} K\cos\theta \begin{cases} \frac{h_1+b_2}{l} + 1 & l < \xi \\ \frac{h_1+b_2+l}{(1-K)\,\xi + Kl} & l \ge \xi \end{cases} & 0 \le x < x_{N_b} \\ 0 & x_{N_b} \le x \le x_{N_d} \end{cases}, \tag{3.31}$$

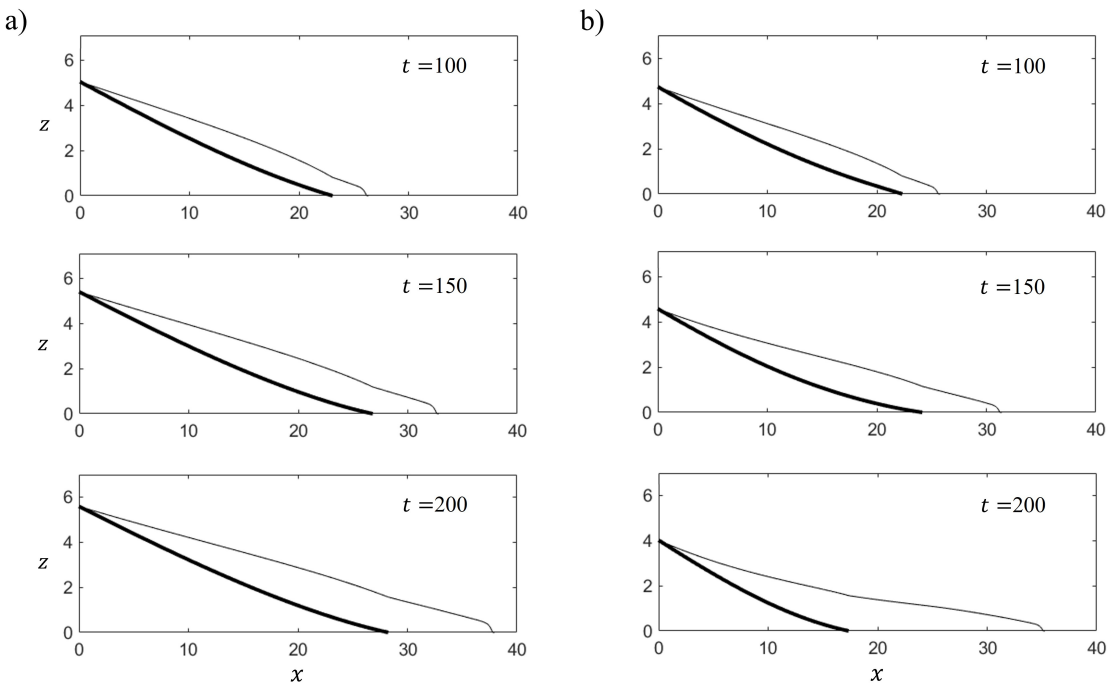

Figure 3.3: Theoretical predictions showing gravity current profiles assuming (a) perfect mixing, and, (b) no mixing in the lower layer. Thick lines represent the bulk interface and thin lines represent the dispersed interface. Here, $K = 0.0025$, $\xi = 0.333$ (equivalent to $K_{\text{eff}} \equiv K(1 + \frac{1}{\xi}) = 0.01$, see equation 3.40 below) and $\theta = 0°$. We further assume that $\varepsilon = 0.0344$. The justification for this choice will be presented in subsection 3.4.4.

and

$$w_{d2} = \begin{cases} 0 & 0 \le x < x_{N_b} \\ K\cos\theta \begin{cases} \frac{h_2}{l} + 1 & l < \xi \\ \frac{h_2 + l}{(1-K)\,\xi + Kl} & l \ge \xi \end{cases} & x_{N_b} \le x \le x_{N_d} \end{cases} . \tag{3.32}$$

Finally, the non-dimensional analogue of (3.17) becomes

$$\frac{\partial l}{\partial t} = \begin{cases} w_{d1} & 0 \le x < x_{N_b} \\ C\, w_{d2} & x_{N_b} \le x \le x_{N_d} \end{cases} \tag{3.33}$$

An explicit finite difference algorithm is employed to solve the governing equations. This approach discretizes spatial derivatives using backward finite differences. Note that, so as to prevent unrealistic singularities, we initialize l with a small value, i.e. $l(x, 0) = 10^{-3}$. Figures 3.3 a,b show

results for both the perfect mixing and no mixing cases. Because l is comparable to ξ at early times, the prediction for w_{d1} returned by (3.29) is similar to that returned by (3.31), and likewise when considering w_{d2}, for (3.30) and (3.32). As a result, and up to $t \simeq 100$, the gravity current propagates to a comparable extent in both scenarios. As time evolves, the l predicted by (3.33) for the no mixing case increases steadily. When l is similar in magnitude to h_2, the drainage velocity remains small such that the gravity current extends beyond the steady-state value that is realized in the long-time limit. As l continues to increase, however, the gravity current begins to retract, a pattern clearly evident from figure 3.3 (b). This pattern of extension and retraction is quite different from that noted in the perfect mixing case where the terminal length of the gravity current is approached monotonically. The difference of behavior in question therefore provides a convenient metric by which to assess the validity of one versus the other representation of lower layer mixing. However, before elaborating on such details and the results anticipated away from the bookend limiting cases of figures 3.3 a,b, it is first necessary to summarize the numerical technique used to resolve such flows.

3.4 Numerical simulations

The first purpose of the COMSOL-based numerical simulations is to approximate the value of ε in the theoretical models of section 3.3. Thereafter, we use numerical results to infer the strengths and weaknesses of the perfect mixing and no mixing models.

Consistent with the orientation of the flows depicted in figures 3.1 and 3.2, we consider the evolution of a dense gravity current through a less dense ambient. More precisely, and mimicking similitude laboratory experiments, we assume that the gravity current and ambient fluids are respectively comprised of salt and fresh water. Although this choice guides our selection of the equation of state, the results of section 3.5 are, in any event, non-dimensionalized so as to increase the generality of our research, i.e. make it applicable to flows spanning a broader range of time- and length-scales. Notwithstanding this preference for non-dimensional variables, it must be noted that $g_s' = 15\,\mathrm{cm/s^2}$ and $q_s = 0.3\,\mathrm{cm^2/s}$ in our simulations. Simulations are typically run for 20 minutes

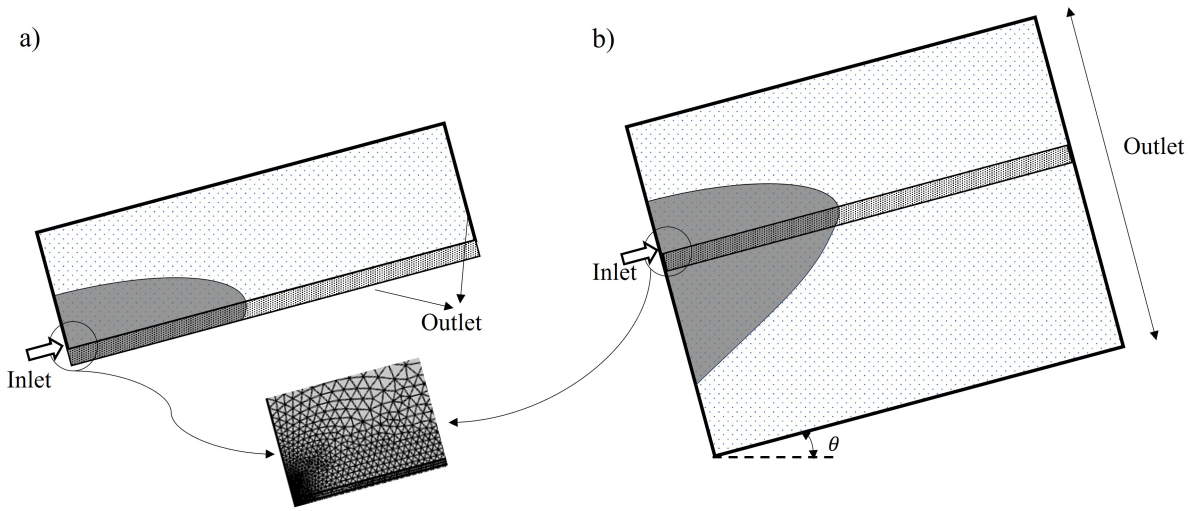

Figure 3.4: Schematic of the numerical set-up that similitude (a) perfect mixing (b) laboratory experiments.

after injection onset representing an investment of approximately 30 hours of wall clock time on an Intel Core i7-9700 CPU with 3.00 GHz and 16 GB memory. (By comparison, numerically-solving the theoretical model of section 3.3 requires only about 3% of the computational resources needed for the COMSOL simulations.)

3.4.1 COMSOL set-up

In order to determine the velocity and concentration fields in our numerical simulations, mass continuity, Darcy's equation, and a solute transport equation are solved. With COMSOL, this is achieved by leveraging the following two interfaces:

1. The Darcy's law (dl) interface prescribes the mass and momentum equations as

$$\frac{\partial u}{\partial x} + \frac{\partial w}{\partial z} = 0\,, \tag{3.34a}$$

$$\frac{1}{\rho_0}\frac{\partial p}{\partial x} + \frac{\nu}{k}u = +\frac{\rho}{\rho_0}g\sin\theta\,, \tag{3.34b}$$

$$\frac{1}{\rho_0}\frac{\partial p}{\partial z} + \frac{\nu}{k}w = \frac{\rho}{\rho_0}g\cos\theta\,, \tag{3.34c}$$

respectively.

2. The transport of diluted species in porous media (tds) interface solves the solute transport equation

$$\phi\frac{\partial c}{\partial t}+u\frac{\partial c}{\partial x}+w\frac{\partial c}{\partial z}=\phi\Big[\frac{\partial}{\partial x}\Big(D_{xx}\frac{\partial c}{\partial x}+D_{xz}\frac{\partial c}{\partial z}\Big)+\frac{\partial}{\partial z}\Big(D_{xz}\frac{\partial c}{\partial x}+D_{zz}\frac{\partial c}{\partial z}\Big)\Big]\,. \tag{3.35}$$

Here, c is the solute concentration, and D_{xx}, D_{xz} and D_{zz} are components of the dispersion tensor, D_{ij}. As explained by Bear (1972), this tensor can be defined based on two independent variables namely the longitudinal dispersivity a_L and the transverse dispersivity a_T, i.e.

$$D_{xx}=D_{\rm mol}+a_L\frac{u^2}{|\boldsymbol{V}|}+a_T\frac{w^2}{|\boldsymbol{V}|}\,, \tag{3.36a}$$

$$D_{zz}=D_{\rm mol}+a_L\frac{w^2}{|\boldsymbol{V}|}+a_T\frac{u^2}{|\boldsymbol{V}|}\,, \tag{3.36b}$$

$$D_{xz}=D_{\rm mol}+(a_L-a_T)\frac{|uw|}{|\boldsymbol{V}|}\,, \tag{3.36c}$$

where $D_{\rm mol}$ is the coefficient of molecular diffusion and $|\boldsymbol{V}|$ is overall velocity magnitude. Following Sheikhi *et al.* (2023), the dispersivity parameters a_L and a_T are predicted based on the empirical correlations of Delgado (2007) as

$$a_L=\begin{cases}0.5\,d_p & 300<\mathrm{Pe}<10^5\\ 0.025\,d_p & 300<\mathrm{Pe}<10^5\end{cases}\,,\qquad a_T=0.025\,d_p\,, \tag{3.37a,b}$$

in which Pe is Péclet number and d_p is the bead diameter. In this work, we consider $d_p=0.5\,\mathrm{mm}$ in line with similitude experiments of the type performed by Sahu & Flynn (2017) and Bharath *et al.* (2020). Note finally that the linear equation of state $\rho=\rho_0(1+\beta\,c)$ allows us to relate the density in (3.34b,c) with the solute concentration in (3.35).

3.4.2 Initial conditions and solver

Initially, it is assumed that the porous medium is filled with fresh water of density $\rho_0=0.998\,\mathrm{g/cm^3}$ such that the solute concentration is zero at $t=0$. The source consists of an opening, oriented

in z, of height 5 mm across which salt water is injected in x with a uniform velocity profile. We determine the salt water density from g'_s by applying

$$\rho_s = \left(1 + \frac{g'_s}{g}\right) \rho_0 \,. \tag{3.38}$$

To discretize (3.34) and (3.35), an unstructured triangular mesh (with local refinement in the neighborhood of the source) is employed – see figure 3.4. After performing a grid independency study, the governing equations are discretized in space using cubic shape functions for (3.34) and quadratic shape functions for (3.35). A third-order implicit backward differentiation formula (BDF) is employed for time discretization.

3.4.3 Preliminary validation

As described in more detail in Sheikhi *et al.* (2023), our COMSOL model is validated using different points of reference. First, we model the flow of a porous media gravity current along an impermeable boundary and observe a strong agreement with the theoretical solution of Huppert & Woods (1995). This comparison confirms the effectiveness of the COMSOL model in predicting porous media buoyancy-driven flow (without either drainage or dispersion). Second, we confirm that our COMSOL model predicts accurately the amount of dispersion experienced by a passive scalar by juxtaposing numerical model output with the classical solution of Bear (1972), section 10.6. This comparison confirms the effectiveness of the COMSOL model in predicting dispersion (without buoyancy effects). Finally, we compare numerical predictions against the flow patterns observed in similitude laboratory experiments of a filling box flow consisting of a leaky gravity current fed by a descending plume, i.e. figures 4 a,c of Sahu & Flynn (2017). This comparison confirms the effectiveness of the COMSOL model in predicting distributed drainage for flows driven by density differences.

3.4.4 Determination of the entertainment coefficient

Numerical simulations are run under two different mixing scenarios. For one, mixing details in the lower layer are resolved using (3.34) and (3.35), thereby offering the most realistic representation of the flow behavior expected in, say, a similitude laboratory experiment. For the other, we run numerical experiments that mimic the perfect mixing case of figure 3.2 and so eliminate dense fluid from the lower layer. This latter category of numerical experiment is run so that, by comparison with the analogue model of section 3.3, we may estimate the numerical value of the entrainment coefficient ε. The value so determined is assumed to apply to both of the perfect mixing and no mixing models, the latter of which is challenging to reproduce numerically. The primary difference between these models concerns, of course, mixing details from the lower layer; in turn, mixing experienced in the domain $z < -\xi$ seems very unlikely to directly influence mass transport between the bulk and dispersed phases of the gravity current and therefore the numerical value of the entrainment coefficient.

To make quantitative predictions with our theoretical models, we first have to estimate the value of the entrainment coefficient ε. To this end, and with specific reference to the perfect mixing case, the difference between the nose positions of the bulk and dispersed phases in the theoretical versus numerical models is specified by a time-integrated error $\overline{E}$, which is defined as

$$\overline{E} = \int_{t_1}^{t_2} \left[\left(\frac{x_{N_d} - x_{N_b}}{x_{N_d}} \right)_{\text{theory}} - \left(\frac{x_{N_d} - x_{N_b}}{x_{N_d}} \right)_{\text{num}} \right] \mathrm{d}t \,, \tag{3.39}$$

in which $\left(\frac{x_{N_d}-x_{N_b}}{x_{N_d}}\right)_{\text{theory}}$ is assessed from the theoretical model and $\left(\frac{x_{N_d}-x_{N_b}}{x_{N_d}}\right)_{\text{num}}$ is assessed from the numerical model. When post-processing the numerical data, we follow the approach suggested by Bharath *et al.* (2020) and define x_{N_b} (x_{N_d}) as the down-dip-most location where fluid having a density 80% (5%) of the source density can be found. Note also that we select $t_1 = 20$ (by which time the gravity current is indeed long and thin) and $t_2 = 200$ (by which time the gravity current has propagated a significant distance downstream). The ε that minimizes this time-integrated error is considered as the optimum value for the entrainment coefficient in the theoretical model.

For mathematical simplicity, the theoretical models of 3.3 assume a linear relationship between w_{ei} and u_i, where $i = 1, 2$. However, and consistent with the free shear flow study of Reeuwijk *et al.* (2019) and the porous media flow study of Sheikhi *et al.* (2023), we allow the entrainment coefficient to vary with the dip angle θ, and also with K_{eff}, defined as

$$K_{\text{eff}} = K\left(1 + \frac{1}{\xi}\right) . \tag{3.40}$$

K_{eff}, effective permeability, is motivated by the functional forms of (3.29) and (3.30), which demonstrate that the draining velocities depend directly on K and ξ^{-1}. In physical terms, K_{eff} characterizes the ease with which dense fluid may drain through the interbed layer. Resistance to draining may arise because K is relatively small or because ξ is relatively large (though not so large that the interbed thickness is large compared to a characteristic gravity current thickness); K_{eff} takes into account both of these considerations. Thus larger K_{eff} is associated with more draining and with a slower speed of advance for the gravity current. Corresponding data are summarized in figure 3.5. These results suggest that ε increases with both of θ and K_{eff}. In this way, our results, though consistent with the porous media flow investigation of Sheikhi *et al.* (2023), demonstrate an intriguing difference with Reeuwijk *et al.* (2019). Although they likewise determined that ε increases with θ, their investigation pertained to downslope, not upslope, flow. In other words, Reeuwijk *et al.* (2019) determined that the entrainment coefficient increases with the gravity current speed whereas porous media flows evidently exhibit the opposite behavior. This difference is likely related to the different entrainment mechanisms that apply for turbulent free shear flows versus porous media flows. In the former case, entrainment is a consequence of large-scale eddies, which entrain external ambient fluid via engulfment. Even for small θ, no such mechanism applies for the porous media flows of interest here, which remain laminar such that gravity current boundaries remain smooth. Graphical evidence for this last claim is presented in the following section.

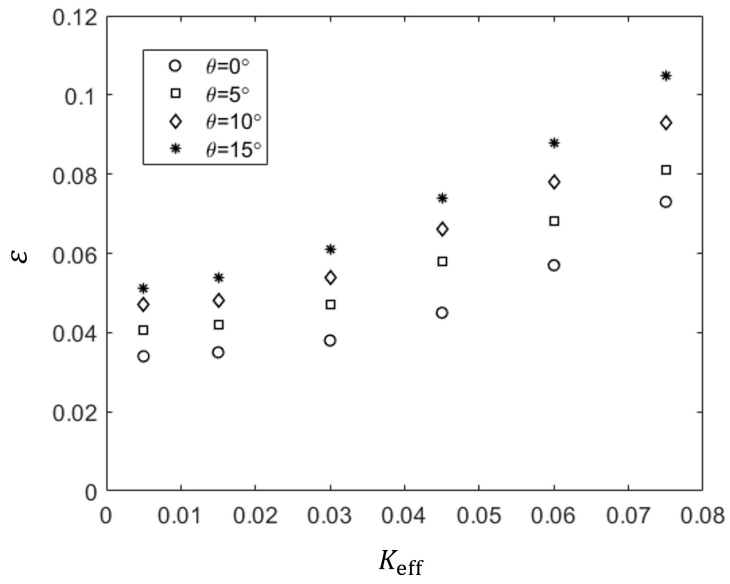

Figure 3.5: Error-minimizing value of ε versus θ and $K_{\text{eff}} = K\left(1 + \frac{1}{\xi}\right)$.

3.5 Results and discussion

3.5.1 Comparison of theoretical and numerical results

Figure 3.6 compares the numerical output against the theoretical predictions made by the perfect mixing and no mixing models. As anticipated, the numerical solution often lies between the two extremes of perfect (red curves) versus no mixing (black curves). Consistent with figure 3.3, the black and red curves very nearly overlap at early times but then diverge as t increases. By extension, and for both $\theta = 0°$ and $\theta = 5°$, there is a good qualitative agreement between the numerical data and the theoretical predictions for $t \lesssim 100$. For $t \gtrsim 100$, the perfect mixing model continues to provide reasonably accurate predictions for the shape and extent of the bulk and dispersed phases. On the other hand, the accuracy of the no mixing model suffers from its over-prediction of gravity current retraction. Additional discussion on this point is provided below.

Shown in figure 3.7 are the bulk (left-hand side panels) and the dispersed (right-hand side panels) nose positions for the two theoretical models. Also included in figure 3.7 are corresponding numerical data, which are indicated by the solid symbols. The no mixing model predicts a gradual

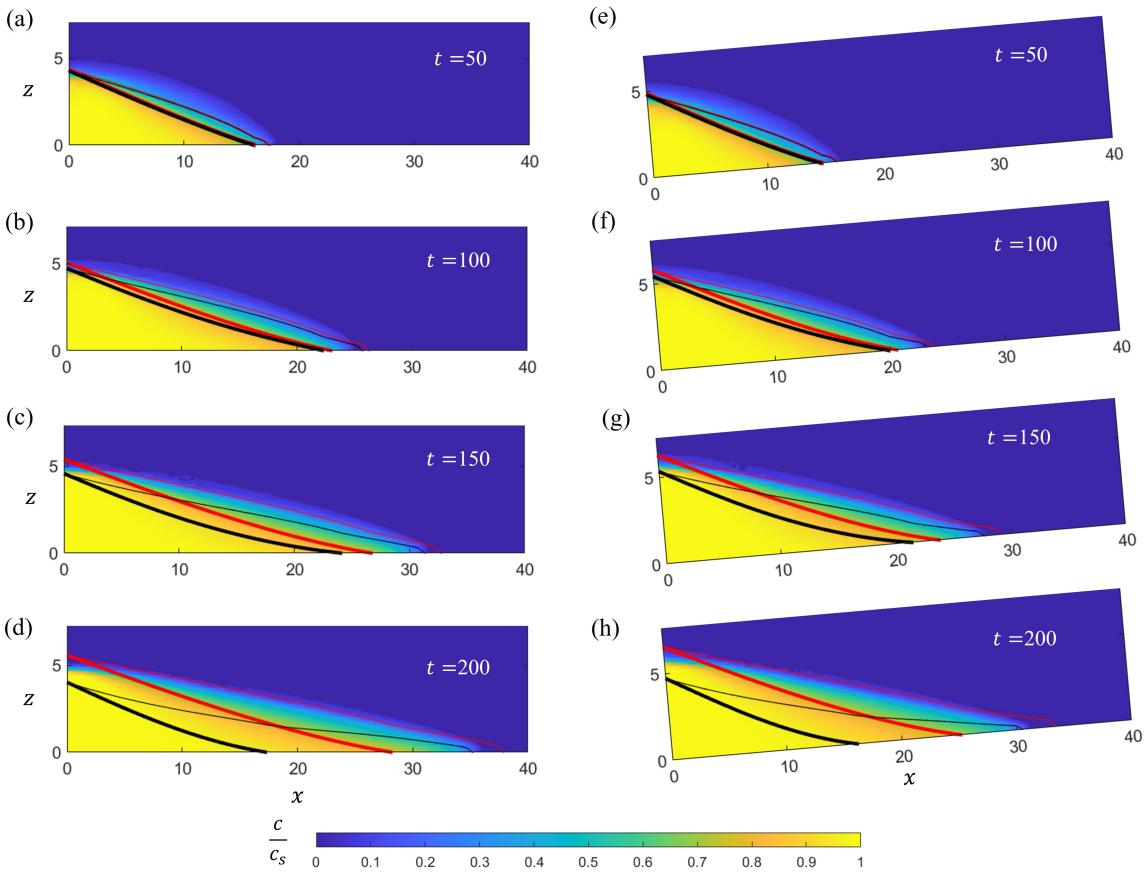

Figure 3.6: [colour] Numerical prediction of the gravity current profile versus the analogue theoretical predictions corresponding to perfect mixing (red curves) and no mixing (black curves). Thick lines indicate the bulk interface and thin lines indicate the dispersed interface. The color contours show the numerical output. (a-d) $\theta = 0°$ and (e-h) $\theta = 5°$. Here, $K = 0.0025$ and $\xi = 0.333$ which is equivalent to $K_{\text{eff}} = 0.01$.

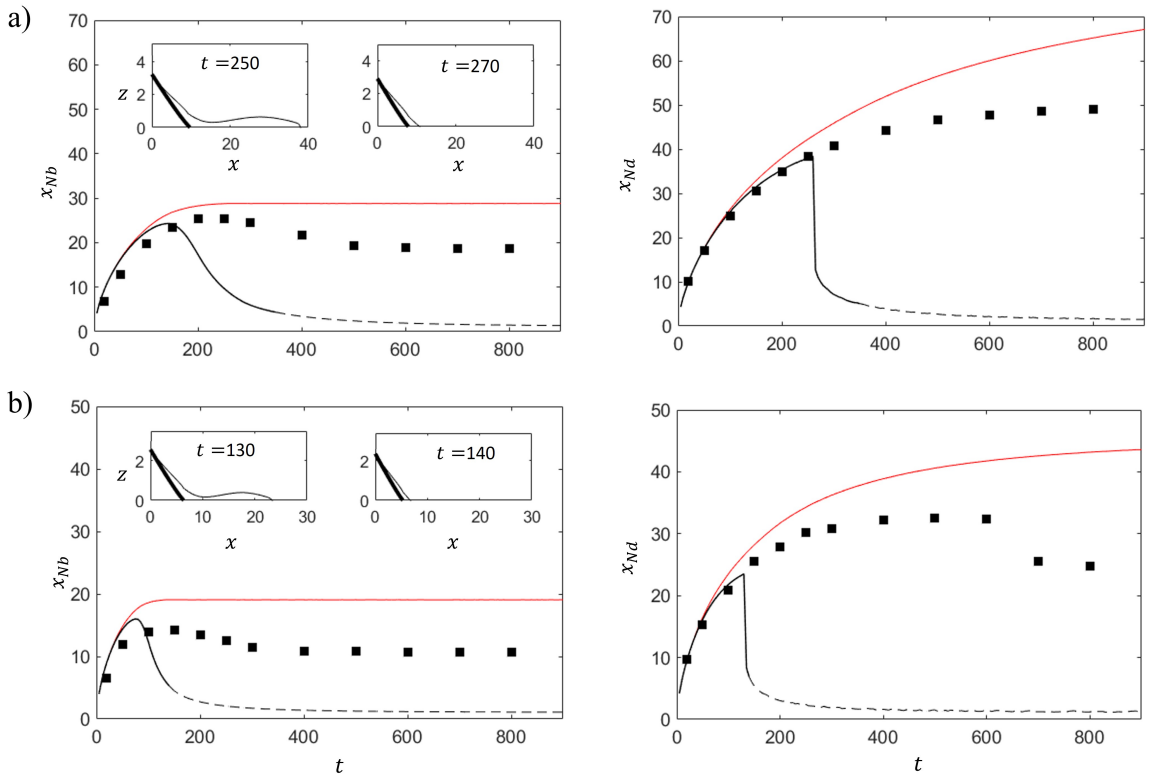

Figure 3.7: [colour] Time series of the bulk and dispersed nose positions for $\theta = 0°$ and (a) $K_{\text{eff}} = 0.01$ and (b) $K_{\text{eff}} = 0.02$. Numerical data are indicated by the square symbols; theoretical predictions are indicated by the red (perfect mixing) and black (no mixing) curves. The dashed black curves indicate the domain where the hydrostatic assumption becomes invalid in the no mixing model. The inset images show the bulk and dispersed interfaces before and after the sharp reduction in the position x_{N_d} of the dispersed nose for the no mixing case.

retraction in the bulk phase but an abrupt retraction in the dispersed phase. As the inset images in figure 3.7 make clear, the sudden retraction in the dispersed phase occurs because of a decrease in the thickness of the dispersed phase at its leading edge. The decrease in question causes a sudden vanishing of the thinned front. As the effective permeability, K_{eff}, increases, the drainage becomes more robust, and the equivalent drained depth, l, increases more quickly. The retraction, therefore, occurs earlier for larger K_{eff}. Beyond the onset of retraction, draining is so robust, and vertical velocities in the gravity current so large, that the assumption of a hydrostatic flow can no longer be justified. In figure 3.7, the (black) line type then changes from solid to dashed. Figure 3.7 confirms that the degree of gravity current retraction experienced in the numerical model, though non-zero, is small and time-delayed, much more so than is predicted by the no mixing model. So although the no mixing model gives predictions that are in reasonably good agreement with the numerical data up to the point of retraction, model fidelity suffers thereafter. Generally more favorable agreement is observed when considering the perfect mixing model, although the long-time limit is characterised by an over-prediction of the front positions for both the bulk and dispersed phases. Not surprisingly, deviations are seen to increase as draining is made more robust, i.e. as the value of K_{eff} increases.

The results of figure 3.7, in particular the observation concerning the eventual non-hydrostatic nature of the flow in the no mixing case, motivate us to divide the (t, K_{eff}) parameter space as in figure 3.8. The red region shows the regime before the onset of gravity current retraction in the no mixing model. In this red regime, we can use either theoretical model to predict, with reasonable accuracy, the forward advance of the bulk and dispersed phases. The green area shows the regime where the no mixing model becomes unduly influenced by its prediction of gravity current retraction. Here, the no mixing model generates results that are consistent with respect to the model assumptions but not, unfortunately, in good agreement with numerically-determined behavior. The severity of the retraction predicted by the no mixing model stems from its inability to account for the instabilities that develop within the lower layer draining fluid. We elaborate on this point in section 3.5.3. Thereafter, and in the blue region of figure 3.8, the flow predicted by the no mixing model becomes non-hydrostatic and the model violates one of the key assumptions

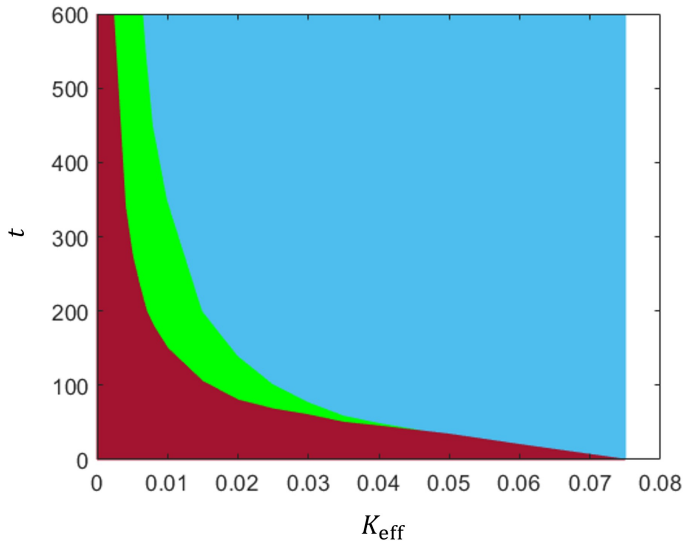

Figure 3.8: [colour] Theoretical model regime diagram illustrating the regimes where (i) both of the no mixing and perfect mixing models return accurate predictions [red], (ii) the no mixing model remains hydrostatic but is inaccurate owing to its over-prediction of gravity current retraction [green], (iii) the no mixing model is invalid [blue], and, (iv) both models become invalid [white]. Formally, data are shown for $\theta = 0°$; however, we find very similar results at different inclination angles.

stated in section 3.3. In this blue region, therefore, only the perfect mixing model is physically-acceptable. Finally, when K_{eff} exceeds approximately 0.075, corresponding to the white region in figure 3.8, the drainage velocity becomes so large that the hydrostatic assumption is violated even in the perfect mixing model. In this regime, most of the injectate immediately drains to the lower layer such that relatively little fluid remains above the permeability jump in the form of a distinct gravity current. Separate analyses (not shown) suggest that the regime diagram of figure 3.8 is insensitive to the choice of inclination angle. Accordingly, the results of figure 3.8 are presumed applicable for different θ.

3.5.2 Effects of K_{eff} and θ on dispersion

In this subsection, attention is restricted to the case where both theoretical models yield accurate predictions corresponding to the red region of figure 3.8. In this red region, we can employ the no mixing and perfect mixing models to quantify the impact on dispersion of two especially important

dimensionless parameters, namely K_{eff} and θ. To this end, we consider as dispersion metrics the separation distance between the bulk and the dispersed nose positions and the fraction of the total buoyancy (per unit width) that is specifically associated with the dispersed phase. As regards the latter parameter, and with respect to the thick and thin curves of figure 3.3, we first calculate

$$B_{\text{bulk}} = \int_0^{x_{N_b}} h_1 \, \mathrm{d}x \qquad \text{and} \qquad B_{\text{disp}} = \int_0^{x_{N_d}} c_2(h_2 - h_1) \, \mathrm{d}x \equiv \int_0^{x_{N_d}} b_2 \, \mathrm{d}x \, . \tag{3.41a,b}$$

The dispersed buoyancy fraction $\tilde{B}_{\text{disp}}$ is then found from

$$\tilde{B}_{\text{disp}} \;=\; \frac{B_{\text{disp}}}{B_{\text{bulk}} + B_{\text{disp}}} \, . \tag{3.42}$$

The sensitivity of dispersion to K_{eff} is explored in figure 3.9. Figure 3.9 a shows the nose separation, $1 - x_{N_b}/x_{N_d}$, whereas figure 3.9 b shows the dispersed buoyancy fraction, $\tilde{B}_{\text{disp}}$. In both panels, data are measured at $t = 150$. Increasing K_{eff} leads to more drainage of bulk fluid from the gravity current, which thereby retards the elongation of the bulk phase. Although increasing K_{eff} likewise increases the drainage of dispersed fluid, the effect is comparatively mild, so that the net effect of increasing the effective permeability is to increase both the nose position separation distance and also the dispersed buoyancy fraction. The trends in question are apparent from both of the no mixing (black curves) and perfect mixing (red curves) models and are also evident from the superposed numerical data (closed symbols). Consistent with figure 3.7, and for the relatively modest values of t of interest here, we find better agreement between the numerical data and the predictions of the no mixing model versus the perfect mixing model.

A complementary comparison but considering the impact of θ rather than K_{eff} is presented in figure 3.10. When the bottom boundary is inclined up-dip such that $\theta > 0°$, the gravity current characteristic velocity decreases. Hence entrainment to the dispersed phase, whether from the surroundings or from the bulk phase, is reduced. Therefore, both of $1 - x_{N_b}/x_{N_d}$ and $\tilde{B}_{\text{disp}}$ decrease with θ. Comparing figure 3.10 against figure 3.9 shows that dispersion intensity is more sensitive to K_{eff} than to θ, e.g. doubling the former parameter yields a bigger change in $1 - x_{N_b}/x_{N_d}$ and

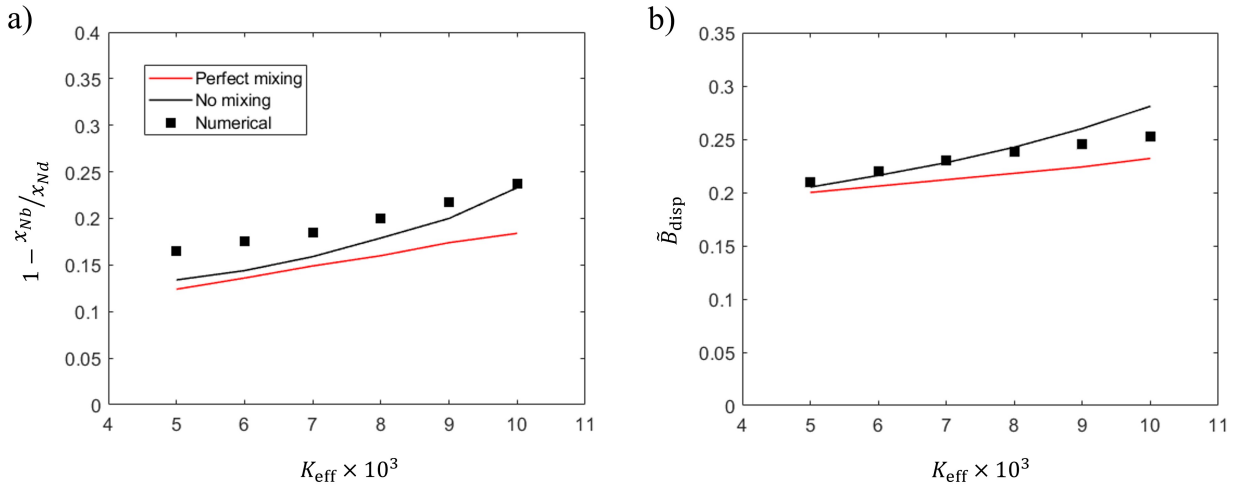

Figure 3.9: [colour] (a) Difference of nose separation and (b) buoyancy fraction in the dispersed phase for $\theta = 0°$ but various K_{eff} at $t = 150$.

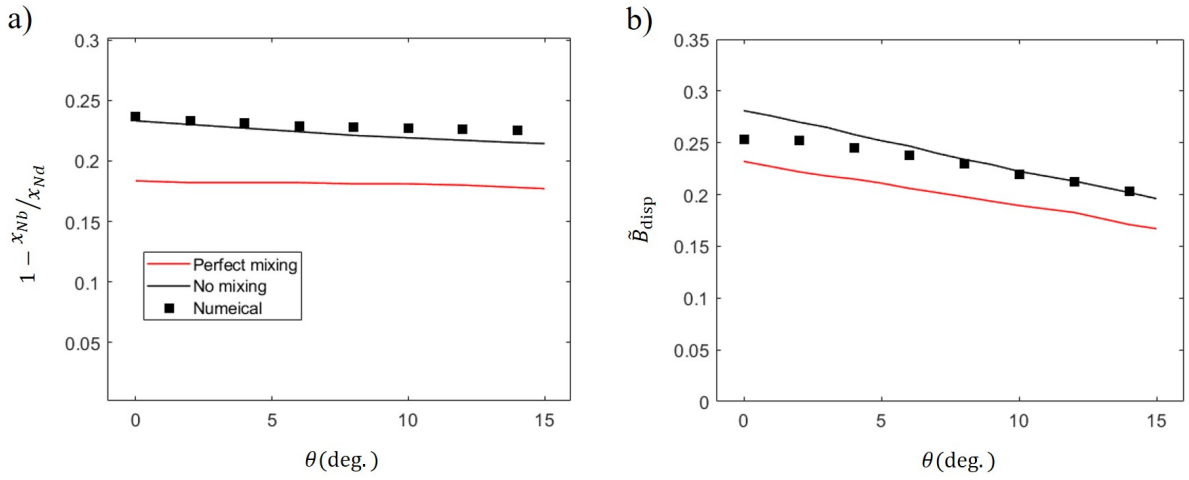

Figure 3.10: [colour] As in figure 3.9 but considering the influence of θ for $K_{\text{eff}} = 0.01$.

$\tilde{B}_{\text{disp}}$ than is realized by doubling the latter parameter. On the other hand, and as with figure 3.9, figure 3.10 confirms that output from the numerical simulations is better aligned with the no mixing model than with its perfect mixing counterpart.

3.5.3 Flow characterization past the point of theoretical model breakdown

Although the theoretical models of section 3.3 become inaccurate and/or invalid in the green and blue regions of figure 3.8, we can leverage the numerical results from the COMSOL simulations to investigate the flow behavior within these parameter spaces. These numerical simulations illustrate that following the elongation of both the bulk and dispersed phases, the bulk phase begins to retract, whereafter the dispersed phase begins to thin – see the top two panels of figure 3.11. The thin leading edge of the dispersed phase eventually disappears and the bulk and dispersed phases reach their respective terminal lengths. Qualitatively similar behavior is predicted by the no mixing model – see e.g. figure 3.7 – though in this theoretical case, transitions are more abrupt and the magnitude of the retraction is much larger.

Examination of the numerical data has a further benefit, namely that it allows us to study the details of the draining flow. To this end, figure 3.12 shows the convective flow patterns that develop in the lower layer for different K_{eff}. Figure 3.12 confirms that drainage is more severe for $0 \leq x < x_{N_b}$ than it is for $x_{N_b} \leq x \leq x_{N_d}$. Moreover, and consistent with Leahy *et al.* (2009) and Sahu & Neufeld (2023), this figure demonstrates the presence of fingers, which result from a Rayleigh-Taylor-type instability. The appearance of fingers is characterized by alternating bands of upward- versus downward-propagating fluid – see e.g. the solid red curve in the left-most panel of figure 3.12. Moreover, the bulbous shape of the largest finger from the second panel of figure 3.12 suggests an eventual separation of this draining fluid from the overlying gravity current. In either case, the situation differs significantly from the much more uniform scenario associated with the no mixing model, whereby the vertical velocities measured in the gravity current, the interbed layer and the lower layer are identical (and over-predicted). Note finally that as K_{eff} increases, fingers form earlier. With reference to figure 3.8, this explains why the time interval over which

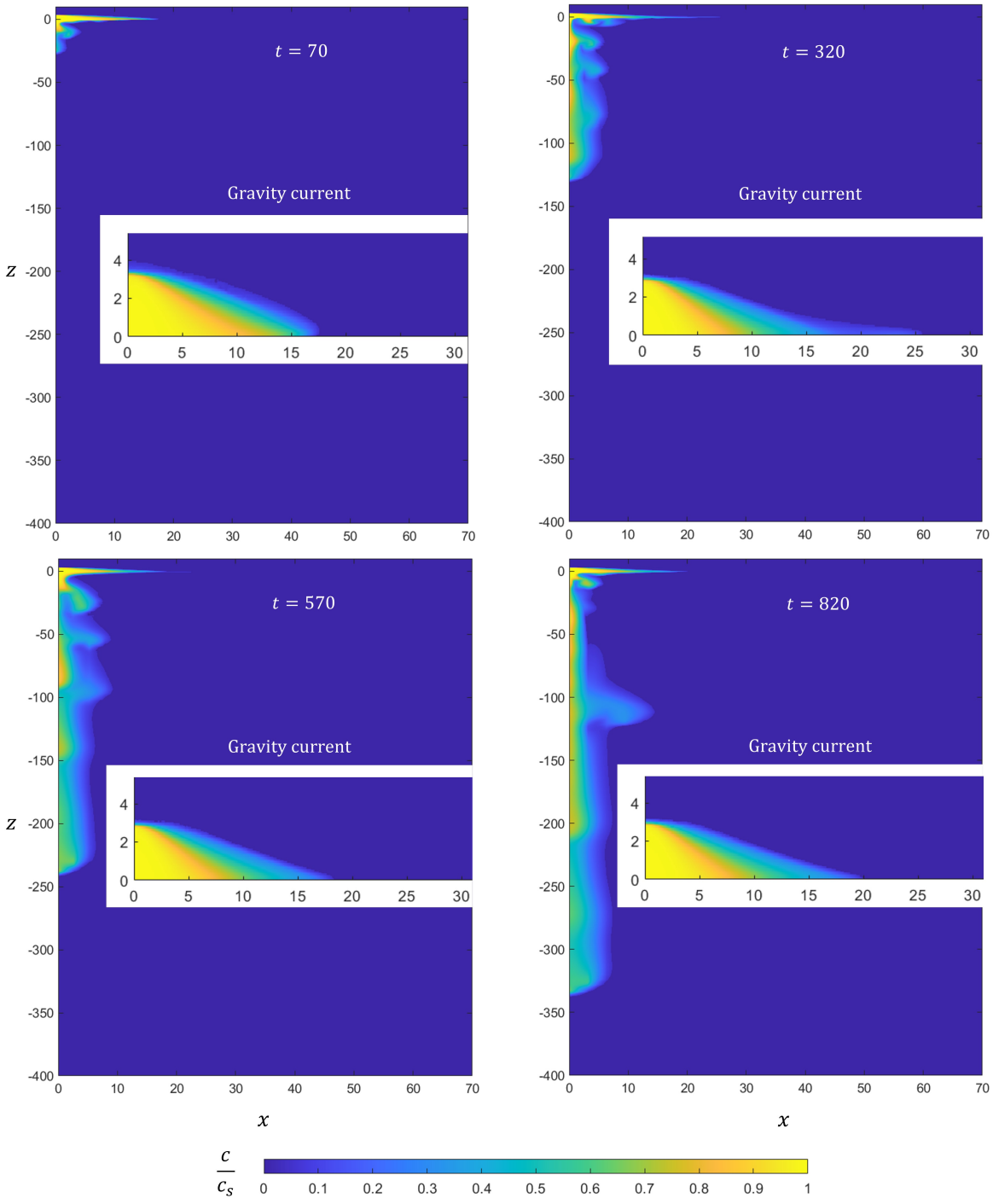

Figure 3.11: [colour] Numerical prediction of the flow in the green and blue regions of figure 3.8. Inset images show the gravity current profile in more detail. Here, $K_{\text{eff}} = 0.03$, $\theta = 0°$ and non-dimensional times are as indicated.

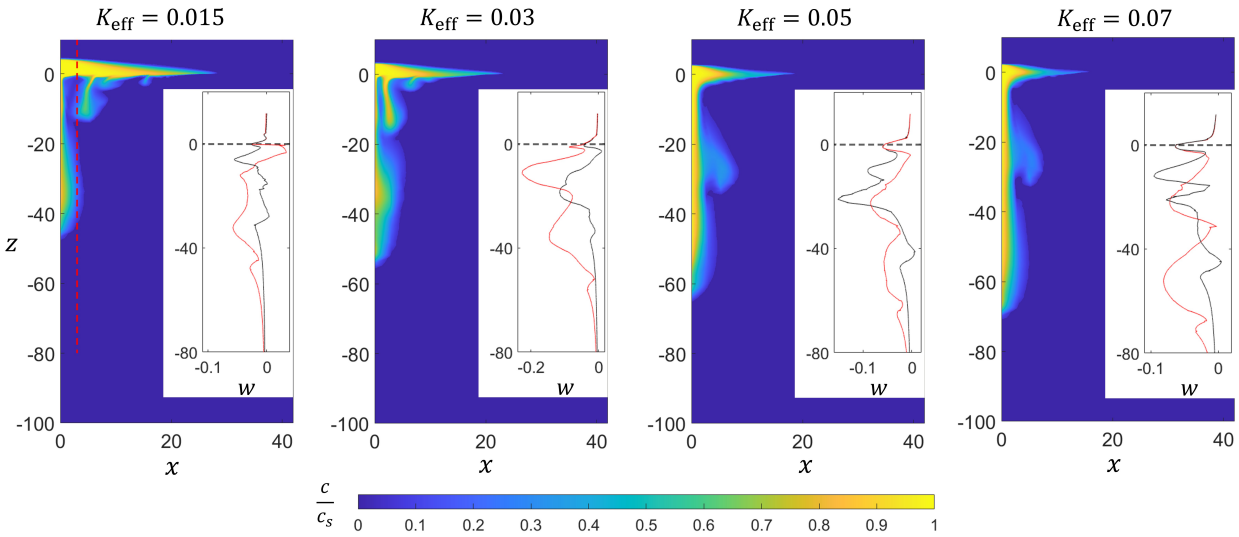

Figure 3.12: [colour] Numerical prediction of the gravity current and associated draining flow for different K_{eff} at $t = 150$ and with $\theta = 0°$. The inset images show the vertical variation of the vertical velocity, w. Curves are drawn for $t = 100$ (black lines) and $t = 150$ (red lines). The red dashed line from the left-most image displays the location $x = 3$ where vertical velocities are evaluated.

the theoretical models work well is tighter for larger K_{eff}.

To categorize mixing in the lower layer, we can extend the definition of $\tilde{B}_{\text{disp}}$ to the draining flow. Accordingly, we evaluate integrals similar to those of (3.41) but spanning a vertical domain $z < -\xi$. Thus do we suppose that $\tilde{B}_{\text{disp}}$ now represents the fraction of the drained fluid that appears in a dispersed rather than in a bulk phase. Numerical values for the redefined $\tilde{B}_{\text{disp}}$ are reported in table 3.1 for various K_{eff} and for two inclination angles, i.e. $\theta = 0°$ and $\theta = 5°$. Although there is some scatter in the data, particularly for the case of a horizontal permeability jump, the

Table 3.1: Lower layer dispersed buoyancy fraction at $t = 150$ for various K_{eff} and $\theta = 0°$ and $\theta = 5°$.

$\theta = 0°$		$\theta = 5°$	
K_{eff}	$\tilde{B}_{\text{disp}}$	K_{eff}	$\tilde{B}_{\text{disp}}$
0.015	0.80	0.015	0.83
0.03	0.85	0.03	0.68
0.05	0.65	0.05	0.59
0.07	0.77	0.07	0.60

results of table 3.1 support the conclusion that most of the drained fluid exists in a dispersed state, especially for small K_{eff}. This observation is helpful in the re-examination of figure 3.7 a, particularly over the time interval $200 \lesssim t \lesssim 350$. There, we find much better overall agreement between the numerical data and the perfect mixing model (red curve) than the no mixing model (black curve). The no mixing model fails to account for the dispersed (and disconnected) nature of the drained flow and so over-predicts both the influence of dense fluid from the lower layer and the severity of gravity current retraction. This limitation is obviously avoided by the perfect mixing model, which neglects any contribution of the drained flow when calculating the draining velocity. The perfect mixing model thereby provides a more accurate (though still imperfect) prediction for the distances traveled by each of the bulk and dispersed phases.

3.6 Summary and conclusions

The present analysis considers, theoretically and numerically, the flow of a porous media gravity current along an interbed layer where drainage from the gravity current underside is spatially-distributed. The theoretical model of section 3.3 includes dispersive mixing and separates the gravity current into bulk and dispersed phases. The latter phase entrains fluid from the former and also from the surrounding ambient. For expediency, we adopt a somewhat simpler approach when considering the evolution of the fluid that drains into the lower layer of the porous medium. Thus do we restrict attention to the two bookend opposite cases of no mixing versus perfect mixing. The non-dimensional governing equations presented in section 3.3 make reference to two dimensionless parameters namely K_{eff}, the effective permeability defined by (3.40), and θ, the inclination angle of the interbed layer. Increasing K_{eff} by either increasing the permeability of the interbed layer or else decreasing its thickness intensifies drainage from both the bulk and the dispersed phases. Given that drainage is notably more severe in the bulk phase, increasing K_{eff} (i) yields a larger separation between the bulk and dispersed nose positions, and, (ii) causes a greater fraction of the gravity current fluid to reside in the dispersed phase. By either metric, we conclude that dispersion is more significant. Increasing θ, so that the gravity current flows up a steeper incline, leads to a smaller

velocity of advance and therefore to less dispersion. Our analysis (see e.g. figure 3.8) suggests that, consistent with Sahu & Neufeld (2023), the hydrostatic pressure assumption becomes invalid when K_{eff} and t are large. The no mixing and perfect mixing models do not, therefore, provide meaningful predictions always. In particular, the no mixing model eventually predicts a draining velocity that is too large and so exhibits a more limited range of applicability than its perfect mixing counterpart.

To gain additional insights into the veracity of our model predictions, we ran a series of complementary COMSOL numerical simulations as described in section 3.4. In the first case, numerical data are needed to calibrate the value of the entrainment coefficient, ε, that appears in the governing equations (3.21)-(3.23). Figure 3.5 demonstrates that the optimum value of ε is a function of K_{eff} and θ. (Note that we consider the same value for ε for both of the no mixing and perfect mixing models because the entrainment coefficient depends on the details of the dispersive mixing that occurs between the gravity current and the ambient, but not on mixing processes in the lower layer.) In the second case, numerical simulations are performed for the sake of comparison with theoretical model output. Not surprisingly, the numerical simulations require approximately 30 times the number of floating point operations given e.g. the simplifying assumptions applied in the theoretical model. Figures such as 3.6, 3.7, 3.9 and 3.10 confirm that both theoretical models provide a reasonable description of the gravity current evolution, at least until the point where the no mixing model predicts flow retraction. Thereafter, the front positions anticipated by the no (perfect) mixing model significantly under-predict (moderately over-predict) the numerically-derived behavior. The eventual breakdown of the no mixing model cannot be regarded as surprising: the model assumes that fluid drained to the lower layer contributes to basal draining in perpetuity. This picture is rather different from the numerical simulation results of figure 3.12, which suggest the appearance of convective fingers that both mix into the lower layer ambient and later detach from gravity current underside. Fingers are the result of a Rayleigh-Taylor-type instability, are characterized by adjacent bands of upwards- versus downwards-directed flow and materialize earlier on for larger K_{eff}. On the other hand, and for smaller K_{eff}, we observe that a greater fraction of the draining fluid in the lower layer appears in a dispersed rather than bulk phase – see e.g. table

3.1. This is, of course, the opposite behavior to what is observed in the upper layer. In other words, large K_{eff} is associated with robust dispersion above the interbed layer but comparatively modest dispersion below. Meanwhile, small K_{eff} is associated with more modest dispersion above the interbed layer but more robust dispersion below. These observations suggest that theoretical models that consider sharp interfaces for the gravity current and also for the draining fluid may apply only under special circumstances e.g. at relatively early times before finger onset.

Although we have presented a careful comparison of theory and numerical simulation, it remains to confirm independently the accuracy of both categories of models with similitude laboratory experiments. To this end, we envision running a series of experiments in the spirit of Huppert *et al.* (2013), Bharath *et al.* (2020) and Sahu & Neufeld (2023). In such a case, the interbed layer may be included by application of a thin porous substrate as in the experiments of Thomas *et al.* (1998). Laboratory experiments must employ a lower layer of large depth so as to avoid the collision of the draining fluid with the bottom boundary of the tank. If such a collision were to occur, then a secondary gravity current would appear, which has the potential to influence the evolution of the gravity current propagating along the interbed layer – see e.g. Bharath & Flynn (2021). Turning from the laboratory to the field, it is important to reiterate that our research is motivated by examples of environmental flows in geological layers. These are more complicated than the physical domain that we consider here owing, for instance, to the more complicated pattern of layer heterogeneities than is accounted for in figure 3.1. In the next step, it would be beneficial to include multiple interbed layers, as has been done in the studies of Neufeld & Huppert (2009), Behnam *et al.* (2021) and Sahu & Neufeld (2023), for example. By doing so, we can better understand buoyancy-driven flow through non-uniform porous media, e.g. the communication of H_2 between different layers in underground hydrogen storage (UHS) projects involving depleted natural gas reservoirs. Our models also consider that the dynamic viscosity, μ, is independent of the concentration and is therefore the same in the bulk and dispersed phases. For the UHS example described in the Introduction, the viscosity of the dispersed phase (consisting of a mixture of H_2 and CH_4) should be more than that of the bulk phase (consisting of H_2). Underestimating the dispersed phase viscosity leads to over-predicting its propagation speed. Relative to real geological

flows, the models presented here might therefore over-predict the extent of dispersion. Quantifying this effect more precisely is a topic of current interest; to this end, we hope to report on our findings in a future publication.

Chapter 4

Can a hydrodynamic model predict the flow evolution of a hydrogen plume in a depleted natural gas reservoir? [1]

4.1 Abstract

Hydrogen storage in depleted natural gas reservoirs is a promising solution for storing excess renewable energy on a timescale longer than can be accommodated by salt cavern storage. However, commercial exploitation of the technology in question awaits the resolution of key challenges and uncertainties. Chief among these from a fluid mechanics point of view is to resolve the connection between hydrogen leakage and the mixing of hydrogen and cushion gas. Reduced-order-models examining this question have been developed i.e. by Sheikhi & Flynn (*J. Fluid Mech.*, vol. 984, A33, 2024), however their work relies much more heavily on fluid mechanics than it does on thermodynamics. It is therefore unclear the extent to which their model predictions are accurate when compared with e.g. the numerical output from reservoir-level simulation packages. Addressing this knowledge gap is the key focus of the present study. To this end, we use OpenGoSim and CMG to numerically resolve hydrogen injection directly below an interbed layer of reduced, but still finite,

[1] Sheikhi. S. & Flynn, M. R. 2024 Can a hydrodynamic model predict the flow evolution of a hydrogen plume in a depleted natural gas reservoir? *Int. J. of Hydrogen Energy*, **Submitted**.

permeability. The resulting comparison demonstrates that the theoretical model predicts, with generally good accuracy, the overall shape of the gravity current plus the amount of hydrogen that dispersively mixes into the surrounding cushion gas. However, reduced-order-model fidelity suffers when the injection time is long, the draining layer is thin and the interbed layer admits a relatively large drainage. This observation highlights areas of future improvement for the reduced-order-model, which can otherwise be applied, with great computational efficiency, in screening candidate reservoirs for hydrogen storage.

4.2 Introduction

As developed and developing economies strive to reduce their dependence on conventional fossil fuels, it is crucial to adopt sustainable alternatives that can minimize the environmental impact associated with traditional energy sources (Dincer, 2000). Because renewable energies, e.g. wind and solar, have emerged as promising surrogates in the energy transition, (green) hydrogen produced from the electricity derived from wind and solar is expected to play a crucial role in shaping the future energy landscape. However, before green hydrogen can displace either of blue or grey hydrogen, effective large-scale storage solutions must be developed (Muthukumar *et al.*, 2023; Hassan *et al.*, 2023; Abdellatif *et al.*, 2023; Verma *et al.*, 2024). Only then can the green hydrogen produced in summer, when solar radiation is plentiful, can be combusted in winter, when such radiation is less abundant. To this end, there is now much interest in underground hydrogen storage (UHS) in which hydrogen is first injected into, then withdrawn from, geological formations (Crotogino *et al.*, 2010; Tarkowski, 2019; Zivar *et al.*, 2021; Song *et al.*, 2023; Salmachi *et al.*, 2024). Among underground formations, depleted natural gas reservoirs are perhaps best suited for seasonal storage. Depleted natural gas reservoirs offer storage capacities in the terawatt-hour range and so surpass the amount of energy that can be stored in salt caverns by several orders of magnitude (Tarkowski, 2019; Alinejad *et al.*, 2024). Moreover, depleted gas reservoirs are believed to be better storage vehicles than either of depleted oil reservoirs or saline aquifers. Hydrogen storage in either of these latter formations includes a greater likelihood of hydrogen dissolution and/or chemical reactions

involving hydrogen. As with the leakage and dispersion mechanisms to be explored below, dissolution and chemical reaction represent an irreversible, and undesirable, loss of injectate (Tarkowski, 2019).

The feasibility of UHS in depleted gas reservoirs has been categorized in various studies (Amid *et al.*, 2016; Huang *et al.*, 2023). No small number of these studies have explored the impact of the cushion gas, i.e. the in-situ gas that maintains operational pressures downhole. Cushion gas composition is a key consideration to any UHS project because, for example, different cushion gases have different densities and are therefore associated with different likelihoods for the "gravity override" of the hydrogen plume (Hassanpouryouzband *et al.*, 2021). Moreover, different cushion gases impact the reservoir pressure in different ways. For instance, the numerical simulations conduted by Zamehrian & Sedaee (2022) reveal that hydrogen recovery is maximized when N_2 is employed as the cushion gas: injecting N_2 results in a greater increase of reservoir pressure compared to CO_2 or CH_4. In the current context, larger pressures are desirable because they are associated e.g. with greater water displacement, a job that would otherwise have to be performed by the hydrogen injected into (then subsequently retained within) the formation.

Other studies, have focused on the possible mixing of injected hydrogen with the cushion gas, the extent of this mixing having been identified by Amid *et al.* (2016) as a key knowledge gap. To this end, quantitative insights are contributed by Sari & Çiftçi (2024), who numerically modeled hydrogen injection/withdrawal from an onshore depleted gas reservoir, namely the Değirmenköy gas field, in Turkey. They used MRST (the MATLAB Reservoir Simulation Toolbox) and documented instances of significant mixing between the hydrogen and ambient reservoir fluid. Consistent with the earlier numerical studies of Pfeiffer & Bauer (2015) and Feldmann *et al.* (2016), Sari & Çiftçi (2024) showed that the ratio of the withdrawn hydrogen increases with the number of storage cycles. By the time of the fifth and final cycle, the recovery ratio (volume ratio of hydrogen injected vs. hydrogen produced) reaches approximately 92%. Complementing Sari & Çiftçi's study, Hagemann (2017) modeled numerically and theoretically UHS in depleted gas reservoirs and found that predictions of mixing efficiencies increase significantly when mechanical dispersion is taken into account. Thus when mechanical dispersion is included, the volume of hydrogen that can be

recovered economically decreases by 15% (Hagemann, 2017). Heterogeneity increases mechanical dispersion because the associated random grain orientation provides different pathways for fluid flow (Wang *et al.*, 2022). In a related spirit, Cai *et al.* (2022) conducted numerical simulations of UHS in an aquifer, a salt cavern and a depleted natural gas reservoir. The authors demonstrated that the purity of the produced hydrogen decreases in the reservoir case when the formation is heterogeneous. Feldmann *et al.* (2016) investigated hydrogen migration within a heterogeneous porous medium. This medium was characterized by the presence of sandstone layers interspersed with semi-permeable clay interbed layers. Their results show that hydrogen drainage through low permeable layers in conjunction with cushion gas dispersion decrease the hydrogen recovery ratio.

The above discussion suggests that the hydrodynamic behaviour of hydrogen (e.g. the "slippery" nature inherited from its small size at the atomic scale) coupled with formation heterogeneities make it difficult to model the precise details of hydrogen migration. Accordingly, simplified conceptual models are required to provide insights into the important factors, i.e. mixing and drainage, that influence the porous media flows relevant to UHS projects. Key to such descriptions is the realization that hydrogen is much more buoyant than any candidate cushion gas (unless, of course, hydrogen is itself used as the cushion gas). Hydrogen injected into formation will therefore rise vertically as an ascending plume, at least until the point where it strikes a cap rock layer. Thereafter, the primary flow will be orientated in a direction parallel to this impermeable or mostly-impermeable boundary. A theoretical study of mixing process within vertical porous media plumes is given in Sahu & Flynn (2015) and Gilmore *et al.* (2021) . Meanwhile, Sheikhi *et al.* (2023) and Sheikhi & Flynn (2024) presented simplified (e.g. hydrostatic) theoretical models for dispersive mixing in porous media gravity currents. The former of these studies developed a theoretical model to identify those most influential parameters that control dispersive mixing in porous media gravity currents experiencing localized drainage. Theoretical predictions were validated using COMSOL-based numerical simulations. This line of inquiry was extended by the latter of the two studies, which examined distributed drainage through a semi-permeable interbed layer rather than localized drainage through a fractured (but otherwise impermeable) interbed layer.

The studies of Sheikhi *et al.* (2023) and Sheikhi & Flynn (2024) are notable in that their theo-

retical models emphasize hydrodynamics at the expense of thermodynamics. Thus do the authors employ a linear equation of state in addition to numerous other simplifying assumptions. These include incompressible flow, concentration-independent dynamic viscosities and linear entrainment laws. So although the theoretical models in question exhibit encouraging quantitative agreement with the output of similitude numerical simulations, it is unclear whether these models offer meaningful insights in the context of real UHS-type flows. The primary focus of this work is to address this uncertainty and we do so by contrasting theoretical predictions with the output of OpenGoSim- and CMG-based numerical simulations that consider reservoir-appropriate (rather than similitude) conditions plus concentration-dependent viscosities, etc. In turn, theoretical predictions are derived from the work of Sheikhi & Flynn (2024), distributed drainage being of greater interest than localized drainage in the context of UHS in a depleted gas reservoir (Bunch *et al.*, 2024). Through the resulting comparison, we will demonstrate that the hydrodynamic model of Sheikhi & Flynn (2024) performs surprisingly well, at least insofar as its ability to predict (i) the lateral spread of hydrogen along the underside of the interbed layer, and, (ii) the volume of hydrogen that mixes into the cushion gas. These observations are significant in the UHS context because they suggest that preliminary assessments of hydrogen flow/mixing can be performed using reduced-order models that emphasize hydrodynamics but that sidestep many of the other complications (and runtime overhead) of more comprehensive numerical simulations.

The rest of this Chapter is organized as follows: in section 4.3, we present the details of OpenGoSim- and CMG-based numerical simulations. Meanwhile, key details associated with Sheikhi & Flynn (2024)'s theoretical model are given in section 4.4. Model output comparison is saved for section 4.5 and conclusions are then presented in section 4.6.

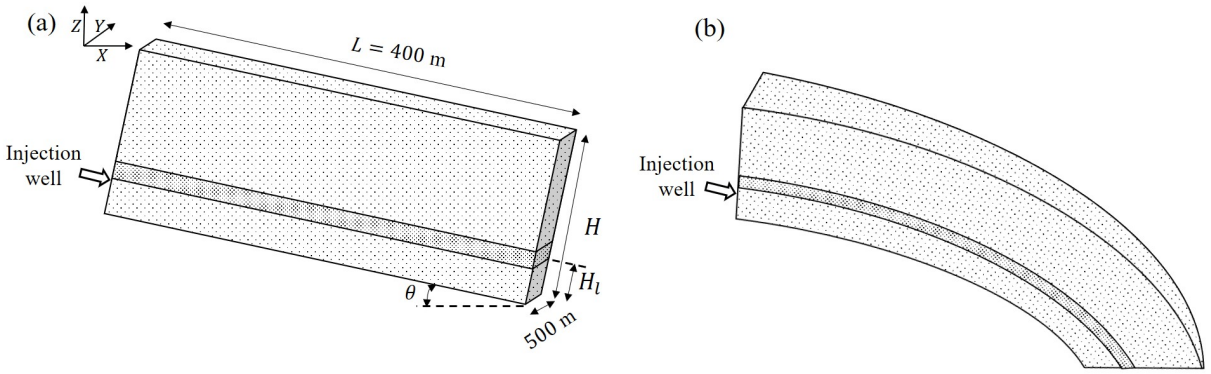

Figure 4.1: Schematic of the numerical domains. (a) Planar geometry, (b) curved (i.e. one-half of an anticline-like) geometry. Note that the scale of the domain is not identical in all directions. The dark stripe indicates the interbed layer. The interbed thickness varies between 1 m and 1.5 m in different simulations. The domain height H and lower layer height H_l are, respectively, 150 m and 38 m for unconfined domains and 50 m and 23 m for confined domains.

4.3 Numerical simulations

4.3.1 Formulation

The numerical domain consists of a homogeneous reservoir, except for the inclusion of a thin interbed layer. Most of the domain is saturated with a mixture of methane, carbon dioxide and nitrogen. The precise composition of this (cushion) gas is as follows: 93.95 mole% methane, 1.53 mole% carbon dioxide and 4.52 mole% nitrogen. The domain measures 800 m long × 500 m wide × 150 (or 50) m tall – see figure 4.1. The thickness of the interbed layer depends on the particular simulation but varies between 1 m and 1.5 m. The permeability and porosity of the upper and lower layers measure 100 mD and 0.2, respectively. These values are appropriate to a medium grained sandstone (Iscan & Kok, 2009). The interbed layer likewise has a porosity of 0.2 but its permeability is much smaller, i.e. we consider a minimum (layer-uniform) permeability of 0.35 mD and a maximum (layer-uniform) permeability of 1.0 mD, which is relevant to different varieties of hydrate-bearing clay (Zhang *et al.*, 2022). Note finally that saturating liquid water is included to a depth of 10 m from the lowest point of the domain. Any water appearing outside of this region of water saturation is considered as irreducible water corresponding to the endpoint saturation of the aqueous phase after extensive displacement by the gas phase – see figure 4.2. Accordingly, and

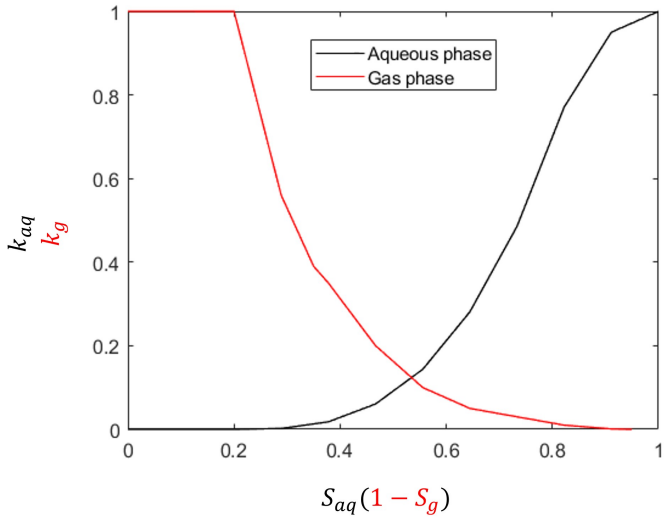

Figure 4.2: [Colour] Relative permeability of the aqueous and gas phase based on saturation. Note that for irreducible water (i.e. $S_g \leq 0.2$), the relative permeability of the gas phase remains unchanged. This is because the irreducible water resides small pore spaces that do not contribute to the overall flow (Ahmed, 2010).

whether we examine the upper, lower or interbed layer outside of the 10 m deep pool of saturating liquid water, the gas phase relative permeability (k_g) is unity (Ahmed, 2010) and the aqueous phase relative permeability (k_{aq}) is zero. This aligns with the concept of immobile irreducible water. Our approach is therefore also consistent with the theoretical model of Sheikhi & Flynn (2024), which ignores capillary effects. As suggested by the information given in the caption to figure 4.1, the lower layer thickness is always larger than 10 m such that the interbed layer does not intersect the water-saturated region within the horizontal domain of interest. This applies even to the anticline case of figure 4.1 (b) for which the region of water saturation remains well-separated from the hydrogen plume.

Hydrogen is injected at a rate of $Q_{\text{in}} = 2 \times 10^5$ S m^3/day from a horizontal well situated immediately below the interbed layer and spanning the formation width. At the source, the flow rate is therefore uniform in y, the spatial direction indicated in figure 4.1. The maximum Bottom Hole Pressure Limit (BHPL) measures 50 Bar above the original formation pressure whose value typically measures $P_{\text{form}} = 100$ bar. By applying mass balance for all three components (hydrogen,

cushion gas and water) (Chen *et al.*, 2006), we find that

$$\frac{\partial}{\partial t}\big(\phi\, x_g^{\mathrm{H_2}}\, S_g\, \eta_g\big) + \nabla.\big(x_g^{\mathrm{H_2}}\, u_g\, \eta_g + \phi\, S_g\, D_g\, \eta_g\, \nabla x_g^{\mathrm{H_2}}\big) = Q_{\mathrm{in}}\, \delta(X, Z - Z_{\mathrm{well}})\,, \tag{4.1}$$

$$\frac{\partial}{\partial t}\big(\phi\, x_g^{\mathrm{c}}\, S_g\, \eta_g\big) + \nabla.\big(x_g^{\mathrm{c}}\, u_g\, \eta_g + \phi\, S_g\, D_g\, \eta_g\, \nabla x_g^{\mathrm{c}}\big) = 0\,, \tag{4.2}$$

$$\frac{\partial}{\partial t}\big(\phi\, S_{aq}\, \eta_{aq}\big) + \nabla.\big(u_{aq}\, \eta_{aq}\big) = 0\,. \tag{4.3}$$

Here, ϕ is the porosity and x_β^α is the mole fraction of component α (hydrogen, H_2 or cushion gas, c) in phase β (gas, g or aqueous, aq). Meanwhile, S_β, u_β and η_β are, respectively, the saturation, Darcy velocity and molar density of phase β. Finally, D_g is the gas phase dispersion coefficient, δ is the Dirac delta function and Z_{well} is the Z-position of the well. Equations (4.1-4.3) do not include dissolution of either of the cushion gas or hydrogen gas in the aqueous phase because the associated Henry's law constants are relatively small (Huang *et al.*, 2023). In a similar spirit, we discount the contribution of water vapor in either gas phase owing to the large formation pressure. Finally, we neglect the capillary pressure at the gas-aqueous interface in the deep water layer that appears below the gas phase and so assume the following equality of pressures $P_{aq} = P_g = P$. In other words, and in the large Bond number limit of interest here, the capillary pressure is insignificant due to the interfacial tension between water and hydrogen (Muhammed *et al.*, 2023). Given the above assumptions, the Darcy's law expressions for the aqueous and gas phases read as follows

$$u_g = \frac{k\, k_g}{\mu_g} \nabla\big(P - \rho_g\, g\, Z\big)\,, \tag{4.4}$$

$$u_{aq} = \frac{k\, k_{aq}}{\mu_{aq}} \nabla\big(P - \rho_{aq}\, g\, Z\big)\,, \tag{4.5}$$

in which k is the medium permeability, g is gravitational acceleration and k_β, μ_β and ρ_β are the relative permeability, dynamic viscosity and density of phase β, respectively. Equations (4.1-4.5) are solved separately in the upper, lower and interbed layers, the only substantial difference between these being the small thickness and permeability associated with the latter layer.

Equations (4.1-4.5) are complemented by an energy balance equation that reads

$$\frac{\partial}{\partial t}\Big[\phi\big(S_g\,\eta_g\,U_g + S_{aq}\,\eta_{aq}\,U_{aq}\big) + (1-\phi)\rho_r\,c_r\,T\Big] + \nabla.\big(u_g\,\eta_g\,H_g + u_{aq}\,\eta_{aq}\,H_{aq} + \kappa\,\nabla T\big) = 0\,. \quad (4.6)$$

Here, T is temperature, U_β is the internal energy of phase β and H_β is the hydrostatic pressure head of phase β. Meanwhile, κ is the rock thermal conductivity, ρ_r is the rock density and c_r is the rock specific heat capacity. Upon substituting (4.4) and (4.5) into (4.1-4.3), we are left with four equations in the six unknowns S_g, S_{aq}, $x_g^{\mathrm{H_2}}$, x_g^{c}, P and T. Closure is realized by recognizing that

$$S_g + S_{aq} = 1\,, \quad (4.7)$$

and

$$x_g^{\mathrm{H_2}} + x_g^{\mathrm{c}} = 1\,. \quad (4.8)$$

The resulting system of coupled equations can be solved using a variety of commercial software platforms. In the following two subsections, we outline how we deployed two particular packages, namely OpenGoSim and CMG. In either case, we consider the same initial conditions, namely a domain devoid of hydrogen and in hydrostatic balance where the top of the domain is at a depth of 3550 m. Except as specified below, this depth is associated with a pressure of 100 bar. Moreover, we consider an initial temperature of 75°C. All boundaries are considered impermeable.

The numerical models are verified in three complementary ways. First, we compare the numerical simulations from two distinct programs, recognizing that OpenGoSim utilizes a finite volume method whereas CMG applies a finite difference method. Second, we confirm that our simulations are grid independent. Finally, we confirm that the numerical model predicts a systematic change in output parameters in response to variations in input variables – see figure 4.7 below and Appendix C.1.2.

4.3.2 OpenGoSim

The COMP3 multi-gas component mode (gas/solvent/water) of OpenGoSim-1.8 is used to solve the governing equations of subsection 4.3.1. Having specified the reservoir temperature and pressure, cushion gas and hydrogen densities are determined via the Peng-Robinson equation of state (Peng & Robinson, 1976). Meanwhile cushion gas and hydrogen viscosities are obtained via the Lorenhz-Bray-Clay method (Lohrenz *et al.*, 1964) and a residual entropy method (Mairhofer, 2021) respectively. Consistent with the value reported in Feldmann *et al.* (2016), the gas phase dispersion coefficient, D_g, is 2×10^{-5} m^2/s. Finally, (4.1-4.3) and (4.6-4.8) are discretized in space using a finite volume scheme based on the two-point flux formula, and in time using a first order fully implicit scheme. The Newton-Raphson approach is used to linearize the discretized equations. This linear system is preconditioned and solved iteratively via the GMRES method.

4.3.3 CMG

When applying CMG 2021.10 to solve the governing equations of subsection 4.3.1, (4.1-4.3) and (4.6-4.8) are discretized using the finite difference method and solved implicitly using the GEM solver. We use higher order upstream weighting schemes under a Total Variation Diminishing (TVD) flux limiter to control the numerical diffusion in the solution (Shrivastava *et al.*, 2005). The reservoir initialization is similar to OpenGOSim. Hydrogen and cushion gas properties are calculated using WINPROP. The gases viscosity is calculated from the Jossi, Stiel and Thodos correlation (Reid *et al.*, 1959). Within CMG, the gas phase dispersion coefficient is represented as a tensor of the form

$$D_g = \begin{bmatrix} D_{g,xx} & D_{g,xy} & D_{g,xz} \\ D_{g,yx} & D_{g,yy} & D_{g,yz} \\ D_{g,zx} & D_{g,zy} & D_{g,zz} \end{bmatrix}. \tag{4.9}$$

Diagonal ($D_{g,mm}$) and non-diagonal ($D_{g,mn}$) terms of the above tensor (4.9) are given by

$$D_{g,mm} = \frac{D_g^*}{\phi\, F_g\, S_g} + \frac{a_L - a_T}{\phi\, S_g\, |u_g|}\, u_{g,m}^2 + a_T\, \frac{|u_g|}{\phi\, S_g}\,, \tag{4.10a}$$

$$D_{g,mn} = \frac{a_L - a_T}{\phi\, S_g\, |u_g|}\, u_{g,m}\, u_{g,n}\,. \tag{4.10b}$$

Here, F_g is the gas phase formation resistivity factor and D_g^* is the gas phase effective molecular diffusion coefficient. D_g^* is related to the standard molecular diffusion, D_g^{mol}, except that it incorporates effects related to the porosity, saturation state, pressure, temperature, and tortuosity of the porous medium (Poling *et al.*, 2001). Based on Michelsen *et al.* (2023), D_g^* is taken to be 10^{-7} m^2/s in this study. Equations (4.10) also make reference to the longitudinal dispersivity, a_L, and the transverse dispersivity, a_T. Dispersivities are scale-dependent and are influenced by pressure, temperature, flow velocity, and the tortuosity and heterogeneity of the porous medium. Although the porous medium considered in our study is not, strictly speaking, homogeneous, we base our estimate for a_L on Michelsen *et al.* (2023) who performed 13 different investigations across a range of flow speeds, temperatures and pressures and found that $a_L = 0.04\, L_c/25$ in which L_c is a characteristic length scale. If, in specifying this length scale, we follow Gelhar *et al.* (1992) and use the maximum downdip distance available to the expanding gravity current, i.e. $L_c = 400\,\mathrm{m}$, we find that $a_L = 0.64\,\mathrm{m}$, which is broadly consistent with the range of values reported by Tek (1989) and Carriere *et al.* (1985). In general, transverse dispersion is two orders of magnitude smaller than longitudinal dispersion (Feldmann *et al.*, 2016) on which basis we set $a_T = 0.0064\,\mathrm{m}$.

4.4 Theoretical model development

The exposition presented in this section is adapted from the more expansive derivation presented in Sheikhi & Flynn (2024). Although the equations to follow have been published previously, they are reproduced here for the sake of completeness in this standalone study.

Sheikhi & Flynn (2024) investigate the flow evolution of an incompressible gravity current from a line source through a lower layer with a constant permeability, k. The gravity current experiences

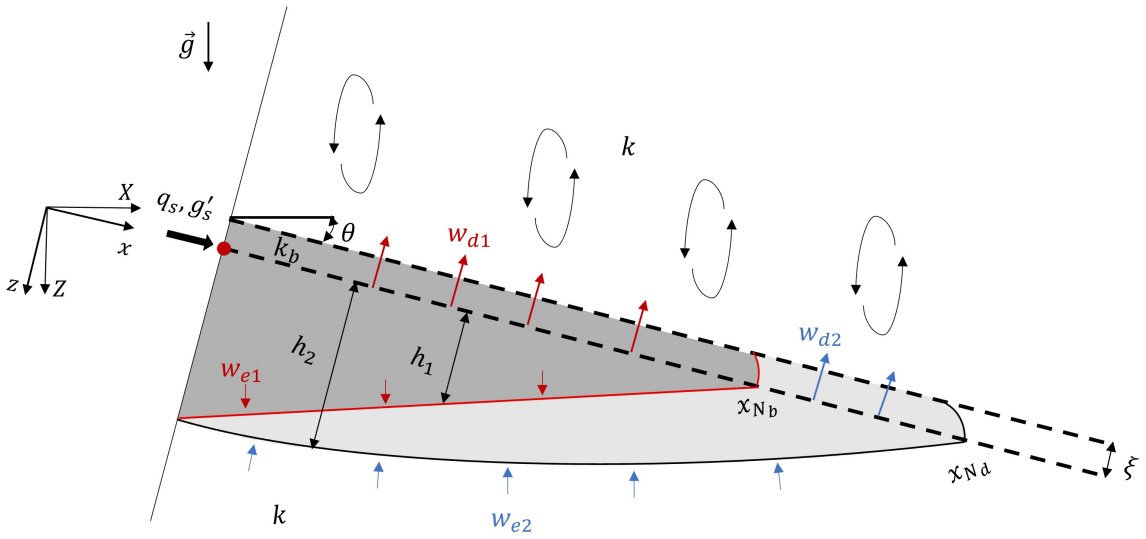

Figure 4.3: [colour] Schematic of a leaky gravity current elongating over an inclined interbed layer. The upper and lower layers have identical permeability, k, and the interbed layer has a smaller permeability, k_b. The red and black lines respectively define the boundaries of the bulk and dispersed phases of the gravity current. We assume a "perfect mixing model" whereby source fluid that drains into the upper layer is quickly and thoroughly mixed into the surrounding ambient. Adapted from figure 2 of Sheikhi & Flynn (2024).

boundary drainage through a thin interbed layer of thickness ξ and permeability k_b – see figure 4.3. The authors model mass exchange between the gravity current and surrounding ambient fluid by defining entrainment velocities. Borrowing ideas from Ellison & Turner (1959) and the theory of free jets, Sheikhi & Flynn (2024) employ the simplest possible entrainment relationship, namely that the entrainment velocity is proportional to the gravity current characteristic velocity. As a result of this entrainment, there develops within the gravity current two phases, i.e. a bulk phase consisting of essentially undiluted source fluid and a dispersed phase consisting of fluid that is a mixture of source and ambient fluid – see figure 4.3. The density of the dispersed phase is therefore between that of the ambient and that of the source.

Sheikhi & Flynn (2024) define as their characteristic length scale

$$\Pi_1 = \frac{\nu q_s}{k g_s'}\,, \tag{4.11}$$

and as their characteristic time scale

$$\Pi_2 = \phi q_s \left(\frac{\nu}{k g_s'} \right)^2 , \tag{4.12}$$

in which q_s is the injectate source volume flow rate (per unit span and therefore expressed in units of length^2/time), g_s' is the source reduced gravity and ν is the kinematic viscosity. As regards this latter variable, recall that Sheikhi & Flynn (2024) assume that the kinematic viscosity of all phases (bulk, dispersed and ambient) are identical. The advent of Π_1 and Π_2 allows us to introduce the following non-dimensional variables:

$$x^* = \frac{x}{\Pi_1} , \quad \xi^* = \frac{\xi}{\Pi_1} , \quad h_1^* = \frac{h_1}{\Pi_1} , \quad h_2^* = \frac{h_2}{\Pi_1} , \quad t^* = \frac{t}{\Pi_2} , \quad w_d^* = w_d \frac{\Pi_2}{\Pi_1} . \tag{4.13a-f}$$

Further to figure 4.3, h_1 and $h_2 - h_1$ denote, respectively, the depths of the bulk and dispersed phases. Meanwhile, w_d is the drainage velocity oriented in a direction perpendicular to the interbed layer. The height h_1 (h_2) can be resolved by integrating the mass continuity equation over the depth of the bulk (dispersed) phase. After a nontrivial amount of algebra, it can be shown that

$$\frac{\partial h_1^*}{\partial t^*} + \frac{\partial (h_1^* U^*)}{\partial x^*} = -\varepsilon U^* - w_{d1}^* , \tag{4.14}$$

and

$$\frac{\partial h_2^*}{\partial t^*} - \frac{\partial}{\partial x^*} \Big[\big(h_2^* - h_1^* \big) \Big(\frac{\partial \Psi^*}{\partial x^*} + C^* \sin\theta \Big) - h_1^* U^* \Big] = -\varepsilon \Big(\frac{\partial \Psi^*}{\partial x^*} + C^* \sin\theta \Big) - w_{d1}^* - w_{d2}^* , \tag{4.15}$$

where, for notational convenience, we have introduced the following parameters:

$$U^* = -\Big(\frac{\partial b_2^*}{\partial x^*} + \frac{\partial h_1^*}{\partial x^*} \Big) \cos\theta - \sin\theta , \tag{4.16}$$

$$\Psi^* = \frac{b_2^* \, h_2^*}{h_2^* - h_1^*} \cos\theta , \tag{4.17}$$

$$C^* = \frac{b_2^*}{h_2^* - h_1^*} . \tag{4.18}$$

In these last equations, reference is made to b_2^*, the z-averaged buoyancy in the dispersed phase. (The rotated coordinate, z, is defined in figure 4.3.) Note that b_2^* is described by its own evolution equation, which is derived by performing a solute mass balance on the dispersed phase. Thus can it be shown that

$$\frac{\partial b_2^*}{\partial t^*} - \frac{\partial}{\partial x^*}\Big[b_2^*\Big(\frac{\partial \Psi^*}{\partial x^*} + C^* \sin\theta\Big)\Big] = \varepsilon U^*\, H(x_{N_b}^* - x^*) - w_{d2}^*\, C^*\,. \tag{4.19}$$

Finally, the parameter ε that appears in (4.14-4.19) is an entrainment coefficient; ε can be evaluated from figure 5 of Sheikhi & Flynn (2024).

Before (4.14), (4.15) and (4.19) can be solved for h_1^*, h_2^* and b_2^*, respectively, expressions must be derived for the drainage velocities w_{d1} and w_{d2}. To this end, Sheikhi & Flynn (2024) consider two bookend opposite scenarios, namely the no mixing limit and the perfect mixing limit. In the former, source fluid drains into the upper layer, evenly displacing the ambient fluid native to this upper layer. In the latter, source fluid rapidly mixes into the upper layer ambient, whose density is minimally impacted by said mixing. Whereas the no mixing model exhibits moderately better agreement with COMSOL-based numerical output at small times, it suffers from a longer time divergence owing to its overestimation of the degree of gravity current retraction after a maximum downdip distance has been achieved. This shortcoming motivates us to consider only the perfect mixing model in the current study. Thus do we anticipate that the drainage velocities w_{d1}^* or w_{d2}^* are uninfluenced by the degree of drainage that has occurred at previous times. Accordingly, the drainage velocities are given by

$$w_{d1}^* = K\cos\theta \begin{cases} \left(\frac{h_1^*+b_2^*}{\xi^*}+1\right) & 0 \le x^* < x_{N_b}^* \\ 0 & x_{N_b}^* < x^* \le x_{N_d}^* \end{cases}, \tag{4.20}$$

and

$$w_{d2}^* = K\cos\theta \begin{cases} 0 & 0 \le x^* < x_{N_b}^* \\ C^*\left(\frac{h_2^*}{\xi^*}+1\right) & x_{N_b}^* \le x^* \le x_{N_d}^* \end{cases}, \tag{4.21}$$

where $K = \frac{k_b}{k}$ is permeability ratio. Exploiting K and interbed layer thickness ξ^*, Sheikhi & Flynn

(2024) define an effective permeability

$$K_{\text{eff}} = K\left(1 + \frac{1}{\xi^*}\right) \tag{4.22}$$

that characterizes the value of drainage through the interbed layer.

By solving (4.14), (4.15) and (4.19) subject to the drainage velocities (4.20) and (4.21), estimates can be made for the spatio-temporal evolution of the bulk and dispersed phases. Thereafter, and for each instant in time, it becomes necessary to estimate the fraction of source fluid that resides in one or the other phase. Sheikhi & Flynn (2024) suggest as an appropriate metric the dispersed buoyancy fraction $\tilde{B}_{\text{disp}}$ (i.e. the fraction of the buoyancy that resides in the dispersed phase), which is defined as

$$\tilde{B}_{\text{disp}} \;=\; \frac{B_{\text{disp}}}{B_{\text{bulk}} + B_{\text{disp}}}\,. \tag{4.23}$$

$\tilde{B}_{\text{disp}}$ serves as a helpful representation for the amount of dispersive mixing that takes place as a result of gravity current flow. In (4.23), B_{bulk} and B_{disp} quantify the respective buoyancies of the bulk and dispersed phases. The parameters in question can be found from

$$B_{\text{bulk}} = \int_0^{x^*_{N_b}} h_1^*\,\mathrm{d}x^* \qquad \text{and} \qquad B_{\text{disp}} = \int_0^{x^*_{N_d}} b_2^*\,\mathrm{d}x^*\,. \tag{4.24a,b}$$

Here, $x^*_{N_b}$ and $x^*_{N_d}$ respectively indicate the frontal position (or "nose") of the gravity currents formed by the bulk and dispersed phases – see figure 4.3. The integrals from (4.24) are straightforward to evaluate once the solutions for h_1^*, h_2^* and b_2^* are known. Note that this model is developed specifically to account for the injection cycle of UHS and it is this cycle that therefore occupies our attention in the following section.

4.5 Results

4.5.1 Comparison of the theoretical and numerical results

The theoretical model of section 4.4 is formulated in terms of non-dimensional variables, however, and for the most part, we shall represent theoretical predictions using dimensional variables, this to facilitate the comparison with the OpenGoSim- and CMG-based numerical results. Of course, swapping between dimensional and non-dimensional variables is straightforward and is achieved by application of (4.13). We consider a 6 month injection period as is appropriate for the case of seasonal storage with green hydrogen derived from e.g. the excess electricity generated from solar panels. With reference to the flow evolution of the bulk and dispersed phases, figure 4.4 compares predictions of the theoretical model against the numerical solutions returned by CMG and OpenGoSim. As shown in this figure, the theoretical model predicts the gravity current profile and dispersion amount relatively well. The positive agreement evident in figure 4.4 suggests that the effects of source momentum are insignificant so that the gravity current can be assumed buoyancy-driven rather than momentum-driven. Furthermore, the difference in viscosity with concentration that is ignored in the theoretical model does not substantially impair the ability of the theoretical model to yield reasonable predictions.

A further important conclusion from figure 4.4 is that the numerical results generated by OpenGoSim are very similar to those generated by CMG. We explore this equivalence in quantitative detail in figure 4.5, which plots timeseries of $\tilde{B}_{\text{disp}}$, the dispersed phase buoyancy fraction. The left- and right-hand side subplots show OpenGoSim and CMG results, respectively. A total of four curves are included in each subplot corresponding to the following values for K_{eff}: 0.015, 0.03, 0.045 and 0.06. Although CMG predicts slightly larger values for $\tilde{B}_{\text{disp}}$ and therefore more overall dispersion, particularly for small K_{eff}, the similarities between panels (a) and (b) of figure 4.5 are more striking than their differences. Given these similarities, plus those evident from figure 4.4, we will hereafter restrict attention to CMG numerical output so as to avoid unnecessary repetition.

The curves of figure 4.5 (b) include dark shading for sufficiently large time and/or K_{eff}. Within

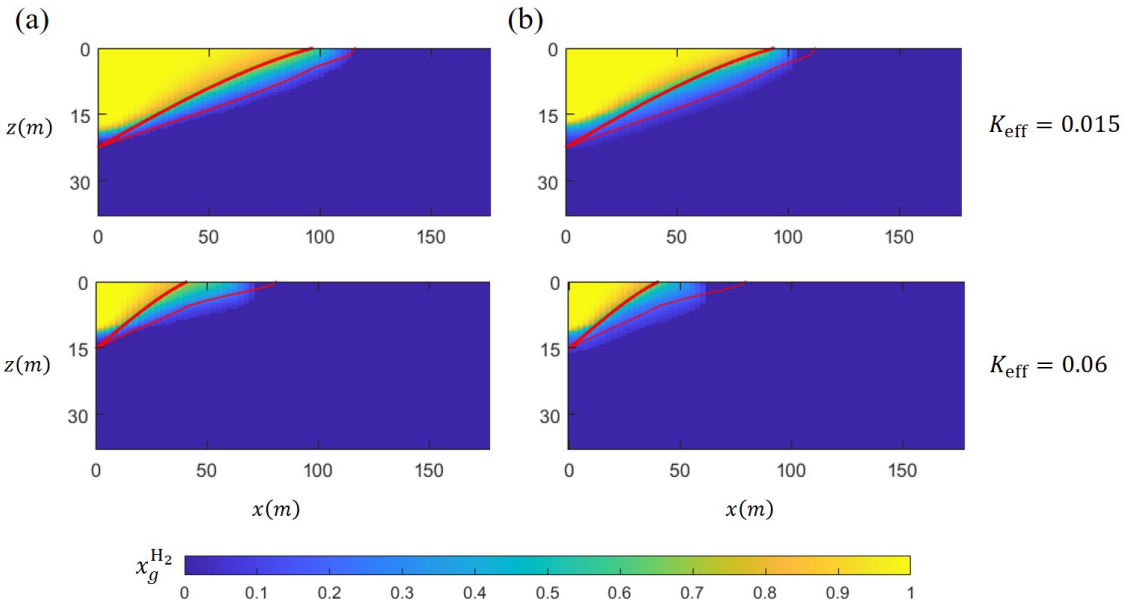

Figure 4.4: [colour] Theoretical predictions for the profile of the bulk phase gravity current (thick solid curves) and the dispersed phase gravity current (thin solid curves) vs. the analogue numerical simulation output (color contours) computed using (a) OpenGoSim, and, (b) CMG. Here we consider a dip angle of $\theta = 0°$, a total time of 6 months and two different values for K_{eff}, defined by (4.22).

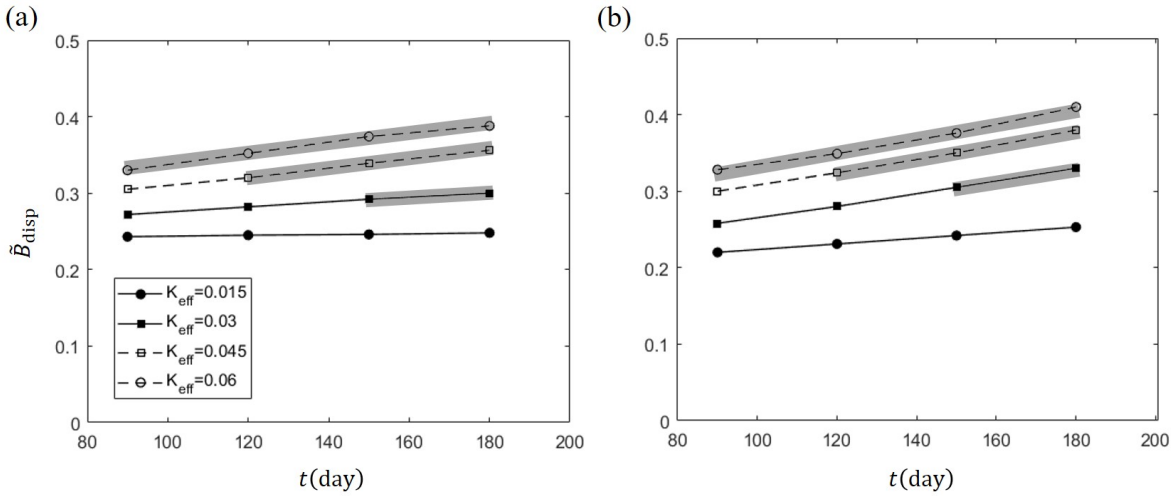

Figure 4.5: Time series data of the buoyancy fraction in the dispersed phase for $\theta = 0°$ and different K_{eff}. (a) OpenGoSim results, and, (b) CMG results. Lines connecting adjacent data points are included to highlight the overall trend of the numerical data. Shaded domains indicate times when the gravity current bulk phase either stops elongating or experiences retraction. The time $t = 0$ corresponds to the initiation of hydrogen flow.

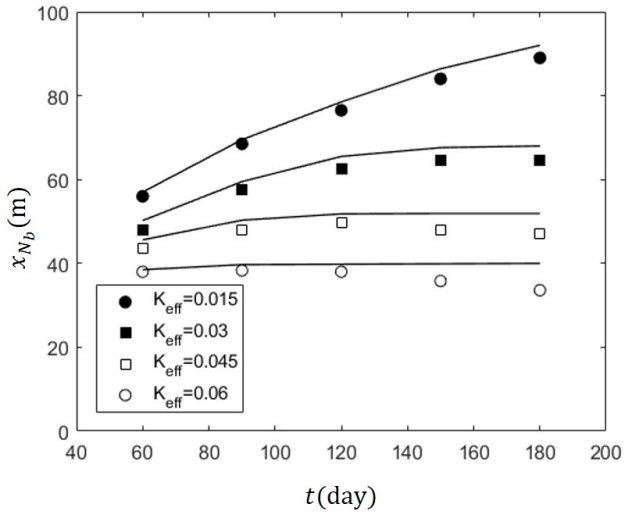

Figure 4.6: Time variation of the bulk nose positions predicted by CMG for various K_{eff} and $\theta = 0°$. Theoretical predictions for each K_{eff} value are indicated with the solid lines.

these shaded regions, the bulk and dispersed phase gravity currents are expected to stop elongating and possibly even retract. Such retraction behavior, which is not well-represented by a perfect mixing-type theoretical model, is even more clearly illustrated by figure 4.6. Similar to figure 4.5, figure 4.6 is a time-series image. Here, however, we consider the temporal evolution of x_{N_b}, the bulk phase nose position, rather than $\tilde{B}_{\text{disp}}$. As figure 4.6 makes clear, the bulk phase gravity current stops elongating and/or retracts earlier for larger K_{eff}. In this regime of large K_{eff}, the theoretical model over-predicts the horizontal extent of the bulk phase to a greater extent than when K_{eff} is small. Indeed, and for even larger K_{eff} values than we consider in figure 4.6, the theoretical model breaks down altogether – see e.g. figure 8 of Sheikhi & Flynn (2024) and the discussion thereof.

Earlier, we stated that the hydrogen flow is expected to be largely buoyancy-driven. The impact of formation vs. source pressure is therefore expected to be of secondary importance given that larger pressures cause an increase of density of both the cushion gas and injected hydrogen. The CMG numerical simulations provide an ideal platform by which to test the above hypothesis. To this end, figure 4.7 investigates the effect of formation pressure on the dispersive mixing in gravity currents. Figure 4.7 illustrates the variation of the dispersed phase buoyancy fraction with K_{eff} for different formation pressures. Also included in figure 4.7 are theoretical predictions derived from the model

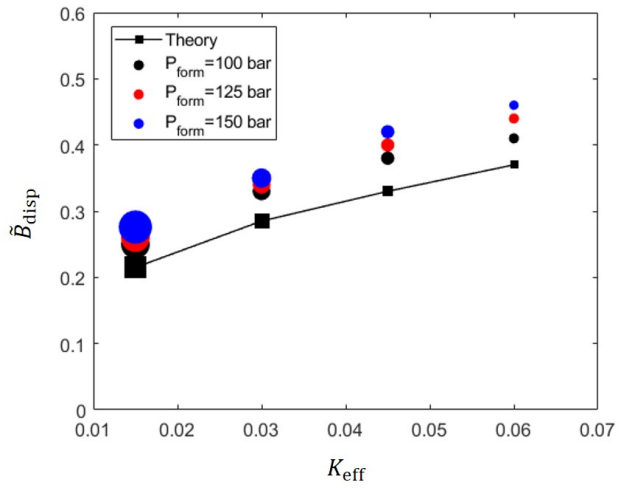

Figure 4.7: [colour] Dispersed phase buoyancy fraction vs. K_{eff} for formation pressures of $P_{\mathrm{form}} =$ 100 bar, 125 bar and 150 bar. Results are shown assuming $\theta = 0°$, $t = 180$ days for black circles, $t = 92$ days for red circles and $t = 53$ days for blue circles. In all cases, $t^* = 90$, where (4.13) is used in defining the non-dimensional time. For each pressure, the marker size indicates the volume of fluid in the bulk phase. For ease of presentation, data are normalized so that the symbols corresponding to $K_{\mathrm{eff}} = 0.06$ are all the same size.

of Sheikhi & Flynn (2024). Note that the black, red and blue data points of figure 4.7 are shown at different dimensional times but the same non-dimensional time, i.e. $t^* = 90$. In this way, we account for the fact that the bulk and dispersed phase gravity currents do not propagate as far when P_{form} is increased. Figure 4.7 reaffirms that there is a generally good agreement between the theoretical results and numerical simulations. In contextualizing this overall good agreement, recall that the theoretical model is, in non-dimensional form, agnostic to the particular value of formation pressure. The situation is slightly different for our numerical results as the associated data demonstrate a mild sensitivity to P_{form}, especially for larger K_{eff}. To understand this difference, consider figure 4.8, which shows the bulk nose position vs. time for three different pressures and two different values of K_{eff}. We present data in a non-dimensional format in figure 4.8 in order to facilitate a fair comparison between data sets having different formation pressures. The results displayed in the left-hand side panel corresponding to $K_{\mathrm{eff}} = 0.015$ predict no retraction of the bulk phase over the indicated time period. However, and for the larger value of $K_{\mathrm{eff}} = 0.06$ shown in the right-hand side panel, retraction is evident for times as small as $t^* = 60$ when $P_{\mathrm{form}} = 150$ bar. The fact that gravity current retraction both occurs earlier and is more severe at elevated pressures is important:

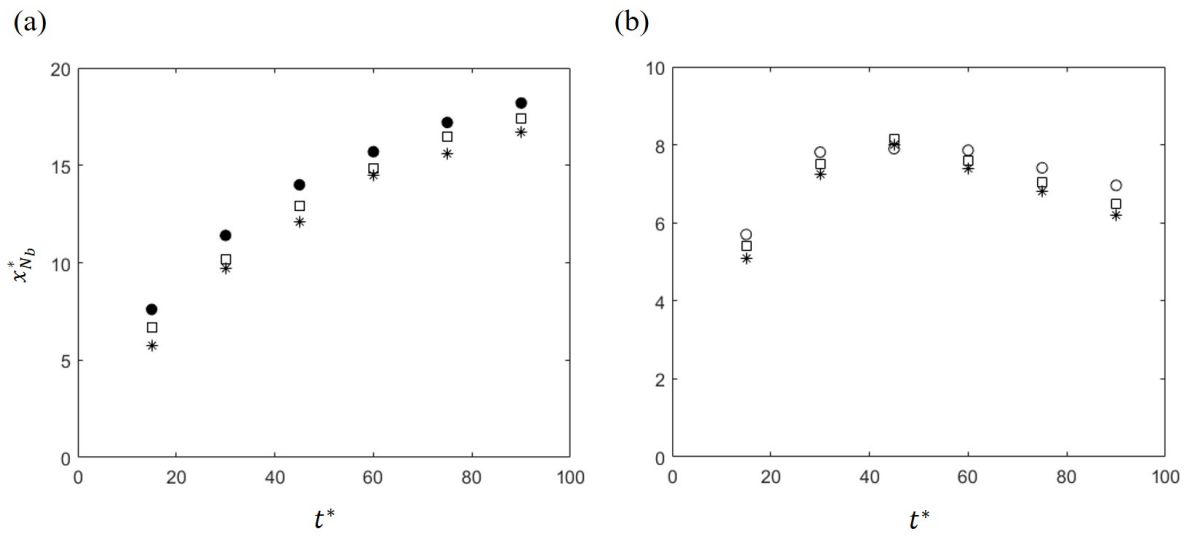

Figure 4.8: Variation of the bulk phase non-dimensional nose position as a function of non-dimensional time t^*, compared for different formation pressures, namely 100 bar (circles), 125 bar (squares) and 150 bar (stars). (a) $K_{\text{eff}} = 0.015$, and, (b) $K_{\text{eff}} = 0.06$. In both panels, we assume a horizontal interbed layer such that $\theta = 0°$.

retraction is a consequence of draining and draining disproportionately removes bulk phase fluid. In other words, the greater the retraction, the larger the fraction of the hydrogen that appears in the dispersed phase. Correspondingly, we expect to measure larger values for $\tilde{B}_{\text{disp}}$ at the elevated pressures of 125 bar and, more especially, 150 bar. This expectation is, of course, consistent with the trends of the black, red and blue data points indicated in figure 4.7.

A complementary comparison between the predictions of our theoretical model and CMG-based numerical results but with an inclination angle $\theta = 10°$ is presented in figure 4.9. Comparing figure 4.9 and 4.4(b) shows that, as expected, the gravity current propagates less distance as we increase the inclination angle. This point aside, it is reassuring to note that figure 4.9 shows the same positive agreement between theory and numerical simulations as is evident in figure 4.4.

All the above results consider an unconfined reservoir where the boundaries do not affect the gravity current flow. In figure 4.10, the domain height is decreased from 150 m to 50 m in order to analyze the performance of the theoretical model in a confined reservoir. When we limit the vertical extent of the reservoir, there arise three potentially-important effects that are omitted

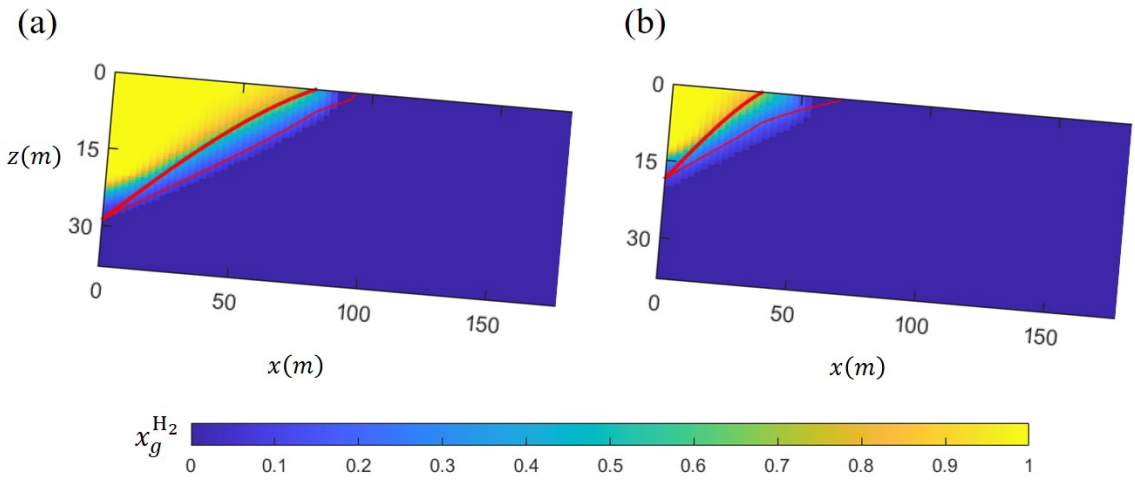

Figure 4.9: [colour] As in figure 4.4 but with an inclination angle $\theta = 10°$. (a) $K_{\text{eff}} = 0.015$ (b) $K_{\text{eff}} = 0.06$. Note that only CMG-based numerical results are shown.

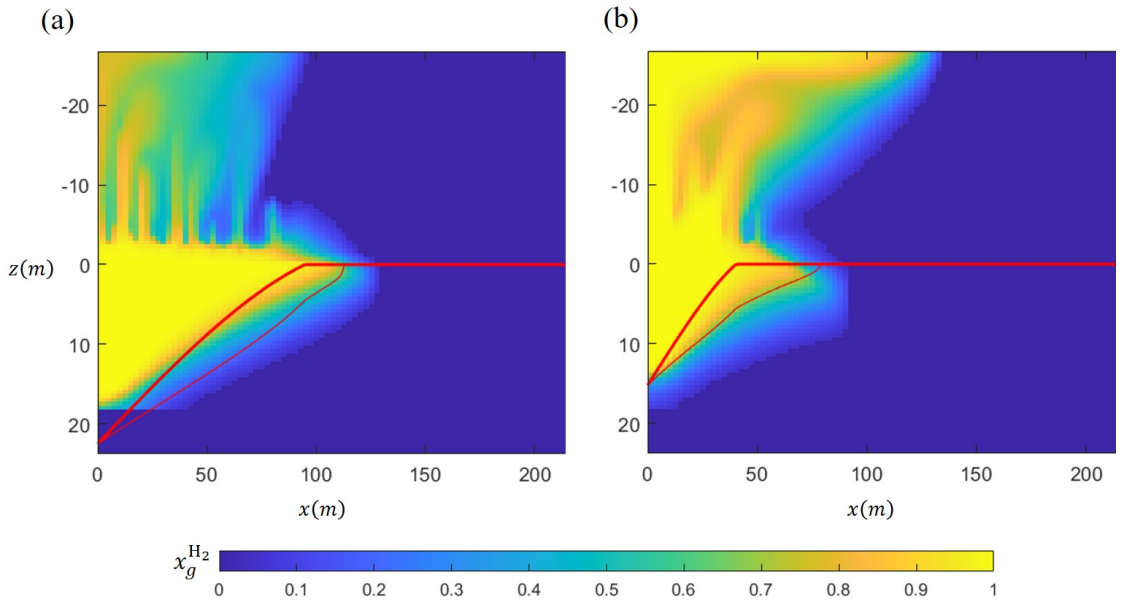

Figure 4.10: [colour] Gravity current evolution in a vertically-confined porous medium where $\theta = 0°$. As in figures 4.4 and 4.9, the thick and thin red curves indicate the theoretically-predicted boundaries for the bulk and dispersed gravity currents. Color contours show the output of the CMG numerical simulations. (a) $K_{\text{eff}} = 0.015$, and, (b) $K_{\text{eff}} = 0.06$. Results are shown after 6 months of hydrogen injection.

by the theoretical model. First, the counter-flow of ambient fluid is now more substantial and therefore likewise the shear stress exerted by this counter-flow on the advancing gravity current. Thus does the viscosity of the ambient fluid, a variable ignored in the theoretical analysis, become important in describing the evolution of the (coupled ambient-gravity current) flow (Pegler *et al.*, 2014). Second, and counterbalancing the above effect, confined layers are associated with the appearance of secondary gravity currents, which in this case appear along the underside of the upper boundary in figure 4.10 (b). It is known from the similitude laboratory experimental work of Bharath & Flynn (2021) that secondary gravity currents can exert a "tugging" force on primary gravity currents arrested along a permeability jump. Third, gravity current fluid drained into the upper layer may accumulate, leading to a decrease in the drainage velocities predicted by (4.20) and (4.21) and a corresponding increase in the rate and distance of gravity current advance. Of the three effects just listed, evidence suggests that the third is the most important. For instance, and comparing $K_{\text{eff}} = 0.015$ results for an effectively unconfined upper layer (i.e. figure 4.4 b) against figure 4.10 (a), we find that the averaged drained flux reduces from 915 S m^3/day to 524 S m^3/day when the depth of the upper layer reduces from 150 m to 50 m. Thus do we observe in figure 4.10 that theory generally under-predicts the horizontal extent of the gravity current that forms immediately below the interbed layer. The under-prediction in question is especially notable when considering the larger effective permeability of $K_{\text{eff}} = 0.06$.

4.5.2 Results beyond the theoretical model

A imitation of the theoretical model of Sheikhi & Flynn (2024) is that it is limited to interbed layers that are flat (whether horizontal or inclined). However, the most desirable formations for the geological storage of hydrogen are anticline structures that are characterized by a structural fold in the rock layers – see figure 4.1 b. Because the inclination angle varies with position in anticline reservoirs, the theoretical model of Sheikhi & Flynn (2024) is unable to predict the flow evolution. In this final subsection, we therefore deviate from the direction of much of the rest of our exposition and present numerical results without accompanying theoretical predictions. Accordingly, we include as supplemental information a video that illustrates the CMG-resolved flow evolution for the case

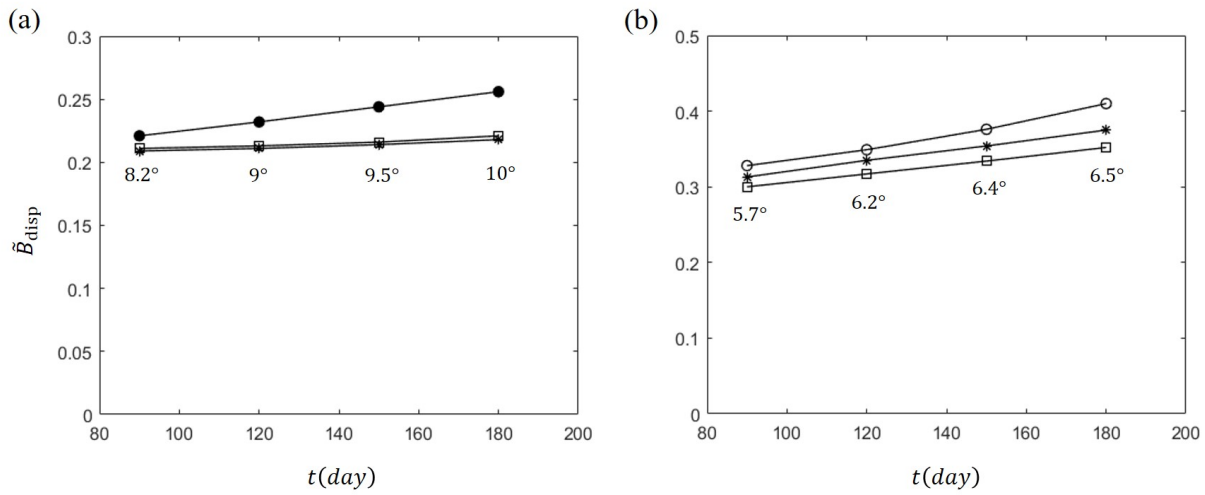

Figure 4.11: Time series data of the dispersed phase buoyancy fraction for a horizontal (circles), 10° inclined (squares) and anticline (stars) domain. (a) $K_{\text{eff}} = 0.015$, and, (b) $K_{\text{eff}} = 0.06$. Note that the y-axis limits are different for panels (a) and (b). Note that the closed and open circles are drawn directly from figure 4.5 (b). Note also that the average inclination angle experienced by a gravity current in an anticline domain progressively increases as time evolves and the gravity current elongates. The average inclination angle is specified here at $t = 90$ days, 120 days, 150 days and 180 days.

of an anticline geometry. Complementing this video, figure 4.11 compares the amount of dispersive mixing associated with gravity current flow within a horizontal vs. inclined vs. anticline domain. This figure suggests that the degree of dispersive mixing realized in an anticline reservoir depends on the average inclination angle experienced by the gravity current as well as the effective permeability of the interbed layer. Focusing on this latter variable first, note that as K_{eff} increases, the gravity current experiences severe drainage and therefore elongates less. Correspondingly, the average inclination angles documented in figure 4.11 b are less than those given in figure 4.11 a. In figure 4.11 a, mixing for the anticline case is close to that for the inclined case because the average inclination angle is close to 10°. On the other hand, the average inclination angles reported in figure 4.11 b fall closer to the average of the $\theta = 0°$ and $\theta = 10°$ cases. It is little surprise, therefore, that $\tilde{B}_{\text{disp}}$ values for the anticline geometry likewise fall roughly halfway between the $\tilde{B}_{\text{disp}}$ values for the other two geometries.

4.6 Conclusions

Numerical simulations are presented to assess the accuracy of the theoretical model presented by Sheikhi & Flynn (2024) vis-à-vis hydrogen storage in depleted natural gas reservoirs. Numerical simulations are conducted using two reservoir simulation packages, namely OpenGoSim and CMG. Consistent with the theoretical model of section 4.4, the numerical simulations of section 4.3 consider flow in a porous medium intersected by a thin interbed layer of substantially reduced permeability – see figure 4.1. Comparison of the numerical results and theoretical predictions indicates that the simplifying assumptions associated with the theoretical model do not lead to significant errors in the UHS context. These simplifying assumptions include, for example, the neglect of detailed thermodynamical relationships, the neglect of the dependence of gas viscosity on composition and the application of a linear entrainment law. On the other hand, the numerical simulations allow us to explore phenomena beyond the scope of Sheikhi & Flynn's model e.g. effects due to formation pressure or a curved interbed layer. Regarding the former effect, figure 4.8 demonstrates that the eventual retraction of the gravity current formed by hydrogen injection depends upon the formation pressure (as well as the effective permeability, K_{eff}, of the interbed layer). Regarding the latter effect, figure 4.11 suggests that gravity currents evolving along interbed layers of variable slope can still be well-approximated by a Sheikhi & Flynn (2024)-type formulation provided the average slope angle can be estimated.

A further effect explored in this study concerns the depth of the upper (draining) layer. From the analysis in question (e.g. figure 4.10), we find that the theoretical model may struggle to correctly predict the gravity current evolution if the time horizon is relatively long, the upper layer is relatively thin and K_{eff} is relatively large such that ample draining occurs across the interbed layer. Accounting for these effects in the theoretical model e.g. by modifying the expressions for drainage velocity (4.20) and (4.21) is saved as a topic for later investigations. Furthermore, both the theoretical model and numerical simulations disregard capillary effects and relative permeability effects by treating liquid water within the gas phase as residual in nature. Extending this approach to account for mobile rather than residual water would necessitate expanding the theoretical model

in a manner similar to Golding *et al.* (2011). Also on the topic of future research, it would be worthwhile, as a numerical exercise, to modify the values of the longitudinal (a_L) and transverse (a_T) dispersivities within the interbed layer to determine whether making the change in question has a demonstrable impact on the numerical output. One significant limitation of our current model is its oversimplified representation of layer heterogeneities. In the physical domain considered here, the model only accounts for a single interbed layer with different permeability, neglecting more complex heterogenous layer structures. To address this limitation, future work should focus on enhancing the model to include detailed representations of intricate layer heterogeneities. By incorporating these complexities, the model's applicability in real-world scenarios would be significantly improved.

Notwithstanding this last commentary and the need for future studies, it is necessary to reiterate the advantages of our hydrodynamics-based, namely that it can generate reasonably accurate estimates of hydrogen plume evolution in a small fraction of the time needed to run even coarse-grained numerical simulations e.g. using CMG. Deploying such a reduced-order-model is expected to be especially advantageous when completing an initial screening of multiple, perhaps many, candidate formations for UHS.

Chapter 5

Conclusions and future work

A comprehensive investigation of dispersive mixing in porous media buoyancy-driven flows is conducted using theoretical analysis and simplified/reservoir-level CFD simulations. CFD simulations fall into one of two categories: (i) simulations that mimic similitude experiments to estimate the entrainment coefficient and validate the theoretical model; (ii) reservoir-level simulations that incorporate parameters and effects not included in the theoretical model. After identifying knowledge gaps in Chapter 1, Chapters 2 and 3 investigate mixing owing to mechanical dispersion in gravity currents experiencing local/distributed basal drainage, e.g. through a local fissure or along a thin interbed layer. The investigation in question requires the development of reduced-order theoretical models, which are validated with reference to the output of the commercial CFD package COMSOL. Then, in Chapter 4, the suitability of the aforementioned reduced-order models in describing real geological flows is considered. Particular focus is placed on the societally-important problem of underground hydrogen storage (UHS) using depleted natural gas reservoirs. From the concise summary given above, we now elaborate on the key methodology and significance of each of the technical chapters of this thesis.

In Chapter 2, the dispersive mixing dynamics of gravity currents propagating along a either horizontal or inclined boundary with a thin local fissure are predicted. We provide a set of non-dimensional coupled non-linear advection-dispersion equations in our theoretical model; these equa-

tions are solved subject to well-prescribed boundary conditions. In the context of dispersive mixing, we use a linear entrainment law consistent with previous works of Ellison & Turner (1959) for free jets and Sahu & Neufeld (2020) for porous media gravity currents. Four important parameters are defined in order to solve the dimensionless governing equations: the boundary inclination angle, the upstream flow parameter, the permeability ratio, and the fissure dimensions, which include its width and length. Using COMSOL, we developed a numerical model to fix the value of the entrainment coefficient, ε, and to thereafter validate our theoretical predictions. Our findings indicate that there is generally good agreement between the numerical simulations and theoretical predictions. In particular, the theoretical model accurately predicts the solute or buoyancy fractions in the dispersed vs. bulk phases of the gravity current. Furthermore, the frontal separation distance between the bulk and dispersed phases is accurately determined by our theoretical model, unless draining is so robust that very little or no bulk fluid flows downstream of the fissure. When this is not the case, our numerical and theoretical results indicate that significant mixing may occur beyond the fissure. Lastly, by applying our theoretical model to UHS applications, we demonstrate that the dispersion of hydrogen in the cushion gas diminishes in a relative sense as the injection flow rate increases.

In many real geological settings, gravity currents experience distributed rather than localized basal drainage. In Chapter 3, we therefore study, numerically and theoretically, the elongation of gravity currents over a thin interbed layer whose permeability is spatially-uniform and also less than that of the surrounding porous medium. Adapting results from 2, we build a corresponding theoretical model and a complementary COMSOL-based numerical model to investigate the effects distributed drainage on gravity current dispersive mixing. Here, two important parameters are defined in the dimensionless governing equations: the effective permeability of the interbed layer and the inclination angle. In the context of distributed drainage, the drainage velocity depends on the extent of mixing within the drained fluid in the lower layer. For simplicity, we adopt a binary perspective when considering this drained fluid, i.e. it either mixes completely with the ambient fluid of the lower layer or else it remains as a distinct phase and does not experience any mixing whatsoever. The former scenario predicts the progressive elongation of the gravity current

front, whereas the no mixing model suggests that after some initial elongation, the gravity current retracts to its terminal run-out length. Our results confirm that, up until the point where the no mixing model predicts flow retraction, both theoretical models explain the evolution of the gravity current in a reasonable way. Past this point, however, the front position predicted by the perfect mixing model moderately over-predicts the numerically-derived solution; conversely, the no mixing model significantly under-predicts the front position. Therefore, the theoretical model does not consistently provide meaningful predictions in the long time limit or when the distributed drainage is so robust that the hydrostatic pressure distribution becomes invalid – see figure 3.8. The eventual breakdown of the no mixing model is expected because it makes the assumption that fluid that drains into the lower layer will always contribute to basal drainage. The results of the numerical simulation, which show the formation of convective fingers some of which eventually detach from the base of the gravity current, strongly contradict this assumption.

In Chapter 4, the hydrodynamic-based model from Chapter 3 is applied to UHS in depleted natural gas reservoirs. In doing so, the reduced-order theoretical model is validated against simulations considering the injection period of UHS operations using reservoir-scale simulators, i.e. CMG and OpenGoSim. We compare the numerical results with the perfect mixing model because the no mixing model cannot correctly predict the long-term flow behavior. This comparison demonstrates that the theoretical model makes accurate predictions of the injectate evolution even though it ignores the detailed thermodynamic relationships, gas viscosity dependence on composition, and non-linearities in the entrainment law and equation of state. Our analysis reveals that when the time horizon is relatively long, the upper layer is relatively thin, and the effective permeability K_{eff} is relatively large, leading to significant drainage across the interbed layer, the theoretical model may struggle to correctly predict the flow evolution. Notwithstanding, there exist other regions of the parameter space where our hydrodynamics-based model offers tangible benefits e.g. it can return reasonably accurate predictions of the gravity current shape and mixing dynamics in a fraction of the time required by reservoir-scale simulation software. Therefore, with future improvements, the theoretical model can be applied to vast reservoirs for hydrogen storage with great computational efficiency. On the other hand, the reservoir-scale numerical simulations enable us to investigate

phenomena beyond the scope of the hydrodynamic-based model, such as the effects of formation pressure or flow dynamics in anticline reservoirs.

5.1 Primary contributions from the present work

The following main points might be used to summarize the primary conclusions and contributions of this thesis:

- We extend the preliminary work of Sahu & Neufeld (2020) on dispersive mixing in porous media gravity currents by incorporating both longitudinal and transverse dispersion, rather than focusing solely on transverse dispersion. When longitudinal dispersion is disregarded, the nose position of the advancing gravity current matches that predicted by the sharp interface model. However, we demonstrate that this equivalence breaks down when longitudinal dispersion is considered, providing an improved method for predicting the outcomes of numerical simulations. Additionally, we differentiate between the bulk phase and the dispersed phase within the gravity current. This approach enables us to apply our theoretical model with greater confidence to porous media gravity currents experiencing either local or distributed drainage. Consequently, we can predict the separation of the bulk interface and the dispersed interface due to drainage and dispersion. Furthermore, this framework allows us to quantify the extent of dispersion based on this separation and examine the parameters that influence dispersion.

- According to both theoretical analysis and COMSOL simulation results, dispersion severity for a gravity current experiencing local drainage increases with down-dip inclination angle and fissure drainage, the latter of which follows from an increase in fissure permeability or width. Furthermore, the extent of dispersion increases with the upstream flow parameter Γ, large Γ indicating a flow driven by buoyancy rather than by source momentum. We validate the hydrodynamic component of our theoretical model by comparing its results with COMSOL simulations. By this comparison, we highlight the parameters that can augment hydrogen

dispersion in cushion gas when hydrogen flows underground and drains through discrete faults in the cap rock.

- Similar to the previous bullet, and for the case of gravity currents elongating over an interbed layer, the dispersion severity increases when the interbed layer is more permeable or has a larger down-dip (or smaller up-dip) inclination angle. Upon comparing our theoretical model with COMSOL simulation output, we find that the predictions of gravity current dispersion and nose position are influenced by Rayleigh-Taylor-type instabilities that develop in the lower layer. These instabilities can limit the applicability of our theoretical model, particularly the no mixing model, over large time horizon. Furthermore, the fluid instabilities add complexity to the understanding of the gravity current retraction. While the perfect mixing model fails to predict any retraction, the no-mixing model significantly overestimates it. The instabilities create an intermediate state where neither model can accurately describe the retraction behavior. Although previous studies, e.g. Neufeld & Huppert (2009), have considered the concept of retraction, we examine the realism of retraction as predicted by the no mixing model. We show that this prediction lacks realism, as it fails to account for the instabilities that break the continuity between the gravity current and the draining fluid. These findings highlight the importance of accounting for instabilities in the drained fluid within the theoretical model to achieve more accurate predictions.

- We have demonstrated that a reduced-order model that incorporates hydrodynamics but which ignores thermodynamics can still provide an accurate description of the evolution and dispersive mixing of a hydrogen plume in a UHS in a depleted natural gas reservoir context. By comparing the results of the reduced-order theoretical model with those of reservoir-level simulations, we confirm that at sufficient distant from the injection well, the flow can be considered buoyancy-driven. Furthermore, reservoir-scale simulations suggest that the reduced-order model can approximate the gravity current spread and mixing along anticline interbed layers, as long as the average slope angle can be estimated.

- In this research, we identify key non-dimensional parameters that influence dispersive mix-

ing in porous media gravity currents, particularly those draining through local fissures or permeable layers. These non-dimensional parameters can be utilized to inform investment decisions and optimize field operations, aiming to minimize hydrogen loss due to drainage and dispersion, thereby enhancing the economic viability of underground hydrogen storage projects. Moreover, we shed light on the retraction of gravity currents propagating over a thin permeable layer and its dependence on instabilities in the drained fluid. These insights are important in the context of field measurement and monitoring (which is expensive and so necessarily limited). Unlike the controlled environment of a laboratory, field measurements tend to be more variable and complex. Nevertheless, measurements indicate that an irregular advance of the hydrogen gravity current are not inherently incorrect. Our findings highlight the predominance of hydrodynamic factors over thermodynamic factors in controlling the behavior of hydrogen plumes. Consequently, our study suggests that significant insights into geological hydrogen flow can be achieved by focusing on hydrodynamics alone, thereby reducing computational demands.

5.2 Limitations of the present study to be addressed by future work

After solving several critical problems related to dispersive mixing in leaky porous media gravity currents, future investigations should address the remaining unresolved issues. Key limitation and areas for future research include:

- In this study, the flow of a gravity current is modeled within unconfined reservoirs. It is imperative to incorporate the effects of boundaries into our model to enhance model applicability to confined reservoirs. To this end, the impact of the ambient counter-flow on the injectate gravity current should be incorporated following the approach outlined in Pegler *et al.* (2014). In the context of distributed drainage, the drainage velocity can be adjusted, for example, to account for the fact that drained fluid will form a secondary gravity current

instead of continuing to propagate vertically indefinitely. Consequently, the influence of impermeable upper and lower boundaries on the gravity current will be added to the theoretical model, which should yield longer and more dispersive gravity currents.

- In the simplified hydrodynamic model, we neglect the compressibility of the fluid. Consequently, our theoretical models of Chapters 2 and 3 work within an intermediate non-dimensional length scale. For small x^* (or $r*$), the flow is dominated by source momentum or volume flux rather than buoyancy. Meanwhile, at larger scales, the hydrogen plume is expected to decompress, rendering the incompressible flow assumption invalid. Similar to the problem studied by Pegler *et al.* (2014) for large scales in confined porous media, the flow dynamics are influenced by the pressure difference between the source and the nose of the gravity current. By incorporating compressible fluid dynamics in future work, the applicability of our theoretical models can be extended to encompass larger non-dimensional length scales. In this scenario, the gravity current should extend over a greater distances due to the assistance of pressure in its elongation. The amount of dispersion should therefore increase.

- Our investigation in Chapter 3 is limited to porous media with a single interbed layer. According to the experimental study of Sahu & Neufeld (2023), the presence of multiple layers with different permeabilities amplifies the degree of dispersion within the fluid flow. Integrating multiple interbed layers enables the investigation of buoyancy-driven flow through heterogeneous porous media, such as the transfer of hydrogen gas between distinct layers. The formulation of a comprehensive theoretical framework for multiple interbed layers still remains an open challenge. A comprehensive theoretical framework for heterogeneous porous media improves the accuracy of predictions regarding fluid flow and dispersion in complex geological formations, leading to an increase in hydrogen storage capacity by optimizing the use of available depleted reservoirs.

- As outlined in Chapter 3, the drainage velocity for gravity currents experiencing distributed drainage is influenced by the amount of mixing in the lower layer. For the sake of simplicity, we examine two extreme conditions of no mixing and perfect mixing. This assumption narrows

the operational scope of our theoretical model, as illustrated in figure 3.8. The mathematical approach to investigate the Rayleigh–Taylor-type instabilities and predict the mixing because of the gravity-driven fingers is left for the future study. The mathematical approach to be developed would, if successfully implemented, enable us to predict the drainage velocity much more accurately and, by extension, the gravity current evolution more precisely.

- In the CMG simulations of Chapter 4, the primary input variables are the longitudinal and transverse dispersivities, a_L and a_T, which are assumed to be constant. However, Michelsen *et al.* (2023) suggest that dispersivities are influenced by factors such as flow velocity, pressure, temperature, tortuosity, and the heterogeneity of the domain. It would be preferable to treat these dispersivity coefficients as variables rather than constants. This approach would help determine whether such variability has a significant impact on the numerical predictions.

- The reduced-order theoretical model has been developed exclusively for the injection phase and is not applicable to the withdrawal phase of a UHS project. However, similar to the approaches of Neufeld & Huppert (2009) and Golding *et al.* (2011) in the context of CO_2 sequestration, incorporating a transient source into the theoretical model would enhance its realism vis-á-vis predicting the flow evolution during not just the injection phase but also the withdrawal phase.

- Current simplified theoretical model ignores capillary effects, by considering miscible flow, and treats liquid water within the gas phase as residual, limiting the accuracy of the representation in scenarios involving mobile water. When water in a reservoir transitions from being residual to mobile, dispersion may increase; it seems likely that mobile water enhances the mixing and spreading processes within the porous medium. Extending the theoretical model to account for mobile water by incorporating multiphase flow dynamics, following the approach similar to Golding *et al.* (2011), is kept for future work.

References

Abdellatif, Moheb, Hashemi, Mehrdad & Azizmohammadi, Siroos 2023 Large-scale underground hydrogen storage: integrated modeling of reservoir-wellbore system. *Int. J. of Hydrogen Energy* **48**, 19160–19171.

Acton, D.M., Huppert, H.E. & Worster, M.G. 2001 Two-dimensional viscous gravity currents flowing over a deep porous medium. *J. Fluid Mech.* **440**, 359–380.

Ahmed, Tarek 2010 *Reservoir Engineering Handbook*. London: Elsevier Inc.

Ajayi, T., Gomes, J. S. & Bera, A. 2019 A review of CO_2 storage in geological formations emphasizing modeling, monitoring and capacity estimation approaches. *Petrol. Sci.* **16**, 1028–1063.

Ali, M., Jha, N. K., Pal, N., Keshavarz, A., Hoteit, H. & Sarmadivaleh, M. 2022 Recent advances in carbon dioxide geological storage, experimental procedures, influencing parameters, and future outlook. *Earth Sci. Rev.* **225** (103895).

Alinejad, A., Molazem, M. H., Sharma, A. & Dehghanpour, H. 2024 Predicting hydrogen storage requirements through the natural gas market for a low-emission future. *Int. J. of Hydrogen Energy* **52**, 787–803.

Amid, A., Mignard, D. & Wilkinson, W. 2016 Seasonal storage of hydrogen in a depleted natural gas reservoirr. *Intl. J. Hydrogen Energy* **42**, 5549–5558.

Amooie, A., Gong, Y., Sedghi, M., McCaskill, B. & Piri, M. 2024 A pore-network modeling perspective on the dynamics of residual trapping in geological carbon storage. *Int. J. Greenh. Gas Control* **136**, 104200.

Anderson, D. M., McLaughlin, R. M. & Miller, C. T. 2003 On gravity currents in heterogeneous porous media. *Dev. Water Sci.* **55**, 2810–2829.

Andrews, J. & Shabani, B. 2012 Where does hydrogen fit in a sustainable energy economy? In *International Energy Congress (IEF-IEC)*. Australia.

Avci, C.B. 1994 Evaluation of flow leakage through abandoned wells and boreholes. *Water Resour. Res.* **30**, 2565–2578.

Bear, J. 1972 *Dynamics of fluid in porous media*. Dover.

Behnam, G.P., Bickle, M.J. & Neufeld, J.A. 2021 Two-phase gravity currents in layered porous media. *J. Fluid Mech.* **922** (A7).

Bello, A., Dorhjie, D. B., Ivanova, A. & Cheremisin, A. 2024 Numerical sensitivity analysis of co_2 mineralization trapping mechanisms in a deep saline aquifer. *Chem. Engineering Sci.* **283**, 119335.

Bharath, K.S. & Flynn, M. R. 2021 Buoyant convection in heterogeneous porous media with an inclined permeability jump: an experimental investigation of filling box-type flows. *J. Fluid Mech.* **924**, A35.

Bharath, K.S., Sahu, C.K. & Flynn, M. R. 2020 Isolated buoyant convection in a two-layered porous medium with an inclined permeability jump. *J. Fluid Mech.* **902**, A22.

Bolster, D. 2014 The fluid mechanics of dissolution trapping in geologic storage of co_2. *J. Fluid Mech.* **740**, 1–4.

Bunch, Mark A., Schacht, Ulrike, Amos, Kathryn & Kernen, Rachelle 2024 Key considerations for evaluating underground hydrogen storage (uhs) potential in five contrasting australian basins. *Int. J. of Hydrogen Energy* **67**, 406–420.

Cai, Zuansi, Zhang, Keni & Guo, Chaobin 2022 Development of a novel simulator for modelling underground hydrogen and gas mixture storage. *Int. J. of Hydrogen Energy* **47** (14), 8929–8942.

Carriere, J., Fasanino, G. & Tek, M. R. 1985 Mixing in underground storage reservoirs. In *SPE annual technical conference and exhibition*. Paper No. SPE-14202-MS.

Chen, Z., Huan, G. & Ma, Y. 2006 *computational methods for multiphase flows in porous media*. Philadelphia: Society for Industrial and Applied Mathematics.

Ciriello, V., Longo, S., Chiapponi, L. & Federico, V. Di 2016 Porous gravity currents: A survey to determine the joint influence of fluid rheology and variations of medium properties. *Water Resour. Res.* **92**, 105–115.

Costall, A. R., Harris, B. D., Teo, B., Schaa, R., Wagner, F. M. & Pigois, J. P. 2020 Groundwater throughflow and seawater intrusion in high quality coastal aquifers. *Sci. Rep.* **10** (9866).

Crotogino, F., Donadei, S., Bunger, U. & Landinger, H. 2010 Large-scale hydrogen underground storage for securing future energy supplies. In *18th World Hydrogen Energy Conference*, pp. 16–21.

Delgado, J. M. P. Q. 2007 Longitudinal and transverse dispersion in porous media. *Chemical Engineering Research and Design* **85**, 1245–1252.

Dincer, Ibrahim 2000 Renewable energy and sustainable development: A crucial review. *Renew. Sustain. Energy Rev.* **4**, 157–175.

Ellison, T. H. & Turner, J. S. 1959 Turbulent entrainment in stratified flows. *J. Fluid Mech.* **6**, 423–448.

Energy information administration 2002 Annual energy outlook, department of energy.

Farcas, A. & Woods, A.W. 2009 The effect of drainage on the capillary retention of CO_2 in a layered permeable rock. *J. Fluid Mech.* **618**, 349–359.

Farcas, A. & Woods, A.W. 2013 Three-dimensional buoyancy-driven flow along a fractured boundary. *J. Fluid Mech.* **728**, 279–305.

Feldmann, F., Hagemann, B., Ganzer, L. & Panfilov, M. 2016 Numerical simulation of hydrodynamic and gas mixing processes in underground hydrogen storages. *Environ. Earth Sci.* **75**, 1165.

Flesch, S., Pudlo, D., Albrecht, D., Jacob, A. & Enzmann, F. 2018 Hydrogen underground storaged-petrographic and petrophysical variations in reservoir sandstones from laboratory experiments under simulated reservoir conditions. *Intl. J. Hydrogen Energy* **43**, 20822–20835.

Flett, M., Gurton, R.M. & Taggart, I. 2005 Heterogeneous saline formations: Long-term benefits for geo-sequestration of greenhouse gases. In *Proceedings of the 7. international conference on greenhouse gas control technologies*, , vol. 38. Elsevier Ltd., UK.

Gelhar, L. W., Welty, C. & Rehfeldt, K. R. 1992 A critical review of data on field-scale dispersion in aquifer. *Water Resources Research* **28**, 1955–1974.

Gilmore, K.E., Sahu, C.K., Benham, G.P., Neufeld, J.A. & Bickle, M.J. 2021 Leakage dynamics of fault zones: experimental and analytical study with application to CO_2 storage. *J. Fluid Mech.* **931**, A31.

Goda, T. & Sato, K. 2011 Gravity currents of carbon dioxide with residual gas trapping in a two-layered porous medium. *J. Fluid Mech.* **673**, 60–79.

Golding, M. J., Neufeld, J.A., Hesse, M.A. & Huppert, H.E. 2011 Two-phase gravity currents in porous media. *J. Fluid Mech.* **678**, 248–270.

Gunter, W.D., Perkins, E.H. & McCann, T.J. 1993 Aquifer disposal of co_2-rich gases: reaction design for added capacity. *Energy Conversion and Management* **34**, 941–948.

Hagemann, Birger 2017 Numerical and analytical modeling of gas mixing and bio-reactive transport during underground hydrogen storage. PhD thesis, TU Clausthal.

Happel, John & Brenner, Howard 1991 *Low Reynolds number hydrodynamics: with special applications to particulate media*. Kluwer Academic.

Hassan, Qusay, Abdulateef, Ammar M., Hafedh, Saadoon Abdul, Al-samari, Ahmed, Abdulateef, Jasim, Sameen, Aws Zuhair, Salman, Hayder M., Al-Jiboory, Ali Khudhair, Wieteska, Szymon & Jaszczur, Marek 2023 Renewable energy-to-green hydrogen: A review of main resources routes, processes and evaluation. *Int. J. of Hydrogen Energy* **48**, 17383–17408.

Hassanpouryouzband, A., Joonaki, E., Edlmann, K. & Haszeldine, R. S. 2021 Offshore geological storage of hydrogen: Is this our best option to aschieve net-zero? *ACS Energy Lett.* **6**, 2181–2186.

Hassanpouryouzband, A., Joonaki, E., Edlmann, K. & Heinemann, N. 2020 Thermodynamic and transport properties of hydrogen containing streams. *Sci Data* **7**, 1.

Hesse, M. A., Tchelepi, H. A., Cantwel, B. J. & Jr, F. M. ORR 2007 Gravity currents in horizontal porous layers: transition from early to late self-similarity. *J. Fluid Mech.* **577**, 363–383.

Hinton, E.M. & Woods, A.W. 2018 The effect of vertically varying permeability on tracer dispersion. *J. Fluid Mech.* **860**, 384–407.

Huang, Tianjia, Moridis, George J., Blasingame, Thomas A., Abdulkader, Afifi M. & Yan, Bicheng 2023 Compositional reservoir simulation of underground hydrogen storage in depleted gas reservoirs. *Int. J. of Hydrogen Energy* **48**, 36035–36050.

Huppert, H.E. & Neufeld, J.A. 2014 The fluid mechanics of carbon dioxide sequestration. *Annu. Rev. Fluid Mech.* **46**, 255–272.

Huppert, H.E., Neufeld, J.A. & Strandkvist, C. 2013 The competition between gravity and flow focusing in two-layered porous media. *J. Fluid Mech.* **720**, 5–14.

Huppert, H. & Woods, A. W. 1995 Gravity driven flows in porous layers. *J. Fluid Mech.* **292**, 55–69.

Huyakorn, P.S., Andersen, P.F., Mercer, J.W. & Jr, H.O. White 1987 Saltwater intrusion in aquifers: Development and testing of a three-dimensional finite element model. *Water Resour. Res.* **23**, 293–312.

Ide, S.T., Jessen, K. & Orr Jr, F.M. 2007 Storage of co_2 in saline aquifers: Effects of gravity, viscous, and capillary forces on amount and timing of trapping. *Int. J. Greenh. Gas Control* **1**, 481–491.

Iscan, A. G. & Kok, M. V. 2009 Porosity and permeability determinations in sandstone and limestone rocks using thin section analysis approach. *Energy Sources Part A* **31**, 568–575.

Jafari Raad, S. M., Leonenko, Y. & Hassanzadeh, H. 2022 Hydrogen storage in saline aquifers: opportunities and challenges. *Renew. Sustain. Energy Rev.* **168**, 112846.

Keith, D., Hassanzadeh, H. & Pooladi-Darvish, M. 2004 Reservoir engineering to accelerate dissolution of stored co2 in brines. In *proceedings of* 7^{th} *International Conference on Greenhouse Gas Control Technologies*. IEA Greenhouse Gas Program, Cheltenham, UK.

Khan, Md. Imran, Bharath, K. S. & Flynn, M. R. 2022 Effect of buoyant convection on the spreading and draining of porous media gravity currents along a permeability jump. *Transport in Porous Media* **146**, 721–740.

Kurusta, T., Mucsi, G., Kumar, S. & Kristály, F. 2023 Carbon-dioxide sequestration by mechanical activation of linz-donawitz steel slag; the effect of water on co_2 capture. *Fuel* **352**, 128951.

Leahy, M.J., Ennis-King, J., Hammond, J., Huppert, H.E. & Neufeld, J.A. 2009 Application of gravity currents to the migration of CO_2 in heterogeneous saline formations. *Energy Procedi* pp. 3331–3338.

Li, J., Wei, Y., Liu, L., Li, X. & Yan, R. 2022 The carbon footprint and cost of coal-based hydrogen production with and without carbon capture and storage technology in china. *J. Cleaner prod.* **362**, 132514.

Lohrenz, J., Bray, B.G. & Clark, C.R. 1964 Calculating viscosities of reservoir fluids from their compositions. *J. Pet. Technol.* **16**, 1171–1176.

Lubon, K. & Tarkowski, R. 2021 Numerical simulation of hydrogen injection and withdrawal to and from a deep aquifer in nw poland. *ACS Energy Letters* **6**, 2181–2186.

Luo, Ang, Li, Yongming, Chen, Xi, Zhu, Zhongyi & Peng, Yu 2022 Review of co2 sequestration mechanism in saline aquifers. *Natural Gas Industry B* **9** (4), 383–393.

Lyle, S., Huppert, H. E., Hallworth, M., Bickle, M. & Chadwick, A. 2005 Axisymmetric gravity currents in a porous medium. *J. Fluid Mech.* **543**, 293–302.

Lyu, Xiaocong & Voskov, Denis 2023 Advanced modeling of enhanced co_2 dissolution trapping in saline aquifers. *Int. J. Greenh. Gas Control* **127**, 103907.

MacMinn, C.W., Neufeld, J.A., Hesse, M.A. & Huppert, H. E. 2012 Spreading and convective dissolution of carbon dioxide in vertically confined, horizontal aquifers. *Water Resour. Res.* **48**, 1–21.

Mairhofer, J. 2021 A residual entropy scaling approach for viscosity based on the gerg-2008 equation of state. *Industrial & Engineering Chemistry Research* **60**, 2652–2662.

Massarweh, O. & Abushaikha, A. S. 2024 Co_2 sequestration in subsurface geological formations: A review of trapping mechanisms and monitoring techniques. *Earth Sci. Rev.* **253** (104793).

Metz, B., Davidson, O., de Coninck, H., Loos, M. & Meyer, L. 2005 IPCC special report on carbon dioxide capture and storage.

Michelsen, J., Thaysen, E. M., Hogeweg, S., Hagemann, B., Hassanpouryouzband, A., Langanke, N., Edlmann, K. & Ganzer, L. 2023 Hydrogen reservoir flow behaviour: Measurements of molecular diffusion, mechanical dispersion and relative permeability. *Tech. Rep.*. H2020 HyUSPRe project report.

Millero, F.J. & Poisson, A. 1981 International one-atmosphere equation of state of seawater. *Deep Sea Research* **28**, 625–629.

Muhammed, N. S., Haq, M. B., Al-Shehri, D. A., Al-Ahmed, A., Rahman, M. M., Zaman, E. & Iglauer, S. 2023 Hydrogen storage in depleted gas reservoirs: A comprehensive review. *Fuel* **337** (127032).

Mustafa, A., Lougou, B. G., Shuai, Y., Wang, Z. & Tan, H. 2020 Current technology development for co_2 utilization into solar fuels and chemicals: A review. *J. of energy Chem.* **49**, 96–123.

Muthukumar, P., Kumar, Alok, Afzal, Mahvash, Bhogilla, Satyasekhar, Sharma, Pratibha, Parida, Abhishek, Jana, Sayantan, Kumar, E. Anil, Pai, Ranjith Krishna & Jain, I. P. 2023 Review on large-scale hydrogen storage systems for better sustainability. *Int. J. of Hydrogen Energy* **48**, 33223–33259.

Neufeld, J.A., Hesse, M.A., Riaz, A., Hallworth, M. A., Tchelepi, M. A. & Huppert, H.E. 2010 Convective dissolution of carbon dioxide in saline aquifers. *Geophys. Res. Latt.* **37**, 1–5.

Neufeld, J.A. & Huppert, H.E. 2009 Modelling carbon dioxide sequestration in layered strata. *J. Fluid Mech.* **625**, 353–370.

Neufeld, J.A., Vella, D. & Huppert, H.E. 2009 The effect of a fissure on storage in a porous medium. *J. Fluid Mech.* **639**, 239–259.

Nordbotten, J.M., Celia, M.A. & Bachu, S. 2004 Analytical solutions for leakage rates through abandoned wells. *Water Resour. Res.* **40**.

Nordbotten, J.M., Celia, M.A., Bachu, S. & Dahle, H.K. 2005 Semianalytical solution for CO_2 leakage through an abandoned well. *Environ. Sci. Technol.* **39**, 602–611.

Panfilov, M. 2016 Underground and pipeline hydrogen storage. *Tech. Rep.*. Elsevier Ltd.

Paster, A. & Dagan, G. 2007 Mixing at the interface between two fluids in porous media: a boundary-layer solution. *J. Fluid Mech.* **584**, 455–472.

Pegler, S.S., Huppert, H.E. & Neufeld, J.A. 2014 Fluid injection into a confined porous layer. *J. Fluid Mech.* **745**, 592–620.

Pegler, S.S., Huppert, H.E. & Neufeld, J.A. 2016 Stratified gravity currents in porous media. *J. Fluid Mech.* **791**, 329–357.

Peng, D. Y. & Robinson, D. B. 1976 A new two-constant equation of state. *Ind. Eng. Chem. Fundamen.* **15**, 59–64.

Pfeiffer, Wolf Tilmann & Bauer, Sebastian 2015 Subsurface porous media hydrogen storage – scenario development and simulation. *Energy Proc.* **76**, 1165.

Poling, B.E., Prausnitz, J.M. & O'Connell, J.P. 2001 *The properties of gases and liquids*. New York: vol 5. McGraw-Hill.

Pritchard, D. 2007 Gravity currents over fractured substrates in a porous medium. *J. Fluid Mech.* **584**, 415–431.

Pritchard, D., Woods, A.W. & Hogg, A.J. 2001 On the slow draining of a gravity current moving through a layered permeable medium. *J. Fluid Mech.* **444**, 23–47.

Pryck, K. D. & Boettcher, M. 2024 The rise, fall and rebirth of ocean carbon sequestration as a climate 'solution'. *Glob. Environ. change* **85**, 102820.

Rahman, T., Lebedev, M., Barifcani, A. & Iglauer, S. 2016 Residual trapping of supercritical co_2 in oil-wet sandstone. *J. Colloid Interface Sci.* **469**, 63–68.

Rasmusson, K., Rasmusson, M., Tsang, Y., Benson, S.M., Hingerl, F., Fagerlund, F. & Niemi, A. 2018 Residual trapping of carbon dioxide during geological storage-insight gained through a pore-network modeling approach. *Int. J. Greenh. Gas Control* **74**, 62–78.

Reeuwijk, Maarten Van, Holzner, Markus & Caulfield, C. P. 2019 Mixing and entrainment are suppressed in inclined gravity currents. *J. Fluid Mech.* **873**, 786–815.

Reid, R.C., Sherwood, T.K. & Street, R.E. 1959 The properties of gases and liquids. *Physics Today* **12**, 38–40.

Riaz, A., Hesse, M. & Tchelepi, H. A. 2006 Onset of convection in a gravitationally unstable diffusive boundary layer in porous media. *J. Fluid Mech.* **548**, 87–111.

Rumpf, H. & Gupte, A. R. 1971 Einflüsse der porosität und korngrößenverteilung im widerstandsgesetz der porenströmung†. *Chemie Ingenieur Technik* **43**, 367–375.

Sahimi, Muhammad 2011 *Flow and transport in porous media and fractured rock*. Wiley-VCH.

Sahu, C. K. & Flynn, M. R. 2015 Filling box flows in porous media. *J. Fluid Mech.* **782**, 455–478.

Sahu, C. K. & Flynn, M. R. 2017 The effect of sudden permeability changes in porous media filling box flows. *Transp. Porous Media* **119**, 95–118.

Sahu, C. K. & Neufeld, J. A. 2020 Dispersive entrainment into gravity currents in porous media. *J. Fluid Mech.* **886**, A5.

Sahu, C. K. & Neufeld, J. A. 2023 Experimental insights into gravity-driven flows and mixing in layered porous media. *J. Fluid Mech.* **956** (A27).

Sainz-Garcia, A., Abarca, E., Rubi, V. & Grandia, F. 2017 Assessment of feasible strategies for seasonal underground hydrogen storage in a saline aquifer. *Intl. J. Hydrogen Energy* **42**, 16657–16666.

Salmachi, Alireza, Seyfaee, Ahmad, Robert, Rohan Jeffry, Hosseini, Tara, Nathan, Graham, Ashman, Peter, Roberts, Ashley, Jafarian, Mehdi & Simon, Catherine 2024 Underground hydrogen storage: Integrated surface facilities and fluid flow modelling for depleted gas reservoirs. *Int. J. of Hydrogen Energy* **50**, 1055–1069.

Sari, Emrah & Çiftçi, Erdem 2024 A numerical investigation on the utilization of a depleted natural gas field for seasonal hydrogen storage: A case study for değirmenköy gas field. *Int. J. of Hydrogen Energy* **51**, 219–228.

Scheidegger, A. E. 1961 General theory of dispersion in porous media. *J. Geophysical Research* **66**, 3273–3278.

Sheikhi, S. & Flynn, M. R. 2024 Porous media gravity current flow over an interbed layer: the impact of dispersion and distributed drainage. *J. Fluid Mech.* **984**, A33.

Sheikhi, S., Sahu, C. K. & Flynn, M. R. 2023 Dispersion effects in porous media gravity currents experiencing local drainage. *J. Fluid Mech.* **975**, A18.

Shrivastava, V.K., Nghiem, L.X., Moore, R.G. & Okazawa, T. 2005 Modelling physical dispersion in miscible displacement-part 1: theory and the proposed numerical scheme. *J. of Canadian Petro. Tech.* **44**, 5.

Song, Hongqing, Lao, Junming, Zhang, Liyuan, Xie, Chiyu & Wang, Yuhe 2023 Underground hydrogen storage in reservoirs: pore-scale mechanisms and optimization of storage capacity and efficiency. *Appl. Energy* **337**, 120901.

Szulczewski, M.L. & Juanes, R. 2013 The evolution of miscible gravity currents in horizontal porous layers. *J. Fluid Mech.* **719**, 82–96.

Tarkowski, R. 2019 Underground hydrogen storage: Characteristics and prospects. *Renew. Sustain. Energy Rev.* **105**, 86–94.

Taylor, J. B., Alderson, J.E.A., Kalyanam, K.M., Lyle, A.B. & Phillips, L.A. 1986 Technical and economic assessment of methods for the storage of large quantities of hydrogen. *Intl. J. Hydrogen Energy* **11**, 5–22.

Tek, M. R. 1989 *Underground storage of natural gas: theory and practice*. Berlin: Springer.

Thomas, L. P., Marino, B. M. & Linden, P. F. 1998 Gravity currents over porous substrates. *J. Fluid Mech.* **366**, 239–258.

United Nations 2021, Paris agreement. Sustainable development goals report.

Vella, D. & Huppert, H. E. 2006 Gravity currents in a porous medium at an inclined plane. *J. Fluid Mech.* **555**, 353–362.

Verma, Satish Kumar, Mishra, Shashank Shekhar, Mukhopadhyay, Nilay Krishna & Yadav, Thakur Prasad 2024 Superior catalytic action of high-entropy alloy on hydrogen sorption properties of mgh2. *Int. J. of Hydrogen Energy* **50**, 749–762.

Wang, G., Pickup, G., Sorbie, K. & Mackay, E. 2022 Scaling analysis of hydrogen flow with carbon dioxide cushion gas in subsurface heterogeneous porous media. *Int. J. of Hydrogen Energy* **47**, 1752–1764.

Warnecki, M., Wojnicki, M., Kusnierczyk, J. & Szuflita, S. 2021 Study of the long term acid gas sequestration process in the borzecin structure: measurements insight. *Energies* **14** (17).

Werner, A. D., Bakker, M., Post, V. E. A., Vandenbohede, A., Lu, C., Ataie-Ashtiani, B., Simmons, C. T. & Barry, D. A. 2013 Seawater intrusion processes, investigation and management: Recent advances and future challenges. *Adv. in Water Resour.* **51**, 3–26.

Wooding, R.A. 1963 Convection in a saturated porous medium at large rayleigh number or peclet number. *J. Fluid Mech.* **15**, 527–544.

World Energy Council 2019 New hydrogen economy: hope or hype?

Zamehrian, M. & Sedaee, B. 2022 Underground hydrogen storage in a partially depleted gas condensate reservoir: Influence of cushion gas. *J. of Petro. Sci. and Eng.* **212**, 110304.

Zhang, S., Yuan, Q., Ni, J., Zheng, K., Xu, Y. & Zhang, J. 2024 Co_2 utilization and sequestration in ready-mix concrete—a review. *Sci. of the total environ.* **907**, 168025.

Zhang, Z., Liu, L., Ning, F., Liu, Z., Sun, J., Li, X., Sun, J., Hyodo, M. & Liu, C. 2022 Effect of stress on permeability of clay silty cores recovered from the Shenhu hydrate area of the south China sea. *J. of Natural Gas Sci. and Engineering* **99**, 104421.

Zheng, Z., Christov, I.C. & Stone, H.A. 2014 Influence of heterogeneity on second-kind self-similar solutions for viscous gravity currents. *J. Fluid Mech.* **747**, 217–246.

Zheng, Z., Guo, B., Christov, I.C., Celia, M. A. & Stone, H. A. 2015 Flow regimes for fluid injection into a confined porous medium. *J. Fluid Mech.* **767**, 881–909.

Zivar, Davood, Kumar, Sunil & Foroozesh, Jalal 2021 Underground hydrogen storage: a comprehensive review. *Int. J. of Hydrogen Energy* **46**, 23436–23462.

Zuo, L. & Benson, S. M. 2014 Process-dependent residual trapping of co_2 in sandstone. *Geophys. Res. Lett.* **41**, 2820–2826.

Appendix A

Theory details of gravity currents experiencing local drainage

A.1 Derivation of the bulk and dispersed velocity in the theoretical model

By using the definition of $\Delta\rho_1$, $\Delta\overline{\rho}_2$ and b_2 in terms of concentration, equations (2.7) and (2.8) can be rewritten as

$$p_1(x,z,t) = \rho_0 g\beta\left(b_2 + c_s\, h_1\right)\cos\theta - \rho_s\, gz\cos\theta + \rho_0\, g\, x\sin\theta + P_0 \quad 0 \le z \le h_1\,, \tag{A.1}$$

$$p_2(x,z,t) = \left[\rho_0\, g\beta\,\overline{c}_2 h_2 - \overline{\rho}_2\, gz\right]\cos\theta + \rho_0\, g\, x\sin\theta + P_0 \qquad h_1 \le z \le h_2\,. \tag{A.2}$$

Moreover, Darcy's law (2.12) in the x-direction indicates that

$$u_1(x,t) = -\frac{k}{\mu}\left(\frac{\partial p_1}{\partial x} - \rho_s\, g\sin\theta\right)\,, \tag{A.3}$$

$$u_2(x,t) = -\frac{k}{\mu}\left(\frac{\partial p_2}{\partial x} - \overline{\rho}_2\, g\sin\theta\right)\,. \tag{A.4}$$

If we insert p_1 and p_2 from (A.1) and (A.2) into (A.3) and (A.4), the bulk and dispersed velocities then read

$$u_1(x,t) = -\frac{kg\beta}{\nu}\Big[\frac{\partial b_2}{\partial x}\cos\theta + c_s\Big(\frac{\partial h_1}{\partial x}\cos\theta - \sin\theta\Big)\Big]\,, \tag{A.5}$$

$$u_2(x,t) = -\frac{kg\beta}{\nu}\Big[\Big(\frac{\partial(\overline{c}_2 h_2)}{\partial x} - z\frac{\partial \overline{c}_2}{\partial x}\Big)\cos\theta - \overline{c}_2\sin\theta\Big]\,. \tag{A.6}$$

COMSOL results show that for the conditions relevant to our analysis, the term $z\frac{\partial \overline{c}_2}{\partial x}$ in (A.6) is two order of magnitude smaller than $\frac{\partial(\overline{c}_2 h_2)}{\partial x}$ and can therefore be ignored. Accordingly, velocity in the dispersed phase can be simplified to

$$u_2(x,t) = -\frac{kg\beta}{\nu}\Big[\frac{\partial(\overline{c}_2 h_2)}{\partial x}\cos\theta - \overline{c}_2\sin\theta\Big]\,. \tag{A.7}$$

A.2 Derivation of the drainage velocity in the theoretical model

Using (2.7), the pressure at the bottom boundary of the gravity current is expressed as

$$p(x,0,t) = \big[\Delta\overline{\rho}_2 g h_2 + \big(\Delta\rho_1 - \Delta\overline{\rho}_2\big)g h_1\big]\cos\theta + \rho_0\, g\, x \sin\theta + P_0\,. \tag{A.8}$$

Moreover, and assuming a hydrostatic pressure balance, the pressure at $z = -l$ corresponding to the base of the fissure is given by

$$p(x,-l,t) = \rho_0\, g\, l\cos\theta + \rho_0\, g\, x \sin\theta + P_0\,. \tag{A.9}$$

Analogous to Acton *et al.* (2001), and by considering pressure continuity at $z = 0$, the pressure distribution within the fissure is described by the following linear function:

$$\begin{aligned} p(x,z,t) \;\; = \;\; & \big[\Delta\overline{\rho}_2 g h_2 + \big(\Delta\rho_1 - \Delta\overline{\rho}_2\big)g h_1\big]\Big(1 + \frac{z}{l}\Big)\cos\theta \\ & -\rho_0\, g\, z\cos\theta + \rho_0\, g\, x\sin\theta + P_0 \qquad\qquad -l \le z \le 0\,. \end{aligned} \tag{A.10}$$

Applying Darcy's law, the vertical velocity in the fissure reads

$$w_d(x,t) = -\frac{k_f}{\mu}\Big(\frac{\partial p}{\partial z} + \rho_0\, g\cos\theta\Big) = -\frac{k_f g}{\mu}\Big[\frac{\Delta\overline{\rho}_2 h_2}{l} + \big(\Delta\rho_1 - \Delta\overline{\rho}_2\big)\frac{h_1}{l} + \Delta\rho_1\Big]\cos\theta\,. \tag{A.11}$$

If we insert $\Delta\rho_1 = \rho_0\beta c_s$ and $\Delta\overline{\rho}_2 = \rho_0\beta\,\overline{c}_2$ into (A.11), it can be shown that

$$w_d(x,t) = -\frac{k_f g\beta}{\nu}\Big(\frac{c_s h_1 + b_2}{l} + c_s\Big)\cos\theta\,. \tag{A.12}$$

A.3 Method of solution for the theoretical model

The finite difference method is used to discretize equations (2.27)-(2.29) in space. First-order derivatives in space are discretized using backward finite differences and a central finite difference is used to discretize second-order derivatives. Although implicit methods are more stable, they produce extra diffusion in our solution; we therefore apply an explicit method for time discretization. Thus equations (2.27)-(2.29) may be rewritten in discrete form as

$$\begin{aligned}(h^*_{1,\,i})^{n+1} = (h^*_{1,\,i})^n \; - \Delta t^*\,\big(h^*_{1,\,i}\,dU^*_i\big)^n \; - \Delta t^*\,(U^*_i)^n\,\Big(\frac{h^*_{1,\,i} - h^*_{1,\,i-1}}{\Delta x^*} + \varepsilon\,\Gamma^{1/2}\Big)^n \\ - \Delta t^*\,K\,\Gamma\Big(\frac{h^*_{1,\,i} + b^*_{2,\,i}}{l^*} + 1\Big)^n \cos\theta \times F(x^*, 1, \xi^*)\,,\end{aligned} \tag{A.13}$$

$$\begin{aligned}(h^*_{2,\,i})^{n+1} = (h^*_{2,\,i})^n \; + \frac{\Delta t^*}{(\Delta x^*)^2}\Big[(h^*_{2,\,i} - h^*_{1,\,i})\Big(\Psi^*_{i-1} - 2\Psi^*_i + \Psi^*_{i+1} - (C^*_i - C^*_{i-1})\Delta x^*\Big) \\ + (h^*_{2,\,i} - h^*_{2,\,i-1} - h^*_{1,\,i} + h^*_{1,\,i-1})\big(\Psi^*_i - \Psi^*_{i-1} - C^*_i\,\Delta x^*\big)\Big]^n - \Delta t^*\,\Big(h^*_{1,\,i}\,dU^*_i \; + U^*_i\,\frac{h^*_{1,\,i} - h^*_{1,\,i-1}}{\Delta x^*}\Big)^n \\ - \varepsilon\,\Gamma^{1/2}\,\Delta t^*\,\big(\frac{\Psi^*_i - \Psi^*_{i-1}}{\Delta x^*} - C^*_i\big)^n - \Delta t^*\,K\,\Gamma\Big(\frac{h^*_{1,\,i} + b^*_{2,\,i}}{l^*} + 1\Big)^n \cos\theta \times F(x^*, 1, \xi^*)\,,\end{aligned} \tag{A.14}$$

$$\begin{aligned}(b^*_{2,\,i})^{n+1} = (b^*_{2,\,i})^n \; + \frac{\Delta t^*}{(\Delta x^*)^2}\Big[b^*_{2,\,i}\,\Big(\Psi^*_{i-1} - 2\Psi^*_i + \Psi^*_{i+1} - (C^*_i - C^*_{i-1})\Delta x^*\Big) \\ + (b^*_{2,\,i} - b^*_{2,\,i-1})\big(\Psi^*_i - \Psi^*_{i-1} - C^*_i\,\Delta x^*\big)\Big]^n \; + \Delta t^*\,\varepsilon\,\Gamma^{1/2}(U^*_i)^n\,,\end{aligned} \tag{A.15}$$

respectively. Here, i and n are non-negative indices that respectively correspond to space and time. In addition, $(U_i^*)^n$ and $(dU_i^*)^n$ are defined as

$$(U_i^*)^n = -\Big(\frac{b^*_{2,\,i} - b^*_{2,\,i-1}}{\Delta x^*} + \frac{h^*_{1,\,i} - h^*_{1,\,i-1}}{\Delta x^*}\Big)^n \cos\theta + \Gamma^{1/2}\sin\theta\,, \tag{A.16}$$

$$(dU_i^*)^n = -\Big(\frac{\partial^2 b_2^*}{\partial {x^*}^2} + \frac{\partial^2 h_1^*}{\partial {x^*}^2}\Big)_i^n \cos\theta = \\ - \Big(\frac{b^*_{2,\,i-1} - 2b^*_{2,\,i} + b^*_{2,\,i+1}}{(\Delta x^*)^2} + \frac{h^*_{1,\,i-1} - 2h^*_{1,\,i} + h^*_{1,\,i+1}}{(\Delta x^*)^2}\Big)^n \cos\theta\,. \tag{A.17}$$

Equation (A.13) applies for $i \geq 1$. When $i = 1$, $(h^*_{1,\,0})^n$ in equation (A.13) is found based on the discrete form of the influx boundary condition in (2.34a), such that

$$(h^*_{1,\,0})^n = \frac{\Delta x^*}{\phi\,(h^*_{1,\,1})^n \cos\theta} + (h^*_{1,\,1})^n - (b^*_{2,\,0})^n - \Gamma^{1/2}\tan\theta\,\Delta x^*\,. \tag{A.18}$$

To find $(h^*_{1,\,0})^n$ in (A.18), we assume some amount for $(b^*_{2,\,0})^n$ and solve equations (A.14) and (A.15) for $i = 1$ to recover $(h^*_{2,\,1})^{n+1}$ and $(b^*_{2,\,1})^{n+1}$. We then iterate using the secant method to satisfy boundary conditions (2.34c) and (2.34e), i.e.

$$(h^*_{2,\,1})^{n+1} = (h^*_{1,\,1})^{n+1}\,, \tag{A.19a}$$

$$(b^*_{2,\,1})^{n+1} = 0\,. \tag{A.19b}$$

Then the expressions in (A.14) and (A.15) apply for $i \geq 2$. Finally, for $i = N_b$ and $i = N_d$, the bulk and dispersed nose positions in (2.34b,d,f) read

$$(h^*_{1,\,N_b})^{n+1} = 0\,, \tag{A.20a}$$

$$(h^*_{2,\,N_d})^{n+1} = (b^*_{2,\,N_d})^{n+1} = 0\,. \tag{A.20b}$$

In the above equations, Δx^* and Δt^* indicate the grid spacing and the time step, respectively. Our discretized equations are solved with $\Delta x^* = 10^{-2}$ and $\Delta t^* = 10^{-5}$. We estimate Δx^* by fixing

Δt^* and then performing a grid independence test. Once the largest value of Δx^* that preserves grid independency is determined, Δt^* is increased slightly, but not beyond a value where computed results vary with the magnitude of the time step. With suitable values for Δx^* and Δt^* selected, we find that the run time to produce a figure such as figure 2 is approximately 0.65 Core-hours using an Intel Core i7-9700 CPU (3.00 GHz and 16 GB memory).

Appendix B

Theory details of gravity currents over an interbed layer

B.1 Derivation of the drainage velocity in the perfect mixing model

With reference to figure 3.2, we assume a hydrostatic pressure distribution through the gravity current such that the pressures measured along $z = 0$ in the bulk and dispersed phases are

$$p_{1,I}(x,0,t) = \rho_0 g'_s \left(h_1 + \frac{b_2}{c_s}\right)\cos\theta + P_0 + \rho_0\, g\, x \sin\theta\,, \tag{B.1}$$

$$p_{2,I}(x,0,t) = \rho_0\, g'_s\, C\, h_2 \cos\theta + P_0 + \rho_0\, g\, x \sin\theta\,, \tag{B.2}$$

respectively. Here, subscript I indicates the upper layer of figure 3.2. Turning to the interbed layer, we integrate Darcy's law in the z-direction below the bulk and dispersed phases and find that

$$\int_z^0 \frac{\partial p_{1,II}}{\partial z}\,\mathrm{d}z = -\int_z^0 \rho_0 g'_s \cos\theta\,\mathrm{d}z - \int_z^0 \frac{\mu}{k_b} w_{d1}\,\mathrm{d}z\,, \tag{B.3}$$

$$\int_z^0 \frac{\partial p_{2,II}}{\partial z}\,\mathrm{d}z = -\int_z^0 \rho_0 C g'_s \cos\theta\,\mathrm{d}z - \int_z^0 \frac{\mu}{k_b} w_{d2}\,\mathrm{d}z\,, \tag{B.4}$$

in which subscript II denotes the interbed layer. Fortuitously, all terms under the right-hand side integrals of (B.3) and (B.4) are independent of z and the integrals are therefore straightforward to evaluate. Consistent with Acton *et al.* (2001) and by considering pressure continuity at $z = 0$ such that $p_{1,I}(x, 0, t) = p_{1,II}(x, 0, t)$ and $p_{2,I}(x, 0, t) = p_{2,II}(x, 0, t)$, the pressure distributions through the interbed layer are given by

$$p_{1,II}(x, z, t) = \rho_0 g'_s \left(h_1 + \frac{b_2}{c_s} - z\right)\cos\theta - \frac{\mu}{k_b} w_{d1}\, z + P_0 + \rho_0\, g\, x \sin\theta\,, \tag{B.5}$$

$$p_{2,II}(x, z, t) = \rho_0\, g'_s\, C\,(h_2 - z)\cos\theta - \frac{\mu}{k_b} w_{d2}\, z + P_0 + \rho_0\, g\, x \sin\theta\,, \tag{B.6}$$

for the bulk and dispersed phases, respectively. Also following Acton *et al.* (2001), we set $p_{1,II}(x, -\xi, t) = P_0 + \rho_0\, g\, x \sin\theta$ and $p_{2,II}(x, -\xi, t) = P_0 + \rho_0\, g\, x \sin\theta$. Using these results, the drainage velocities for the perfect mixing case can be recovered by substituting $z = -\xi$ in (B.5) and (B.6) then solving for w_{d1} and w_{d2}, respectively. To wit, we find that

$$w_{d1}(x, t) = \begin{cases} \frac{k_b g'_s}{\nu}\left(\frac{c_s h_1 + b_2}{c_s\, \xi} + 1\right)\cos\theta & 0 \le x < x_{N_b} \\ 0 & x_{N_b} < x \le x_{N_d} \end{cases}, \tag{B.7}$$

and

$$w_{d2}(x, t) = \begin{cases} 0 & 0 \le x < x_{N_b} \\ \frac{k_b g'_s}{\nu}\, C\left(\frac{h_2}{\xi} + 1\right)\cos\theta & x_{N_b} \le x \le x_{N_d} \end{cases}. \tag{B.8}$$

B.2 Derivation of the drainage velocity in the no mixing model

Using (B.5) and (B.6), the pressures measured at the base, $z = -\xi$, of the interbed layer of figure 3.1 are

$$p_{1,II}(x, -\xi, t) = \rho_0 g'_s \left(h_1 + \frac{b_2}{c_s} + \xi\right)\cos\theta + \frac{\mu}{k_b} w_{d1}\, \xi + P_0 + \rho_0\, g\, x \sin\theta\,, \tag{B.9}$$

$$p_{2,II}(x, -\xi, t) = \rho_0\, g'_s\, C\,(h_2 + \xi)\cos\theta + \frac{\mu}{k_b} w_{d2}\, \xi + P_0 + \rho_0\, g\, x \sin\theta\,. \tag{B.10}$$

If we consider, consistent with Neufeld & Huppert (2009), the continuity of flux perpendicular to the boundary at $z = -\xi$, the drainage velocities w_{d1} and w_{d2} must be constant through the interbed

and lower layers. Regarding this lower layer, we integrate Darcy's law in the z-direction and find that

$$\int_z^{-\xi} \frac{\partial p_{1,III}}{\partial z}\,\mathrm{d}z = -\int_z^{-\xi} \rho_0 g_s' \cos\theta\,\mathrm{d}z - \int_z^{-\xi} \frac{\mu}{k} w_{d1}\,\mathrm{d}z\,, \tag{B.11}$$

$$\int_z^{-\xi} \frac{\partial p_{2,III}}{\partial z}\,\mathrm{d}z = -\int_z^{-\xi} \rho_0 C g_s' \cos\theta\,\mathrm{d}z - \int_z^{-\xi} \frac{\mu}{k} w_{d2}\,\mathrm{d}z\,. \tag{B.12}$$

Again, all of the terms under the right-hand side integrals are independent of z. Note that, for the sake of mathematical convenience, we suppose that any drained fluid that appears in the lower layer forms a uniform layer of depth l. This simplification is in obvious contrast to figure 3.1, which defines layer depths l_1 and l_2 for the bulk and dispersed phases, respectively. As a consequence of the simplification, it is appropriate to set $C = 1$ in the former right-hand side terms of (B.10) and (B.12). By assuming pressure continuity at $z = -\xi$, the pressure distributions under the gravity current bulk phase and dispersed phase can be found. These read

$$p_{1,III}(x,z,t) = \rho_0 g_s' \left(h_1 + \frac{b_2}{c_s} - z\right)\cos\theta + \frac{\mu}{k_b} w_{d1}\left[(1-K)\xi - Kz\right] + P_0 + \rho_0\, g\, x \sin\theta\,, \tag{B.13}$$

$$p_{2,III}(x,z,t) = \rho_0 g_s' \left(h_2 - z\right)\cos\theta + \frac{\mu}{k_b} w_{d2}\left[(1-K)\xi - Kz\right] + P_0 + \rho_0\, g\, x \sin\theta\,. \tag{B.14}$$

Consistent with Acton *et al.* (2001), we set $p_{1,III}(x,-l,t) = p_{2,II}(x,-l,t) = P_0 + \rho_0\, g\, x \sin\theta$. Combining this information with (B.13) and (B.14), the drainage velocities in the no mixing case can be written as

$$w_{d1}(x,t) = \begin{cases} \dfrac{k_b g_s'}{\nu}\cos\theta \begin{cases} \left(\frac{c_s h_1 + b_2}{c_s\, l} + 1\right) & l < \xi \\ \frac{c_s h_1 + b_2 + c_s l}{(1-K)c_s\,\xi + K c_s\, l} & l \geq \xi \end{cases} & 0 \leq x < x_{N_b} \\ 0 & x_{N_b} < x \leq x_{N_d} \end{cases}, \tag{B.15}$$

and

$$w_{d2}(x,t) = \begin{cases} 0 & 0 \leq x < x_{N_b} \\ \dfrac{k_b g_s'}{\nu}\cos\theta \begin{cases} \left(\frac{h_2}{l} + 1\right) & l < \xi \\ \frac{h_2 + l}{(1-K)\,\xi + Kl} & l \geq \xi \end{cases} & x_{N_b} \leq x \leq x_{N_d} \end{cases}. \tag{B.16}$$

Reassuringly, (B.15) and (B.16) are consistent with (B.7) and (B.8) when $l < \xi$ such that fluid has not yet drained through the depth of the interbed layer.

Appendix C

Details of numerical simulations

We utilize two distinct sets of numerical simulations in our research. The first set involves COMSOL simulations that replicate similitude laboratory experiments, while the second set comprises CMG/OpenGoSim simulations that mimic reservoir-scale fluid flow. The validation, verification, and sequence of numerical operations in these simulations are highlighted in the following.

C.1 Verification and validation of numerical simulations

C.1.1 COMSOL

We verify the COMSOL model through a grid independence study. Figure 2.5 demonstrates that the COMSOL model is grid independent for the local drainage scenario with $10^{4.91}$ grid cells. Figure C.1 below also shows that the COMSOL model is grid independent with 10^5 grid cells in the distributed drainage scenario.

Our COMSOL model is validated in two complementary way. First, we confirm that it faithfully reproduces the results of a canonical buoyancy-driven flow when dispersion is comparatively small. More specifically, and as indicated in figure C.2 below, we model the flow of a porous media gravity current along an impermeable boundary and thereby demonstrate excellent agreement with the well-accepted theoretical solution of Huppert & Woods (1995). Second, we confirm that our

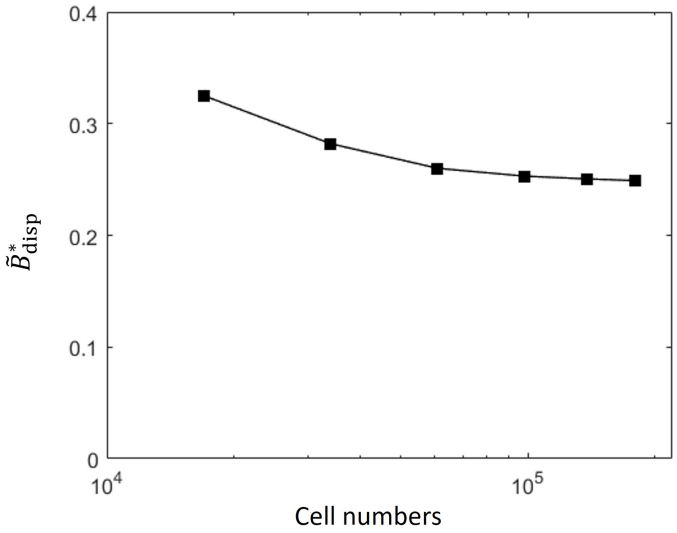

Figure C.1: COMSOL estimates for the dispersed phase bouncy fraction for different grid sizes in the distributed drainage case. Here, $K_{\text{eff}} = 0.015$, $\theta = 0°$ and $t^* = 150$.

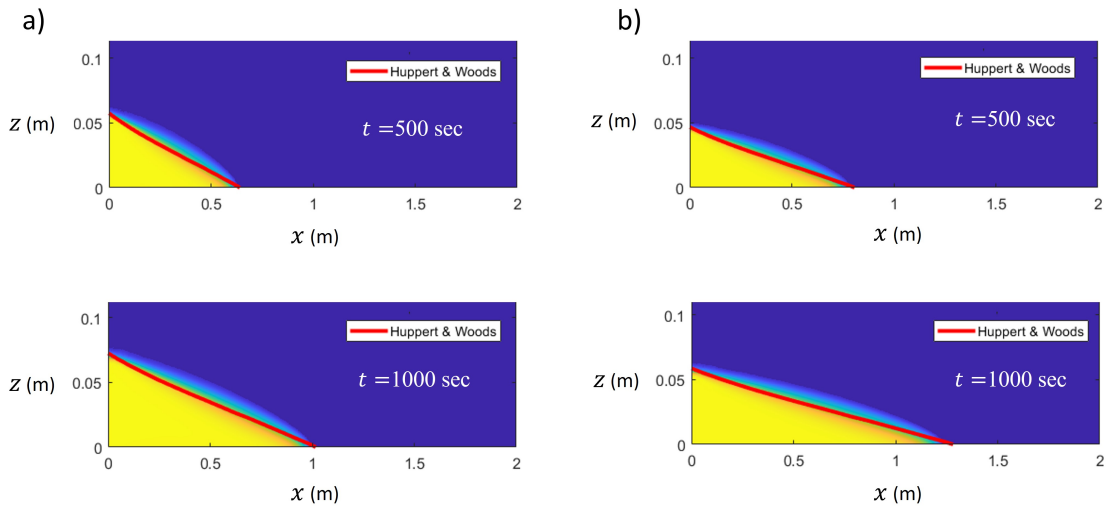

Figure C.2: [Colour] Comparison between COMSOL and the Huppert & Woods (1995) solution for a porous media gravity current propagating along an impermeable boundary without drainage. Here, $k = 2.18 \times 10^{-4}$ cm^2, $q_s = 0.14$ cm^2/s and (a) $g'_s = 15$ cm/s^2,(b) $g'_s = 30$ cm/s^2.

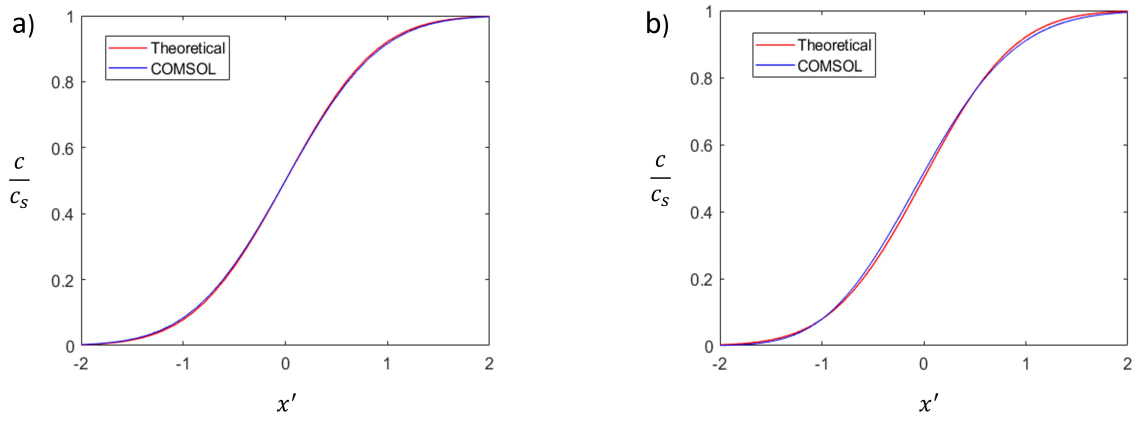

Figure C.3: [Colour] Comparison between COMSOL and Bear's (1972) theoretical solution for a concentration front progressing through a porous medium. Here, $k = 2.18 \times 10^{-4}$ cm^2, $\phi = 0.38$, $t = 200$ sec and (a) $q = 0.001$ cm/s, (b) $q = 0.01$ cm/s. The horizontal axis variable, $x' = \frac{x - \frac{qt}{\phi}}{\sqrt{\frac{4Dt}{\phi}}}$, represents a Galilean-shifted horizontal coordinate in which D is the dispersion coefficient. The vertical axis variable, c/c_s, represents the non-dimensional scalar concentration in which c_s is the concentration ahead of the advancing front.

COMSOL model correctly predicts the degree of dispersion in a scenario where the scalar is passive. To wit, we consider the left-to-right advance of a concentration front in a laterally expansive porous medium and compare the result with the classical solution of Bear (1972). The concentration front advects owing to a steady, uniform flow of Darcy flux q, which is large enough that the Péclet number exceeds unity. Figure C.3 below illustrates that there is a strong agreement between our COMSOL solution and Bear's theoretical solution.

C.1.2 CMG and OpenGoSim

A hallmark of a reliable numerical model is its ability to exhibit a systematic variation in output parameters, e.g. the dispersed buoyancy fraction $\tilde{B}^*_{\text{disp}}$, with respect to changes in the input parameters like petrophysical properties or fluid flow characteristics. For instance, variations in the medium permeability or the injection flow rate should yield a consistent and predictable variation in $\tilde{B}^*_{\text{disp}}$. The variation in question is illustrated in figure C.4. Figure C.4 (a) shows a smooth, monotone increase in the amount of dispersion with the medium permeability. Similar comments apply to figure C.4 (b), which, consistent with figure 14 of Sheikhi *et al.* (2023), illustrates the

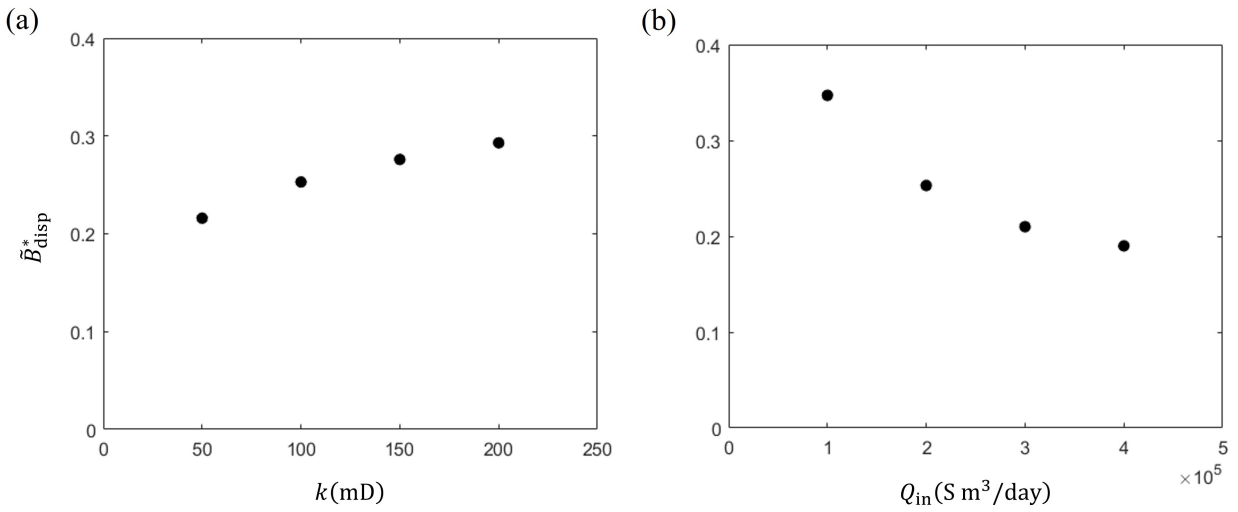

Figure C.4: Dispersed phase buoyancy fraction vs. (a) the medium permeability, k, and (b) the source volume flow rate, Q_{in}. Results are shown assuming a formation pressure of $P_{\text{form}} = 100\,\text{bar}$. We further assume that $\theta = 0°$, $t = 180\,\text{day}$ and $K_{\text{eff}} = 0.015$. Note that $Q_{\text{in}} = 2 \times 10^5\,\text{S m}^3/\text{day}$ in panel (a) and $k = 100\,\text{mD}$ in panel (b).

variation of $\tilde{B}^*_{\text{disp}}$ with the source volume flow rate, Q_{in}.

We also conduct grid independence tests for our reservoir-scale simulations. As an example, figure C.5 illustrates that the CMG solution becomes grid independent beyond approximately 10^6 grid cells.

C.2 Workflow of numerical simulations

The workflow used to obtain numerical simulation, i.e. COMSOL, OpenGoSim and CMG, output in the desired format is demonstrated in figure C.6.

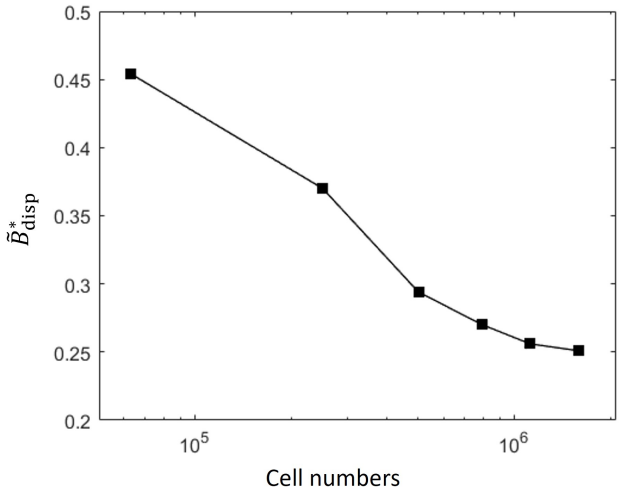

Figure C.5: CMG estimates for the dispersed phase buoyancy fraction for different grid sizes. Here, consistent with figure C.4, $P_{\text{form}} = 100\,\text{bar}$, $Q_{\text{in}} = 2\times10^5\,\text{S m}^3/\text{day}$, $k = 100\,\text{mD}$, $\theta = 0°$, $t = 180\,\text{day}$ and $K_{\text{eff}} = 0.015$.

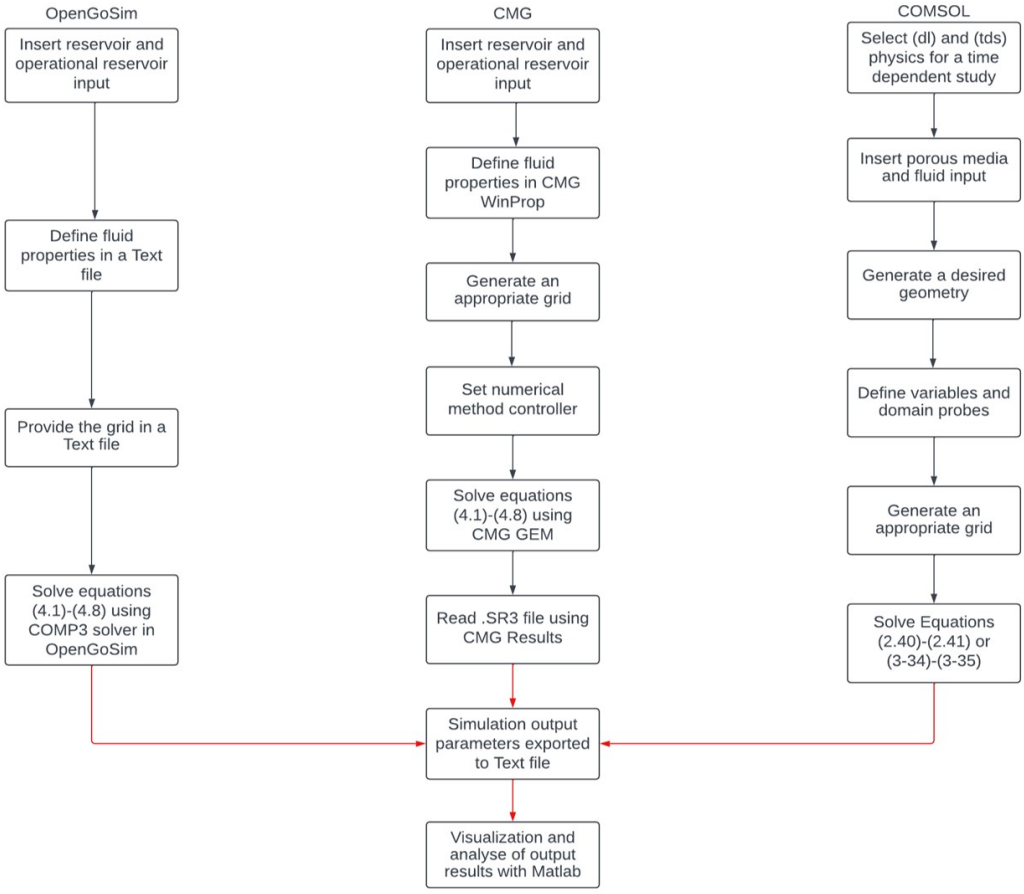

Figure C.6: [Colour] Numerical software workflow visualization.